NEURONAL FILOPODIA BORNE ALONG TIPS AND SHAFTS OF DENDRITES COMPRISE TWO DISTINCT POPULATIONS AS EVIDENCED BY DIFFERENCES IN STRUCTURE AND DYNAMICS

BY

ANIKA JAIN

DISSERTATION

Submitted in partial fulfillment of the requirements
for the degree of Doctor of Philosophy in Cell and Developmental Biology
in the Graduate College of the
University of Illinois at Urbana-Champaign, 2017

Urbana, Illinois

Doctoral Committee:

Professor Martha Gillette, Chair, Director of Research
Professor Rashid Bashir
Associate Professor Stephanie Ceman
Associate Professor William Brieher

Abstract

Ever since their discovery in 1880 by Ramon y Cajal, dendritic spines have evoked considerable interest in the field of cellular and molecular neuroscience. Subsequent studies into their morphogenesis, and into synaptogenesis, brought into the spotlight their putative precursors – the dendritic filopodia. This set off several lines of investigation into filopodial structure and function, notable among which is the work by Portera-Cailliau et al. who showed in 2003 that growth cone filopodia differ from shaft filopodia in terms of densities and lengths, and in their response to blocking of synaptic transmission, and of ionotropic glutamate receptors. However, they observed these differences only up to postnatal day 5. In 2010, Korobova and Svitkina reported the existence of a different actin organization in shaft filopodia at 10 days in vitro (DIV). This work fills the gap between those two studies, investigating differences between tip and shaft filopodia at 4, 7, 10 and 14 DIV, and examining structure and dynamics, as well as responses to developmental cues, specifically, Semaphorin3A (Sema3A).

Using confocal microscopy to visualize filopodial membrane and actin we found that shaft filopodia are shorter than tip filopodia, and show a less dense presentation along the dendrite. We then employed the quantitative phase imaging technology of Spatial Light Interference Microscopy (SLIM) for analysis of mass change dynamics of individual filopodia. We found that tip and shaft filopodia show similar dynamics early on, but further on in development by 7 DIV shaft filopodia slow down considerably while tip filopodia continue to show fast increases and decreases in mass. Further analysis of growth rates showed that both types filopodia exhibit exponential growth during their extension, implying that the bigger the filopodium the faster it grows.

Next we sought to examine the functional ramifications of these differences in tip and shaft filopodia. We investigated the differential responses of the two populations to Sema3A. We found that a 24 h exposure to Sema3A at 0-1 DIV leads to accelerated maturation of shaft filopodia as evidenced by (1) an increase in dendritic branching, (2) an acceleration of maturation into spines, and (3) into synapses. An analysis of the underlying dynamics showed that Sema3A treatment results in (1) tip filopodial movement becoming more deterministic, (2) an increase in average growth and shrinkage rates in shaft filopodia, and, (3) an increase in speed of the fastest growth and shrinkage in tip and shaft filopodia at 4 and 7 DIV. Together these findings show that Sema3A is a unique cue that acts on both tip filopodia and shaft filopodia, but with different outcomes – the former to increase dendrite lengths, and the latter to increase branching, spinogenesis and synaptogenesis. Bath application of Sema3A also elicits an axonal response, which might itself affect the cells as a whole, and could confound the filopodial read out. To avoid this, we supplemented bath application studies with investigations using microfluidic devices that enable focal, dendrite specific application of Sema3A, and, also, better replicate the *in vivo* layered structure of the hippocampus. Our results held true even with this sub-cellular administration of Sema3A.

Taken together our findings provide further evidence for differences in the two dendritic filopodial populations – those borne on the tips, and those along the shafts, and help deconstruct the role of Sema3A in dendritic development. A greater comprehension of this diversity in the filopodial population, and its role in shaping the development of neuronal networks will not only further our understanding of the nervous system, but will also help unravel the mechanistic bases of developmental disorders and diseases.

To my parents

ACKNOWLEDGEMENTS

First and foremost, I want to thank my advisor, Martha Gillette, for her guidance and encouragement. Her mentorship in the conduct and communication of science, and her infectious enthusiasm for it, not only made this work possible, but also fun and rewarding.

The work presented in this thesis owes much to scientific input from a number of people. I am grateful to my collaborators, Gabriel Popescu and Taewoo Kim, for generously sharing their time and expertise in Spatial Light Interference Microscopy. Thanks also to the members of my thesis committee – Rashid Bashir, Stephanie Ceman, William Brieher, and Phillip Newmark – for helping guide my research.

I have greatly enjoyed my time at the Gillette lab, and for that I thank all my lab mates, past and present. I am particularly grateful to Larry Millet and Jennifer Mitchell for showing me the ropes; to Olivia Cangellaris, for her help with designing and manufacturing microfluidic devices; and to Ann Benefiel, Maureen Holtz, and Karen Weis for being my guide through the labyrinths of publication, training, and, equipment purchase and maintenance.

As for babies, so for theses – it takes a village! A very special thank you to the many members of the university staff, whose support kept me sane and functioning; to my course coordinator, Elizabeth Good, for her friendship through the joys of teaching and the trials of grading; to the administrative staff, especially Delynn Carter, Shannon Croft, Laura Martin, Elaine Rodgers, and Laura Miller, for creating order out of the chaos of submissions, deadlines and other graduate school requirements; to the animal care personnel, for their tireless and meticulous dedication to the maintenance of the animal facilities; to the Information Technology staff, particularly Jeffrey Haas, Karl Schlipf, and Bemi Ekwejunor, for being the guardians and saviors of my data; and to Doug and the custodial staff, for their care and friendship. I would be lost were it not for the support and smiles you have all been so generous with.

I also deeply treasure the support of my brother, Rahul Jain. Were it not for our insane trips chasing solar eclipses across the world, this wouldn't have been half the adventure it ended up being. A very special thanks to Aditya Sharma. Aditya, a Ph.D. is a series of important findings, and finding you will always be my proudest accomplishment. Heartfelt thanks also to Onkar Parrikar, my very own Batman, a man so good, so warm, he makes superlatives impotent; to Neha Garg, Divya Balasubramanian, Sneha Narang, and Nandita Kohli, who are the memories of summer on a cold winter's night; to Vineet Abhishek, Nachiketa Chakraborty, and Sachin Kadloor, who are conversations so engrossing you forget to sleep; and to Ankur Jain, Dipti Gorur, Nikhil Chopra, and Sandeep Pawar, who brought me pieces of me I didn't know I was missing. Each of you deserves whole odes of gratitude for indulging me, but you'll have to do with just these few words, and the promise of a lifetime of my love.

I am also thankful for the Krannert Center for Performing Arts and the Art Theater. They have played a more important role in the development of this work than can be expected of any non-lab space.

The journey that brought me here began with a little girl trying to apply the principles of getting yoghurt from milk, to getting oil from water. To my parents, I.P. Jain and Mridula Jain, who kept that crazy curiosity going, thank you for making this possible. What appears to be a few years of my work, is really, decades of yours. Every word of this thesis is a thanks to you for your strength and your love.

TABLE OF CONTENTS

LIST OF ABBREVIATIONS

Arp2/3	Actin-related protein-2/3
ATP	Adenosine triphosphate
BSA	Bovine serum albumin
C1	Channel 1
C2	Channel 2
C3	Channel 3
CA1	Cornus ammonis 1
CAD	Computer-Aided Design
cGMP	Cyclic guanosine monophosphate
CNS	Central Nervous System
CRMP	Collapsin Response Mediator Protein
DI	De-ionized
DiA	4-(4-(Dihexadecylamino)styryl)-N-Methylpyridinium Iodide
DIV	Days in vitro
DMEM	Dulbecco's Modified Eagle Medium
DMSO	Dimethyl sulfoxide
EDTA	Ethylenediaminetetraacetic acid
E-PDMS	Extracted polydimethylsiloxane
F-actin	Filamentous actin
FBS	Fetal bovine serum
FITC	Fluorescein isothiocyanate
GFAP	Glial fibrillary acidic protein

H	Height
HPLC	High Performance Liquid Chromatography
LSM	Laser scanning microscope
MAP	Microtubule Associated protein
NGS	Normal Goat Serum
NLO	Nonlinear optical
N-WASP	Neuronal Wiskott–Aldrich Syndrome protein
P	Postnatal day
PBS	Phosphate Buffered Saline
PDL	Poly-D-lysine
PDMS	Polydimethylsiloxane
PHS	Public Health Service
PLL	Poly-L-lysine
ROI	Region of interest
Sema3A	Semaphorin 3A
SLIM	Spatial Light Interference Microscopy
U	Units of enzymatic activity
USP	United States Pharmacopeia
UV	Ultra-violet light
W	Width
WAVE1	Wiskott-Aldrich syndrome protein family member 1

CHAPTER 1: INTRODUCTION

Filopodia

Filopodia are dynamic, thread-like protrusions of the cell membrane that contain loose bundles of about 10-30 actin filaments. Since they first came to prominence in the 1960's,[1,2] a diverse population of cells has been found to employ filopodia to explore the extracellular environment and surfaces of other cells, identify appropriate targets for contact or adhesion, and generate guidance cues and traction forces for the directed growth and/or migration of the cell. Hence, while on the one hand they aid migration in cells like fibroblasts and keratinocytes, on the other they assist morphogenetic events, including gastrulation,[3] dorsal closure in *Drosophila*,[4] ventral enclosure in *Caenorhabditis elegans*,[5] epithelial cell adhesion[6] and wound healing.[7]

The nervous system is replete with instances where filopodial navigation is put to use to establish and maintain the intricate wiring of neuronal networks. During the initial stages of development, neurons migrate from the lumen of the neural tube to distinct distal layers of their target tissues. They must also send out axons to synapse with appropriate partners. Processes such as experience-dependent refinement and synaptic plasticity continue into adulthood and are thought to be a basis of learning and memory. At the forefront of all these events are filopodia.

Due to the plethora of studies on axon guidance,[8–10] axonal growth cone filopodia remained the primary focus of research for several years. Spurred by technological advances, scientists have now begun to explore the structural and functional landscape of dendritic filopodia. These are 200-300 nm wide, 2-20 μm long protrusions that occur

predominantly during early postnatal development (P2-12 for cortical pyramidal cells).[11,12] They have been implicated in spinogenesis,[13–17] synaptogenesis[13,17–20] and dendritic morphogenesis.[21,22]

Spinogenesis: First described by Ramón y Cajal in 1888, spines form sites of neuron-to-neuron communication, and are thought to be the dynamic substrates of experience-dependent memory formation.[23–25] More than 90% of excitatory axo-dendritic synapses in the central nervous system (CNS) occur at these sites.[26] Neurons receiving inputs from diverse sources, such as pyramidal cells in the cerebral cortex and hippocampus, are particularly rich in spines.[26–30] In these cells, the appearance of filopodia just precedes that of spines.[11,12,31,32] This sequential appearance, along with similarities in shape and cytoskeletal organization, forms tantalizing evidence for the *filopodial model of spinogenesis,* describing filopodia as immature protrusions that develop into spines upon axonal contact.[33] Further support comes from imaging data showing eventual stabilization of filopodia, approaching a more 'spine-like' state.[11,20,34]

Synaptogenesis: Another school of thought attributes a more exploratory role to filopodia, hypothesizing that their primary role is to contact axons and establish early synapses – independent of eventual spine formation.[35] This forms the essence of Vaughn's 'synaptotropic' hypothesis which states that filopodia 'catch' and recruit axons, followed by the formation of synapses.[36–38] The inherent flexibility of filopodia makes them ideal for spatial sampling. Furthermore, since synaptogenesis is arguably the most important task for a developing neuron, it validates the massive energy expenditure required of that cell to extend and retract tens of thousands of filopodia per day. In support of this model, an electron microscopsy analysis of rat hippocampal neurons in the

CA1 region has revealed that numerous dendritic filopodia form synaptic contacts.[39] In addition, about 70% of synaptic contacts in the developing chick spinal cord are found on filopodia.[40]

Dendritic morphogenesis: Another aspect of Vaughn's 'synaptotropic' hypothesis is its explanation of dendritic morphogenesis. According to the hypothesis, the formation of a synapse on the filopodium results in retrograde signals that stimulate growth and/or branching towards regions rich in synaptic activity.[37] Hence, filopodia not only initiate synaptogenesis, but also model the branching pattern of the dendritic tree.[21] This idea is particularly tempting, since it correlates adult dendritic morphology with the history of synaptic activity and of interactions of the filopodia with axons and the surrounding environment. It also minimizes the need of detailed genetic instructions to create the highly complex dendritic arbors.

More recently dendritic filopodia also have been implicated in developmental plasticity and even repair and regeneration.[13,22]

Tip and shaft filopodia

Despite this large body of initial exploratory work, several questions regarding filopodial dynamics remain unanswered. For instance, while axonal and dendritic filopodia are treated as distinct populations, filopodia borne along the shafts of dendrites often get clubbed together with those at the tips of the dendrites. This despite evidence of significant structural differences between these shaft and tip filopodia (Figure 1.1).[15] Korobova and Svitkina showed in 2010 that actin arrangement in shaft filopodia in primary hippocampal neurons at 10 DIV (days in vitro) differs significantly from the

conventional model of filopodial cytoskeletal organization. Instead of parallel bundles of actin characteristic of conventional filopodia (Figure 1.1B), these filopodia have a mix of aligned and branched actin filaments, resulting in a crisscross network-like arrangement. Their examination of myosin decoration of these actin filaments revealed the presence of actin filaments with the barbed end of the filament pointing away from the filopodial tip – the exact inverse of the polarity predicted by the conventional model (Figure 1.1C). Studies treating these shaft filopodia as different from tip filopodia are rare.[41] Hence while the structural and chemical cues guiding filopodial dynamics have been well-studied, their differential effects on shaft and tip filopodia remain obscure.

Role of Semaphorin 3A

Semaphorin 3A (Sema3A) is one such cue that, in particular, needs to be investigated further. It is a critical short-range diffusive cue that guides neuronal pattern development by acting as a negative cue for axons, binding to receptors on axonal growth cone filopodia and mediating axonal growth-cone collapse,[42] and as a positive cue for dendrites, stimulating their growth and branching.[43–45] It also has several other region-specific guidance effects throughout the nervous system. In the neocortex, it directs apical dendrite extension toward the pial surface[43] and aids in migration and regeneration of neocortical neurons.[46] Being a signaling protein that selectively promotes dendrite survival and growth, its effects on the dendritic filopodia are all the more relevant. Even so, its differential regulation of these developmental processes at the level of tip and shaft filopodia remains unknown.

Compartmentalization through microfluidic devices

One of the reasons why these avenues remain relatively unexplored is the inherent difficulty of studying the finer details of filopodial dynamics using the conventional paradigm of neuronal dish culture. These culture systems allow only limited control and manipulation of the neuronal microenvironment. Recent advances in microfluidics have opportunely provided neuroscientists with a revolutionary culture platform – the microfluidic device. Tracing their origin to the Campenot chamber, these devices are a powerful tool with varied biological applications.[47–50] Today, soft lithography can be used to fabricate devices of virtually any design using Computer-Aided Design (CAD)-generated patterns.[47] These enable incorporation of features of dimensions down to as low as 10 nm. The devices are fabricated using polydimethylsiloxane (PDMS) – a polymer that is inexpensive, flexible and optically transparent down to 230 nm. It is impermeable to water, non-toxic to cells and permeable to gases, making it ideal for biological studies.[48,51]

Neuronal cultures in microdevices are a more faithful simulation of the complexity of the mammalian CNS, where distinct sub-regions of the neurons have distinct chemical environments.[50,52] In studies of filopodial development, state-of-the-art microdevices have the potential to enable maximal control of the microenvironments around different sub-regions of a neuronal network and also an individual neuron.[53–57] Compartmentalization of neurons, that is, having different sub-regions of the neuron growing in different, fluidically isolated chambers or channels, allows selective and localized stimulation of specific regions.[52,58,59] Furthermore, manipulations of fluid dynamics provide unparalleled spatiotemporal control for establishing fluidic and

surface-bound gradients.[53,54,60–65] This convergence of filopodial investigations and the technology of microfluidics, when coupled with high resolution imaging and sophisticated software for data analysis, has the potential to aid in deciphering the guidance cues that direct the development of dendritic filopodia in hippocampal neurons.

Statement of problem and significance

Fully functioning filopodia are critical to the establishment of neuronal connectivity through dendritic morphogenesis, spinogenesis and synaptogenesis. Anomalies in these processes are at the root of diverse developmental disorders, such as Down's syndrome,[66,67] Fragile-X mental retardation,[68] schizophrenia, and mood disorders.[69] Sema3A, in particular, has been implicated in schizophrenia[70] and Alzheimer's.[71] Better comprehension of the processes that shape development will help deconstruct the underlying mechanisms of these developmental disorders and diseases, thereby, aiding the advancement of cures and relief.

Hence, with a view towards furthering our understanding of network formation in the brain, the aim of my work is to examine the differential presentation and behavior of filopodia along the tips and shafts of dendrites of primary hippocampal neurons. I examined trends in lengths, densities, mass-change dynamics, and response to Sema3A, over the developmental time course of 4 to 14 days-in-vitro (DIV).

Conducting structural analyses using membrane and actin labels, I found that tips bear longer filopodia, and at higher densities at 4 and 7 DIV. I examined filopodial mass change dynamics using Spatial Light Interference Microscopy (SLIM), an innovative quantitative phase imaging method that enables high-resolution label-free imaging of live

cells and allows measurements of the dry mass of live neurons at femtogram levels.[72] My analysis of time-lapse SLIM imaging of dendritic filopodia showed that (1) tip filopodia show significantly higher rates of change of mass, for both growth and shrinkage, relative to shaft filopodia, and (2) both tip and shaft filopodia exhibit an exponential growth, i.e., the rate of growth increases as filopodial mass increases. I discuss these findings in Chapter 2.

Next I investigated specifically the role of Sema3A in filopodial development, guiding dendritic morphogenesis, spinogenesis, and synaptogenesis. Sema3A acts not only at the level of the dendrites, promoting neurite survival and growth, but also at the level of the filopodia. I found that a 24-h exposure to Sema3A administered 1 h after cell seeding leads to accelerated maturation of shaft filopodia as evidenced by (1) an increase in the branching of the dendrites, (2) an acceleration of maturation of these filopodia into spines and (3) into synapses, and, (4) an increase in growth and shrinkage rates in shaft filopodia selectively. These results hold true even with sub-cellular administration of Sema3A using microfluidic devices. I present these in further details in Chapter 3.

Taken together our findings provide further evidence for differences in the two filopodial populations – those borne on the tips, and those along the shafts, of dendrites, and help deconstruct the role of Sema3A in dendritic development. A greater comprehension of this diversity in the filopodial population, and its role in shaping the development of neuronal networks will not only further our understanding of the nervous system, but will also help unravel the mechanistic bases of developmental disorders and diseases.

Literature cited

1. Kinnander, H. & Gustafson, T. Further studies on the cellular basis of gastrulation in the sea urchin larva,. *Exp. Cell Res.* **19,** 278–290 (1960).

2. Tilney, L. G. & Gibbins, J. R. Microtubules and filaments in the filopodia of the secondary mesenchyme cells of Arbacia punctulata and Echinarachnius parma. *J. Cell Sci.* **5,** 195–210 (1969).

3. Kinnander, H. & Gustafson, T. Further studies on the cellular basis of gastrulation in the sea urchin larva,. *Exp. Cell Res.* **19,** 278–290 (1960).

4. Millard, T. H. & Martin, P. Dynamic analysis of filopodial interactions during the zippering phase of Drosophila dorsal closure. *Development* **135,** 621–626 (2008).

5. Williams-Masson, E. M., Malik, A. N. & Hardin, J. An actin-mediated two-step mechanism is required for ventral enclosure of the C. elegans hypodermis. *Development* **124,** 2889–901 (1997).

6. Phng, L. K. *et al.* Formin-mediated actin polymerization at endothelial junctions is required for vessel lumen formation and stabilization. *Dev. Cell* **32,** 123–132 (2015).

7. Wood, W. *et al.* Wound healing recapitulates morphogenesis in Drosophila embryos. *Nat. Cell Biol.* **4,** 907–912 (2002).

8. Dickson, B. J. Molecular mechanisms of axon guidance. *Science (80-.).* **298,** 1959–1964 (2002).

9. Dent, E. W. & Gertler, F. B. Cytoskeletal dynamics and transport in growth cone motility and guidance. *Neuron* **40,** 209–227 (2003).

10. Tessier-Lavigne, M. Wiring the brain: the logic and molecular mechanisms of axon guidance and regeneration. *Harvey Lect.* **98,** 103–43

11. Portera-Cailliau, C., Pan, D. T. & Yuste, R. Activity-regulated dynamic behavior of early dendritic protrusions: evidence for different types of dendritic filopodia. *J. Neurosci. Off. J. Soc. Neurosci.* **23,** 7129–7142 (2003).

12. Miller, M. & Peters, a. Maturation of rat visual cortex. II. A combined Golgi-electron microscope study of pyramidal neurons. *J. Comp. Neurol.* **203,** 555–573 (1981).

13. Chen, Y., Bourne, J., Pieribone, V. A. & Fitzsimonds, R. M. The role of actin in the regulation of dendritic spine morphology and bidirectional synaptic plasticity. *Neuroreport* **15,** 829–32 (2004).

14. Harris, K. M. Structure, development, and plasticity of dendritic spines. *Curr. Opin. Neurobiol.* **9,** 343–348 (1999).

15. Korobova, F. & Svitkina, T. Molecular architecture of synaptic actin cytoskeleton in hippocampal neurons reveals a mechanism of dendritic spine morphogenesis. *Mol. Biol. Cell* **21,** 165–76 (2010).

16. Tada, T. & Sheng, M. Molecular mechanisms of dendritic spine morphogenesis. *Curr. Opin. Neurobiol.* **16,** 95–101 (2006).

17. Zito, K. *et al.* Induction of Spine Growth and Synapse Formation by Regulation of the Spine Actin Cytoskeleton. *Neuron* **44,** 321–334 (2004).

18. Friedman, H. V, Bresler, T., Garner, C. C. & Ziv, N. E. Assembly of new individual excitatory synapses: time course and temporal order of synaptic molecule recruitment. *Neuron* **27,** 57–69 (2000).

19. Knott, G. W., Holtmaat, A., Wilbrecht, L., Welker, E. & Svoboda, K. Spine growth precedes synapse formation in the adult neocortex in vivo. *Nat. Neurosci.* **9,** 1117–24 (2006).

20. Ziv, N. E. & Smith, S. J. Evidence for a role of dendritic filopodia in synaptogenesis and spine formation. *Neuron* **17,** 91–102 (1996).

21. Gao, F.-B. Molecular and cellular mechanisms of dendritic morphogenesis. *Curr. Opin. Neurobiol.* **17,** 525–32 (2007).

22. Portera Cailliau, C. & Yuste, R. [On the function of dendritic filopodia]. *Rev. Neurol.* **33,** 1158–66

23. y Cajal, S. R. Estructura de los centros nerviosos de las aves. *Rev. Trim. Histol. Norm. Patol.* **1,** 1–10 (1888).

24. Ethell, I. M. & Pasquale, E. B. Molecular mechanisms of dendritic spine development and remodeling. *Prog. Neurobiol.* **75,** 161–205 (2005).

25. Sorra, K. E. & Harris, K. M. Overview on the structure, composition, function, development, and plasticity of hippocampal dendritic spines. *Hippocampus* **10,** 501–11 (2000).

26. Harris, K. M. & Kater, S. B. Dendritic spines: cellular specializations imparting both stability and flexibility to synaptic function. *Annu. Rev. Neurosci.* **17,** 341–71 (1994).

27. Cragg, B. G. The density of synapses and neurones in the motor and visual areas of the cerebral cortex. *J. Anat.* **101,** 639–54 (1967).

28. Peters, A., Palay, S. L. & Webster, H. deF. *The fine structure of the nervous system : neurons and their supporting cells*. (Oxford University Press, 1991).

29. Shepherd, G. M. The dendritic spine: a multifunctional integrative unit. *J. Neurophysiol.* **75,** 2197–210 (1996).

30. Konur, S., Rabinowitz, D., Fenstermaker, V. L. & Yuste, R. Systematic regulation of spine sizes and densities in pyramidal neurons. *J. Neurobiol.* **56,** 95–112 (2003).

31. Morest, D. K. The growth of dendrites in the mammalian brain. *Z. Anat. Entwicklungsgesch.* **128,** 290–317 (1969).

32. Morest, D. K. The differentiation of cerebral dendrites: A study of the post-migratory neuroblast in the medial nucleus of the trapezoid body. *Z. Anat. Entwicklungsgesch.* **128,** 271–289 (1969).

33. Yuste, R. & Bonhoeffer, T. Genesis of dendritic spines: insights from ultrastructural and imaging studies. *Nat. Rev. Neurosci.* **5,** 24–34 (2004).

34. Dailey, M. E. & Smith, S. J. The dynamics of dendritic structure in developing hippocampal slices. *J. Neurosci.* **16,** 2983–94 (1996).

35. Wong, R. O. L., Yamawaki, R. M. & Shatz, C. J. Synaptic Contacts and the Transient Dendritic Spines of Developing Retinal Ganglion Cells. *Eur. J. Neurosci.* **4,** 1387–1397 (1992).

36. Berry, M. & Bradley, P. The growth of the dendritic trees of Purkinje cells in the cerebellum of the rat. *Brain Res.* **112,** 1–35 (1976).

37. Vaughn, J. E. Review: Fine structure of synaptogenesis in the vertebrate central nervous system. *Synapse* **3,** 255–285 (1989).

38. Vaughn, J. E., Henrikson, C. K. & Grieshaber, J. A. A quantitative study of synapses on motor neuron dendritic growth cones in developing mouse spinal cord. *J. Cell Biol.* **60,** 664–72 (1974).

39. Fiala, J. C., Feinberg, M., Popov, V. & Harris, K. M. Synaptogenesis via dendritic filopodia in developing hippocampal area CA1. *J. Neurosci.* **18,** 8900–11 (1998).

40. Skoff, R. P. & Hamburger, V. Fine structure of dendritic and axonal growth cones in embryonic chick spinal cord. *J. Comp. Neurol.* **153,** 107–47 (1974).

41. Portera-Cailliau, C., Pan, D. T. & Yuste, R. Activity-regulated dynamic behavior of early dendritic protrusions: evidence for different types of dendritic filopodia. *J. Neurosci.* **23,** 7129–42 (2003).

42. Fournier, A. E. *et al.* Semaphorin3A enhances endocytosis at sites of receptor-F-actin colocalization during growth cone collapse. *J. Cell Biol.* **149,** 411–421 (2000).

43. Polleux, F., Morrow, T. & Ghosh, A. Semaphorin 3A is a chemoattractant for cortical apical dendrites. *Nature* **404,** 567–73 (2000).

44. Fenstermaker, V., Chen, Y., Ghosh, A. & Yuste, R. Regulation of dendritic length and branching by semaphorin 3A. *J. Neurobiol.* **58,** 403–12 (2004).

45. Morita, A. *et al.* Regulation of dendritic branching and spine maturation by semaphorin3A-Fyn signaling. *J. Neurosci.* **26,** 2971–80 (2006).

46. Chen, G. *et al.* Semaphorin-3A guides radial migration of cortical neurons during development. *Nat. Neurosci.* **11,** 36–44 (2008).

47. McDonald, J. C. *et al.* Fabrication of microfluidic systems in poly(dimethylsiloxane). *Electrophoresis* **21,** 27–40 (2000).

48. Sia, S. K. & Whitesides, G. M. Microfluidic devices fabricated in poly(dimethylsiloxane) for biological studies. *Electrophoresis* **24,** 3563–76 (2003).

49. Taylor, A. M. *et al.* Microfluidic Multicompartment Device for Neuroscience Research. *Langmuir* **19,** 1551–1556 (2003).

50. Walker, G. M., Zeringue, H. C. & Beebe, D. J. Microenvironment design considerations for cellular scale studies. *Lab Chip* **4,** 91–7 (2004).

51. Mata, A., Fleischman, A. J. & Roy, S. Characterization of polydimethylsiloxane (PDMS) properties for biomedical micro/nanosystems. *Biomed. Microdevices* **7,** 281–93 (2005).

52. Wang, J. *et al.* Microfluidics: a new cosset for neurobiology. *Lab Chip* **9,** 644–52 (2009).

53. Joanne Wang, C. *et al.* A microfluidics-based turning assay reveals complex growth cone responses to integrated gradients of substrate-bound ECM molecules and diffusible guidance cues. *Lab Chip* **8,** 227–37 (2008).

54. Keenan, T. M. & Folch, A. Biomolecular gradients in cell culture systems. *Lab Chip* **8,** 34–57 (2008).

55. Park, T. H. & Shuler, M. L. Integration of cell culture and microfabrication technology. *Biotechnology Progress* **19,** 243–253 (2003).

56. Rhee, S. W. *et al.* Patterned cell culture inside microfluidic devices. *Lab Chip* **5,** 102–7 (2005).

57. Thiébaud, P., Lauer, L., Knoll, W. & Offenhäusser, A. PDMS device for patterned application of microfluids to neuronal cells arranged by microcontact printing. *Biosens. Bioelectron.* **17,** 87–93 (2002).

58. Taylor, A. M. *et al.* A microfluidic culture platform for CNS axonal injury, regeneration and transport. *Nat. Methods* **2,** 599–605 (2005).

59. Jain, A. & Gillette, M. U. Development of microfluidic devices for the manipulation of neuronal synapses. *Neuromethods* **103,** 127–137 (2015).

60. Chung, B. G. *et al.* Human neural stem cell growth and differentiation in a gradient-generating microfluidic device. *Lab Chip* **5,** 401–6 (2005).

61. Corey, J. M. & Feldman, E. L. Substrate patterning: An emerging technology for the study of neuronal behavior. *Exp. Neurol.* **184,** (2003).

62. Fosser, K. A. & Nuzzo, R. G. Fabrication of patterned multicomponent protein gradients and gradient arrays using microfluidic depletion. *Anal. Chem.* **75,** 5775–82 (2003).

63. Romanova, E. V, Fosser, K. A., Rubakhin, S. S., Nuzzo, R. G. & Sweedler, J. V. Engineering the morphology and electrophysiological parameters of cultured neurons by microfluidic surface patterning. *FASEB J.* **18,** 1267–9 (2004).

64. Shi, P., Shen, K. & Kam, L. C. Local presentation of L1 and N-cadherin in multicomponent, microscale patterns differentially direct neuron function in vitro. *Dev. Neurobiol.* **67,** 1765–76 (2007).

65. Millet, L. J., Stewart, M. E., Nuzzo, R. G. & Gillette, M. U. Guiding neuron development with planar surface gradients of substrate cues deposited using microfluidic devices. *Lab Chip* **10,** 1525–35 (2010).

66. Becker, L. E., Armstrong, D. L. & Chan, F. Dendritic atrophy in children with Down's syndrome. *Ann. Neurol.* **20,** 520–526 (1986).

67. Takashima, S., Iida, K., Mito, T. & Arima, M. Dendritic and histochemical development and ageing in patients with Down's syndrome. *J. Intellect. Disabil. Res.* **38 (Pt 3),** 265–73 (1994).

68. Irwin, S. A., Galvez, R. & Greenough, W. T. Dendritic spine structural anomalies in fragile-X mental retardation syndrome. *Cereb. Cortex* **10,** 1038–44 (2000).

69. Law, A. J., Shannon Weickert, C., Hyde, T. M., Kleinman, J. E. & Harrison, P. J. Reduced Spinophilin But Not Microtubule-Associated Protein 2 Expression in the Hippocampal Formation in Schizophrenia and Mood Disorders: Molecular Evidence for a Pathology of Dendritic Spines. *Am J PsychiatryAm J Psychiatry* **161,** 1848–1855 (2004).

70. Eastwood, S. L., Law, A. J., Everall, I. P. & Harrison, P. J. The axonal chemorepellant semaphorin 3A is increased in the cerebellum in schizophrenia and may contribute to its synaptic pathology. *Mol. Psychiatry* **8,** 148–55 (2003).

71. Good, P. F. *et al.* A role for semaphorin 3A signaling in the degeneration of hippocampal neurons during Alzheimer's disease. *J. Neurochem.* **91,** 716–36 (2004).

72. Wang, Z. *et al.* Spatial light interference microscopy (SLIM). *Opt. Express* **19,** 1016 (2011).

73. Biyasheva, A., Svitkina, T., Kunda, P., Baum, B. & Borisy, G. Cascade pathway of filopodia formation downstream of SCAR. *J. Cell Sci.* **117,** (2004).

Figures

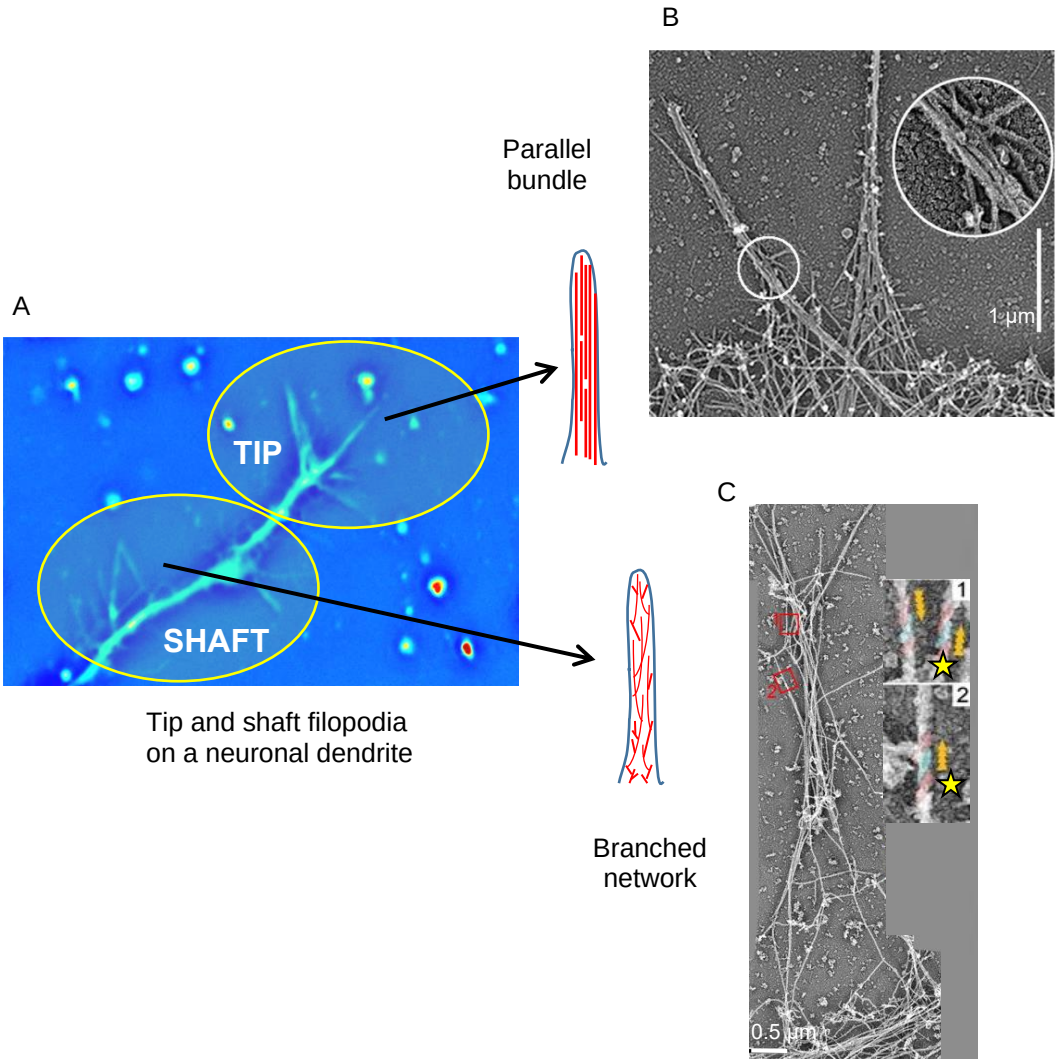

Figure 1.1. Actin cytoskeletal arrangement differs in tip and shaft filopodia. (A) Phase contrast image of a dendrite of a primary rat hippocampal neuron showing the sub-dendritic regions of 'Tip' and 'Shaft'. Neuronal filopodia along tips and shafts were thought to exhibit the conventional parallel bundle arrangement of the actin cytoskeleton, shown here in tip filopodia in *Drosophila* BG-2 neuronal cell line (B), adapted from Biyasheva et al 2004.[73] Scale bar = 1 µm. However, shaft filopodia have been shown to have a mix of aligned and branched actin filaments forming a network-like arrangement, as shown in (C), adapted from Korobova and Svitkina 2010.[15] Insets show actin filaments of opposing polarities, including barbed ends pointing away from the filopodial tip (yellow stars), a contradiction of the conventional model of filopodial actin organization. Scale bar = 0.5 µm.

CHAPTER 2: DENDRITIC FILOPODIA BORNE ALONG TIPS AND SHAFTS EXHIBIT DISTINCT BEHAVIORS

Abstract

Ever since their discovery in 1880 by Ramon y Cajal, dendritic spines have evoked considerable interest in the field of cellular and molecular neuroscience. Subsequent studies into their morphogenesis, and into synaptogenesis, brought into the spotlight their putative precursors – the dendritic filopodia. In 2010, Korbova and Svitkina showed that filopodia borne on the shafts of dendrites have a crisscross network-like organization of actin filaments – unlike the usual filopodial cytoskeletal organization of tightly packed, parallel actin bundles. What still remains unknown is (1) how this distinct cytoskeletal organization informs filopodial behavior, and, (2) whether this resulting behavior places shaft filopodia into a population distinct from that of the filopodia at the tips of dendrites. This works seeks to address those questions using confocal microscopy for structural analyses and Spatial Light Interference Microscopy (SLIM) for analysis of mass change dynamics. Focusing on the developmental stages of 4, 7, and 10 days *in vitro* (DIV), we found that shaft filopodia are shorter than tip filopodia, and show a less dense

This study was possible due to a collaboration with Prof. Gabriel Popescu, Department of Electrical and Computer Engineering and Beckman Institute, University of Illinois at Urbana-Champaign, Prof. Popescu provided open access to his innovative imaging equipment and insights determining mass-transport using Scattered Light Interference Microscopy (SLIM). Taewoo Kim, graduate student at the Popescu Lab, helped with image acquisition and dry-mass analysis for one of the repeats of the filopodial dynamics experiments. Support was provided by the National Science Foundation IGERT 0965918 (AJ) and STC CBET 0939511 (MUG, GP), and the National Institutes of Health NIH R21MH085220 and R21MH101655 (MUG).

presentation along the dendrite. SLIM enabled me to measure the masses of individual filopodia, and time-lapse SLIM imaging revealed differences in filopodial dynamics. Tip and shaft filopodia show similar dynamics early on, but further on in development by 7 DIV shaft filopodia slow down considerably while tip filopodia continue to show fast increases and decreases in mass. Further analysis of growth rates showed that both types filopodia exhibit exponential growth during their extension. Together these studies establish shaft filopodia as population distinct from tip filopodia – a finding that would aid greater comprehension of the processes of spinogenesis, synaptogenesis, and dendritic morphogenesis.

Introduction

Long mistaken as artifacts of the Golgi staining method, spines finally gained well-deserved recognition through Cajal's work in the 1880's.[1] The discovery set off several lines of investigation into spine structure and function, but progress was slow until recent decades due to the lack of the technological capabilities required to study such fine structures. In the late 1900's to early 2000's, studies of spine structure showed that spine heads are predominantly composed of a meshwork of branched actin filaments, with the narrower spine necks formed of actin bundles;[2–4] investigations into the protein complement reported the presence of the Arp2/3 complex,[5,6] cortactin,[7] WAVE1,[8] and N-WASP,[6] – proteins known to be involved in the establishment and maintenance of branched actin networks; and inquiries into mechanisms of spinogenesis established dendritic filopodia as the precursors of spines.[9–11] In 2010, Korbova and Svitkina took these studies a step further, using platinum-replica electron microscopy to characterize the cytoskeletal organization dendritic spines and filopodia. They found dendritic filpodia

to be different in structure from the conventional filopodia in that they consist of a mix of aligned and branched actin filaments that form a network-like structure.[12] This was the first evidence of the existence of a distinct filopodial population with a cytoskeletal organization different from the typical tight bundle of parallel actin filaments long assumed to be the universal underlying cytoskeletal feature of all filopodia. While their work was focused on relatively mature filopodia in neurons at 10 DIV, Portera-Cailau et al. had earlier studied pyramidal neurons in mouse cortical slices and found differences in dendritic growth cone filopodia and shaft filopodia, but only in early stages of development - from postnatal day (P) 2 to 5.[13] They found growth cone filopodia to be denser, longer, and more motile, but reported these as exclusive characteristics of the growth cone structure that was only detectable till the P5 stage. Thus, there still remains a gap in our understanding of how the cytoskeletal differences unearthed by Korbova and Svitkina instruct filopodial behavior, especially in the mid-to-late stages of filopodial maturation.

Answering that question requires an examination of the dynamics of these dendritic filopodia. Dynamics of cellular and sub-cellular structures, have long been quantified primarily in terms of lengths and volumes, employing phase contrast or fluorescence microscopy to aid visualization. The same has been true of neuronal filopodia as well, with filopodial lengths being the chief parameter being measured.[13,14] While these measurements are very informative, obtaining a more complete picture of dynamics would entail an analysis of variations in mass. Fortunately, there have been a number of innovations in recent years that help circumvent the inherent difficulties of weighing microscopic structures. Prominent among these are the suspended microchannel

resonator,[15,16] and cantilever- or pedestal-based sensors.[17,18] The former are more suited to cell suspensions and are therefore not applicable to neuronal studies that require adherent cell cultures, and the latter lack the high sensitivity and resolution required for the analysis of such fine structures as filopodia. Another technique, based not on resonance but on interferometry, called Spatial Light Interference Microscopy (SLIM), satisfies these requirements and is uniquely suited to the analysis of filopodia (Figure 2.4).[19,20] It is based on the concept that the optical phase shift induced in light as it passes through a cell is linearly proportional to the dry mass in that region.[21] This idea of quantitative phase imaging is realized through a combination of phase contrast microscopy and holography.[22,23] The former provides high-contrast intensity images, while holography provides quantitative path-length maps for mass calculation, making possible femtogram-level analyses of mass dynamics in filopodia in ideal, label-free, culture conditions.

To further understand the implications of a change in the mass of a filopodium, it is worthwhile to consider the possible origins of the changes in mass. Mass depends on volume and density, as,

$$M = V.\rho$$

where, M = mass, V = volume, ρ = density

To further examine the expression, the structure of a filopodium can be approximated to resemble a cylinder that has been cut in half longitudinally, along its length. For such a case, the expression for mass expands as follows –

$$M = (\pi r^2 h/2).\rho$$

where, r = half the width of the filopodium, and, h = length of the filopodium.

For filopodia, of the three factors on which mass depends – width, length, and density – length is the one that changes predominantly. As such, it is to be expected that mass changes mostly reflect changes in filopodial length. Instances of deviation from a length correlation would most often be due to changes in filopodial width which is captured by mass, but not length, variation analyses. Given that a wider filopodium has a greater surface area (surface area ~ πrh), and therefore greater potential for interaction and exploration, a parameter that takes the width into account as well is a more accurate representation of the filopodium's capacity to perform its exploratory function.

In addition to elucidating mass changes in a filopodium, dry-mass analysis enables a deeper investigation into the nature of that growth, *i.e.*, whether filopodial growth is linear or exponential. Linear growth would imply that growth rate is constant over time, and that it is independent of the size of the filopodium. Exponential growth rate entails a growth rate that increases with size, that is, the larger the filopodium, the faster it would grow (Figure 2.10). Using the aforementioned mass-measurement techniques, several groups have conducted such growth pattern investigations for several cell types. For instance, *Bacillus subtilis, Escherichia coli, Saccharomyces cerevisiae* and mouse lymphoblasts were shown to all exhibit exponential growths.[15] On the other hand, rat Schwann cells were reported to grow at the same rate independent of cell size.[24] In 2011, Mir *et al*. demonstrated the suitability of SLIM for such growth rate studies, confirming exponential growth rate in *E. coli.*[19] Investigations so far have only examined growth rates of populations or single cells, with growth patterns of sub-cellular structures remaining largely unknown. In cells like neurons, where subcellular structures – axons,

dendrites, cell soma – behave and function so differently from each other, such subcellular inquiries merit special attention. The high-resolution mass-change analysis power of SLIM can be recruited towards addressing these questions for filopodial growth patterns.

With these factors taken into account, we exploited the unique capabilities of the SLIM imaging system in addition to traditional confocal microscopy, to build on the foundations of the filopodial investigations presented above. We teased apart the differences between tip and shaft filopodia in primary rat hippocampal neurons across a range of developmental stages, from 4 DIV to 10 DIV, asking if, and how, the underlying cytoskeletal differences affect filopodial development. Through analyses of structure we found that filopodia borne along the tips are longer, and presented at higher densities, than shaft filopodia all through development, though their widths are not significantly different. In analyzing their dynamics, we found that while tip and shaft filopodia show similar dynamics early on, with the progression of neuronal maturation, shaft filopodia soon slow down while tip filopodia continue to show faster increases and decreases in mass, for average as well as highest rates. This mass variation corresponds primarily to variations in length, to filopodial growth and shrinkage. We examined growth rate trends in filopodia and found filopodial growth to be exponential for the majority of the duration of growth.

Here, we present evidence for the existence of two distinct populations of dendritic filopodia, those borne on the tips and those along the shafts, based on structure as well as dynamics.

Materials and methods

Cell culture

Source Animal - Long-Evans BluGill rats were used in accordance with protocols established by the University of Illinois Institutional Animal Care and Use Committee and in accordance with all state and federal regulations. Hippocampi were harvested from P1-P2 rat pups following previously published protocols.[25,26] Hibernate-A (Brain Bits, Springfield, IL) and Neurobasal-A (Invitrogen) media without phenol red, supplemented with 0.5 mM L-glutamine (Invitrogen), B-27 (Invitrogen), 100 U/ml penicillin, and 0.1 mg/ml streptomycin (Sigma) were used for harvesting and culture, respectively. Hippocampi were dissected out in ice-cold Hibernate, pooled together and treated with papain (25 U/ml, Worthington) in Hibernate at 37 ^{o}C for 15 min, twice, with gentle shaking every 5 min. The papain-media was aspirated, and the tissue was rinsed with 1 ml fresh Hibernate at 37 ^{o}C. Cells were then mechanically dissociated through trituration with a fire-polished Pasteur pipette in 2 ml Hibernate. The supernatant from two such dissociations was pooled and centrifuged at 1400 rpm for 5 min. The cell pellet was resuspended in 1 ml Neurobasal and the cells were counted using a Haemocytometer, and plated at a density of 125-150 cells/mm^2 on acid-washed, PDL-coated (100 mg/ml poly-D-lysine, Sigma) glass-bottom petri dishes.

Cell labeling and immunochemistry

DiA was used to stain cell membranes, by incubating the cells in a staining solution containing 2 µl DiA and 2 µl dimethyl sulfoxide (DMSO) in 2 ml Neurobasal for 10 min, followed by a 5 min PBS rinse. For antibody labeling, cells were fixed with

paraformaldehyde (4%) with 4% sucrose for 15 min, permeabilized using TritonX-100 (0.25% in PBS) for 10 min, and blocked with 5% Normal Goat Serum (NGS) for 30 min. Cells were incubated with primary and secondary antibodies in 2% NGS for 1 hr each. Primary antibody used was anti-MAP-2 (1:1000, Molecular Probes), and secondary antibodies were Alexa Fluor 488 and/or Alexa Fluor 568 secondary antibodies (1:1000, Molecular Probes). Alternatively, for filopodial visualization using phalloidin, fixed and permeabilized cells were incubated with 5 U/ml rhodamine-conjugated phalloidin (Thermo Fisher Scientific) for 20 min. Each step was followed by 5 quick rinses and one 5-min rinse with PBS.

Microscopy and data analysis

For structural studies using DiA, neurons at 4, 7, and 10 DIV were imaged on a laser-equipped Zeiss LSM-510 Meta NLO confocal microscope. Z-stacks were acquired with a slice thickness of 0.5-1 μm, at 100x magnification for filopodial studies (Figure 2.1A). Imaris (Bitplane) was used for reconstruction and 3D-visualiztion of the stacks, and also for the subsequent quantification of cellular and filopodial parameters. The tip and shaft regions of dendrites, confirmed through a second staining with dendrite marker Microtubule Associated Protein 2, MAP2, were then analyzed individually through 3D-reconstructions of the Z-stacks using Imaris software from Bitplane (Figure 2.1B and 2.1D). The distal 10 μm of dendrites, inwards from dendritic end points, were designated as ‘tip’ (Figure 2.1C and 2.1E). The next 5 μm inwards from the tip region were excluded from analysis since this is likely to be a zone of transition from tip-like characteristics to shaft-like characteristics. The remaining length of the dendrite, leaving out the 10 μm tip

region and the 5 μm transition zone, was designated as the 'shaft' (Figure 2.1C and 2.1E). All results obtained with DiA labeling and Imaris analysis were validated with rhodamine-phalloidin labelling. Rhodamine-phalloidin stained cells were imaged on a Zeiss LSM 880 NLO confocal microscope at 63x, and analyzed using ImageJ.

For dynamic analyses, live cells were imaged on an Axiovert fluorescence microscope equipped with a Spatial Light Interference Microscopy (SLIM) module to collect phase data. Images were acquired at 63x magnification every 1.5-3.0 s for a total of 5 min for each field of view. Background elimination, thresholding, and Region of Interest (ROI) selections were performed using ImageJ. Raw phase data was processed using MATLAB, or Dry Mass plugin (Phi Optics) on ImageJ and analyzed using Microsoft Excel.

To analyze dynamics for groups of filopodia at the tips and shafts of dendrites, primary rat hippocampal cultures at 4 DIV were imaged at 3-sec intervals for 5 min each for the. After image acquisition, cells were post-stained with MAP2 for identification of neurons *vs.* glia and, dendrites *vs.* axons to enable selective analysis of filopodia borne on neuronal dendrites. ROI's of constant area and shape were drawn to encompass groups of filopodia at the tips and along the shafts of dendrites (Figure 2.5A).

Variable polygon ROI selections in ImageJ were employed to analyze the behavior of individual filopodia (Figure 2.6). ROI's were drawn around each filopodium analyzed, such that they circumscribed the entire field swept by the filopodium in the duration of the time-lapse image series, while also minimizing the area enclosed in order to reduce noise. Each ROI was then individually processed to convert grey scale images

to phase, and phase to dry mass, followed by background subtraction. When applied to entire time series this yields dry mass changes over time for single filopodia.

Results

STRUCTURAL ANALYSES

Dendrite tips and shafts show different filopodial expression

In order to determine filopodial densities within sub-regions of dendrites, tips *vs.* shafts were analyzed by counting the number of filopodial end-points / unit dendrite length. Filopodia at the distal 10 μm of dendrite shafts were designated as tip filopodia, with the next 5 μm inwards being excluded from analysis as a transition zone, and filopodia borne along the remaining length of the dendrite designated as shaft filopodia (Figure 2.1).

At 4 DIV, the tips of the dendrites show an average of 5.06 filopodia / 10 μm, significantly higher than filopodial densities along the shafts, 2.6 filopodia / 10 μm (Unpaired *t* test, n = 3 dishes per time point, 10 cells per dish, $p < 0.01$, Figure 2.2A). This trend extended further through development, with filopodial densities being higher at the tips at 7 DIV (Unpaired *t* test, n = 3 dishes per time point, 10 cells per dish, $p < 0.01$, Figure 2.2B). Widths and lengths were also analyzed for filopodia along tips and shafts. While the widths did not show significant variation, tip filopodia were seen to be longer than shaft filopodia at both the 4 DIV and 7 DIV developmental time points (Unpaired *t* test, n = 3 dishes per time point, 10 cells per dish, $p < 0.01$, Figure 2.2C and 2.2D). At 4 DIV tip filopodia showed average lengths of 4.40 μm, while shaft filopodia were on average 1.37 μm long (Unpaired *t* test, n = 3 dishes per time point, 10 cells per

dish, $p < 0.01$). At 7 DIV there was no significant change in either. Care was taken not to include short and stubby protrusions in the analysis (those less than 0.5 μm in length, and more than 0.5 μm in width) since these are likely to be spines and not filopodia, especially towards the later stages of development.

By 10 DIV, there was marked neuronal network formation and clustering in the culture. At this stage neuronal heterogeneity becomes very evident. A part of the cellular population continues to bear filopodia along the tips as well as the shafts (Figure 2.3 A-D), but the rest, while bearing filopodia along the tips, display none to only a few along the shafts (Figure 2.3 E-H). Even among the cells bearing filopodia, distal segments of dendrites were observed to bear few to no filopodia (Figure 2.3 D). For these cells, dendrites, or dendritic segments, bearing filopodia were selectively analyzed for densities (Figure 2.3I) and lengths (Figure 2.3J). Tip filopodia showed similar numbers as at 4 and 7 DIV, but shaft filopodia, for this subset, were found to be significantly denser and longer than at 4 and 7 DIV (Unpaired *t* test, n = 3 dishes per time point, 10 cells per dish, $p < 0.01$). For these subsets tip filopodia were still more dense than shafts, though they were no longer longer (Unpaired *t* test, n = 3 dishes per time point, 10 cells per dish, $p < 0.01$ for densities). Combining the data for the two populations exerts an averaging effect, yielding values similar to the ones observed at 4 and 7 DIV for shaft filopodia, as well.

FUNCTIONAL ANALYSES

Dendrites of live neurons were analyzed for their filopodial dynamics. Due to the requirements for high-resolution and fast acquisition rate, high-levels of accompanying photo-toxicity rule out most fluorescence-based techniques for such analyses. On the

other hand, label-free Spatial Light Interference Microscopy (SLIM),[20] an innovative quantitative phase imaging based technique, proved ideal for imaging neurons with high sensitivity (Figure 2.4). Furthermore, the high spatial and temporal resolution capabilities of SLIM are well-suited to capturing the fast and high-resolution filopodial dynamics.

Group analysis shows filopodial stabilization at dendrite tips

When groups of filopodia were analyzed at acquisition rates that approach real-time imaging (1.5-3.0 sec intervals), field-wide dry mass analysis showed a drop in dry mass at the tips but not at the shafts (Figure 2.5B and 2.5C). The former is indicative of dendritic growth which is accompanied by stabilization of a few filopodia and retraction of the rest. On the other hand, at the shafts, retraction of some filopodia is accompanied by the extension of others, resulting in an overall balancing effect such that the group dry mass value shows no significant increase or decrease.

SLIM enables femtogram-level analysis of individual filopodia

Group analysis, while being informative, is only indicative of population effects. To learn further about the behavior of individual filopodia, we extended the analysis by using variable polygon ROI selections in Image J and applied data to time series in order to yield dry mass changes over time for single filopodia. Changes in filopodial mass can be due to variations in length, width, and/or density. Mass variation obtained through SLIM was compared with length variation obtained through manual analysis in ImageJ. Figure 2.7 shows an example of such a comparison. A high degree of correlation was found between the two curves, with the correlation coefficient being higher than 0.9.

While length changes were found to be the most significant contributors to mass change data, analysis showed occasional fluctuations in width, in particular during periods of extension and retraction of filopodia, where width changes contributed as well. Density analysis, performed using dry mass analysis of regions within filopodia showed only negligible variation in density over the time course of imaging. Hence, variations in mass obtained through dry mass analysis using SLIM were found to be predominantly due to variations in filopodial length.

Tip and shaft filopodia differ in mass change dynamics and development

To compute rates of change of mass as indicators of filopodial activity, neurons at 4, 7, and 10 DIV were imaged using SLIM and regions of interest containing individual filopodia were selectively analyzed for changes in dry mass, as described above. Figure 2.8 shows representative mass *vs.* time traces for a tip filopodium, and a shaft filopodium at 7 DIV. The findings were quantified with the aim of answering the following questions about the dynamics of tip and shaft filopodia – during the time course of imaging,

(1) How fast can a filopodium increase or decrease in mass, *i.e.*, grow or shrink?
(2) What is the average rate of increase or decrease in mass?
(3) Considering both gain and loss of mass, what is the fastest activity a filopodium is capable of?
(4) Regarding the overall speed of dynamics, what is the average rate of filopodial mass change?

At the early stage of 4 DIV, tip filopodia showed higher values for fastest rate of growth, averaging at 4 fg/s, significantly faster than shaft filopodia at 3.1 fg/s (Unpaired *t*

test, n = 3 dishes, with 7 fields of view/dish, >4 filopodia/field, $p < 0.05$, Figure 2.9A), though average growth rates were similar for both, 0.82 fg/s for tips and 0.9 fg/s for shafts (Figure 2.9A). Shrinkage rates for the two were similar in both the fastest and the average categories.

By the more advanced stage of 7 DIV, a marked slowing down of dynamics was seen in the shaft filopodia, but not in tip filopodia (Figure 2.9B). The fastest rate of growth of shaft filopodia dropped from 3.1 fg/s at 4 DIV to 1.2 fg/s at 7 DIV, and their fastest rate of shrinkage went from 3.2 fg/s to 1.2 fg/s (Unpaired *t* test, n = 3 dishes, with 7 fields of view/dish, >4 filopodia/field, $p < 0.01$). Average rates of growth and shrinkage fell from 0.82 fg/2 and 0.86 fg/s, to 0.32 fg/s and 0.35 fg/s respectively (Unpaired *t* test, n = 3 dishes, with 7 fields of view/dish, >4 filopodia/field, $p < 0.05$). For tip filopodia, no significant change was seen in most of the parameters examined, except for their fastest growth rate which saw a dip from 4 fg/s to 3.3 fg/s (Unpaired *t* test, n = 3 dishes, with 7 fields of view/dish, >4 filopodia/field, $p < 0.05$). Consequently, at this stage, tip filopodia were found to be much more motile and active than shaft filopodia, showing two- to three-fold higher values of maximum and average growth and shrinkage rates (Unpaired *t* test, n = 3 dishes, with 7 fields of view/dish, >4 filopodia/field, $p < 0.05$, Figure 2.9B). An investigation into filopodial dynamics at 10 DIV showed no significant changes from those observed at 7 DIV.

Tip and shaft filopodia show exponential growth

Dry mass data from SLIM imaging of dendritic filopodia at 7 DIV was further analyzed to determine the mass dependence of growth rate – whether filopodial growth is

linear implying that rate of growth is constant and independent of the size of the filopodium (Figure 2.10A and 2.10B), or exponential wherein growth rate would increase with filopodial mass (Figure 2.10C and 2.10D). Growth phase data for 10 tip and 10 shaft filopodia were extracted from the mass variation data (Figure 2.10E), and growth rates were plotted against mass (Figure 2.10F and 2.10G). All filopodia analyzed showed three stages of growth rate variation: (1) a clear exponential phase of growth, where growth rate increased with increasing mass, (2) a brief phase (5.6 s on average) of slowing down of growth, where the filpodium still grew, but the growth rate decreased, and (3) filopodial retraction, with growth rates dipping into the negatives demonstrative of loss of mass. The growth rate constants for the exponential phase ranged from 0.1 s^{-1} to 0.22^{-1}, averaging at 0.17s^{-1}.

Discussion

Over the past few decades, an extensive interest in axon guidance as the key to neuronal patterning and network formation has led to a steady stream of studies,[27–29] with several focusing on axon growth cone filopodia. Dendritic filopodia gained recognition relatively recently, originally as the putative precursors of spines and synapses,[30–34] and prominent players in dendrite growth and branching.[32,35,36] More recently dendritic filopodia have also been implicated in developmental plasticity and even roles of repair and regeneration.[37,38]

Our work digs deeper into some of the questions raised by those original investigations into dendritic filopodia. We examine differences in structural and behavioral expression of filopodia on tips and shafts of dendrites in primary rat

hippocampal neurons at the developmental stages of 4, 7 and 10 DIV. Portera-Cailliau *et al.* had earlier studied pyramidal neurons in mouse cortical slices and found differences in dendritic growth cone filopodia and shaft filopodia, but only in early stages of development - from postnatal day (P) 2 to 5.[13] At P5, they reported growth cones disappeared, as did the differences in the two filopodial populations. In the low density dish cultures we use, cells cultured at 150 cells/mm^2 continued to present a differential filopodial expression – greater densities and lengths at the tips compared to the shafts – even up to the advanced stage of 10 DIV (Figure 2.2 and 2.3). This finding of the existence of two distinct populations of filopodia, even up to 10 DIV, is in agreement with electron microscopy investigations by Korobova and Svitkina, who showed differences in the cytoskeletal organization of tip and shaft filopodia at 10 DIV, indicative of the persistence of differences in the two populations to more advanced stages of development.[12] For structures as sensitive and as responsive as filopodia, culture condition factors such as substrates, cell density, and growth factors can heavily impact the biological read-out. A 300 μm thick cortical brain slice presents a very different environment compared to a low density dish culture. Filopodia in a slice environment are constantly in contact with other neurites and/or cells. On the other hand, we selectively analyzed free filopodia that were not interacting with other cells in order to ensure uniformity of culture conditions from filpodium to filopodium, since cell contact would itself constitute a confounding influence on filopodial development.[39] This analysis, therefore, highlights the exploratory aspect of a filopodium's activity, in favor of the connection consolidation phase that follows contact with other cells.

In addition to differences in the filopodial presentation parameters of densities and lengths, we also found differences in the behavioral dynamics of tip and shaft filopodia. We analyzed second-to-second changes in filopodial mass achieving femtogram-level resolution using label-free imaging with SLIM. In early stages of development, the two populations showed similar dynamics, except that filopodia at the tips showed faster growth. This could be attributed to the presence of growth cones at the tips which provides a ready pool of actin for quick incorporation into budding filopodia at the tips. Additionally, the higher density of filopodia at the tips implies a higher concentration of actin polymerization and de-polymerization machinery which could aid faster growth.

With further maturation over 7 and 10 DIV, tip filopodia mostly retained their faster dynamics, except for a slight dip in growth rates which could be associated with a reduction in the sizes of growth cones as the cell develops. Interestingly, shaft filopodia showed a significant slowing down by 7 and 10 DIV, with growth and shrinkage rates dropping to half the values observed at 4 DIV. Hence, in the course of dendritic development, tip and shaft filopodia start out with similar dynamics, but progression of neuronal maturation is accompanied by a selective slowing down of the filopodia along the shaft. Such findings make it tempting to consider a transitional model of shaft filopodial development that posits a gradual change in shaft filopodia from early stages, when they are more similar to the conventional filopodium like tip filopodia, to later stages when they begin to slow down, approaching and preparing for the transition to spines and/or synapses. A closer examination of cytoskeletal structure and modulators of

actin dynamics in shaft filopodia in earlier stages of development would help elucidate filopodial behavior in these stages.

As in studies of structure, methodological diversity can be an even greater source of variation for studies of dynamics. Fluorescence-based studies of filopodial motility can usually support only low image acquisition rates for long durations due to photo-toxicity concerns, employing parameters such as acquisition rates of one image every 30 s for a 10 min duration,[13] or even as much as more than 6 min / measurement.[30,40] These protocols fail to capture the second-to-second changes that we were able observe through label-free SLIM imaging. To minimize any other variations and to ensure the highest degree of accuracy, we imposed set guidelines for our analyses. (1) Times where two or more filopodia touched or crisscrossed were not included in the analysis since it is not possible to accurately attribute a certain portion of the dry mass in the field to one filopodium *vs.* the other(s). This also reduces the chances of the alteration in filopodial behavior due to interaction with neighboring filopodia obfuscating the readouts. (2) Another selection factor imposed was that filopodia were analyzed only during those times when they were not touching other neurites or cells, or cell debris. This is because cell-cell contact or topographical cues provided by these is expected to influence filopodial dynamics.[39] A fair comparison would require ensuring that all filopodia analyzed received similar levels of contact-based stimulation, which is not feasible. (3) Finally, cells close to dead or dying cells, as identified by membrane blebbing, were completely excluded from analysis. An intriguing extension of this work would be the examination of these external influences on filopodia – if, and how, a filopodium's

interaction with its neighboring filopodia, with other cells or neurites, and with debris and other topographical features, influence its presentation and behavior.

Another interesting outcome of our analysis was an elucidation of the growth pattern of filopodia. Recent years have seen a number of forays into single-cell mass measurements, but to our knowledge mass variations in subcellular structures remain largely unexplored. The high spatial and temporal resolution of SLIM is uniquely suited to such analyses. Our analysis of filopodial mass variances revealed that filopodia exhibit an exponential growth, that is, the longer the filopodium, the faster it grows (Figure 2.10). This is a finding that has a number of implications for the field. The exponential growth might be demonstrative of the mechanical obstacles faced by a budding filopodium, such as membrane resistance, that might be easier to overcome with increasing mass. It could also hint to a cooperative recruitment of the machinery employed in filopodial extension. Another characteristic feature of systems that show exponential growth is the existence of checkpoints or regulatory systems that keep the growth in check.[19,41] The actin cytoskeletal system that forms the core of filopodial dynamics, is a system that lends itself especially well to control and regulation. The nuances of this regulation and how it pertains to the maintenance of an exponential growth rate in filopodia are questions that merit further investigation.

In conclusion, this work posits the existence of two distinct populations of dendritic filopodia in hippocampal neurons as evidenced by differences in structure and dynamics. Tip filopodia were shown to be longer and presented at higher densities than shaft filopodia, across the progression of neuronal development from 4 to 10 DIV. The high spatial and temporal resolution capabilities of SLIM were employed towards

investigating femtogram-level mass changes in filopodial dynamics. In the early stages of 4 DIV, the two populations displayed similar dynamics, but by 7 and 10 DIV, shaft filopodia slowed down significantly – potentially reflecting a change in the underlying cytoskeleton as has been reported before.[12] Growth dynamics were further examined, revealing filopodial growth to be exponential in nature, with the growth rate increasing with increasing mass. With dendritic filopodia being at the core of the processes of spinogenesis, synaptogenesis and dendritic morphogenesis, these findings will contribute greater comprehension of the processes of neuronal patterning and network formation.

Literature cited

1. y Cajal, S. R. Estructura de los centros nerviosos de las aves. *Rev. Trim. Histol. Norm. Patol.* **1,** 1–10 (1888).

2. Markham, J. A. & Fifková, E. Actin filament organization within dendrites and dendritic spines during development. *Brain Res.* **392,** 263–9 (1986).

3. Landis, D. M. & Reese, T. S. Cytoplasmic organization in cerebellar dendritic spines. *J. Cell Biol.* **97,** (1983).

4. Hirokawa, N. The arrangement of actin filaments in the postsynaptic cytoplasm of the cerebellar cortex revealed by quick-freeze deep-etch electron microscopy. *Neurosci. Res.* **6,** 269–75 (1989).

5. Rácz, B. & Weinberg, R. J. Organization of the Arp2/3 complex in hippocampal spines. *J. Neurosci.* **28,** 5654–9 (2008).

6. Wegner, A. M. *et al.* N-wasp and the arp2/3 complex are critical regulators of actin in the development of dendritic spines and synapses. *J. Biol. Chem.* **283,** 15912–20 (2008).

7. Hering, H. & Sheng, M. Activity-dependent redistribution and essential role of cortactin in dendritic spine morphogenesis. *J. Neurosci.* **23,** 11759–69 (2003).

8. Kim, Y. *et al.* Phosphorylation of WAVE1 regulates actin polymerization and dendritic spine morphology. *Nature* **442,** 814–817 (2006).

9. Ethell, I. M. & Pasquale, E. B. Molecular mechanisms of dendritic spine development and remodeling. *Prog. Neurobiol.* **75,** 161–205 (2005).

10. Tada, T. & Sheng, M. Molecular mechanisms of dendritic spine morphogenesis. *Curr. Opin. Neurobiol.* **16,** 95–101 (2006).

11. Takahashi, H. *et al.* Drebrin-dependent actin clustering in dendritic filopodia governs synaptic targeting of postsynaptic density-95 and dendritic spine morphogenesis. *J. Neurosci.* **23,** 6586–95 (2003).

12. Korobova, F. & Svitkina, T. Molecular architecture of synaptic actin cytoskeleton in hippocampal neurons reveals a mechanism of dendritic spine morphogenesis. *Mol. Biol. Cell* **21,** 165–76 (2010).

13. Portera-Cailliau, C., Pan, D. T. & Yuste, R. Activity-regulated dynamic behavior of early dendritic protrusions: evidence for different types of dendritic filopodia. *J. Neurosci.* **23,** 7129–42 (2003).

14. Zimering, J. H. *et al.* Anesthetic Sevoflurane Causes Rho-Dependent Filopodial Shortening in Mouse Neurons. *PLoS One* **11,** e0159637 (2016).

15. Godin, M. *et al.* Using buoyant mass to measure the growth of single cells. *Nat. Methods* **7,** 387–90 (2010).

16. Bryan, A. K., Goranov, A., Amon, A. & Manalis, S. R. Measurement of mass, density, and volume during the cell cycle of yeast. *Proc. Natl. Acad. Sci. U. S. A.* **107,** 999–1004 (2010).

17. Park, K. *et al.* Measurement of adherent cell mass and growth. *Proc. Natl. Acad. Sci. U. S. A.* **107,** 20691–6 (2010).

18. Park, K. *et al.* 'Living cantilever arrays' for characterization of mass of single live cells in fluids. *Lab Chip* **8,** 1034 (2008).

19. Mir, M. *et al.* Optical measurement of cycle-dependent cell growth. *Proc. Natl. Acad. Sci. U. S. A.* **108,** 13124–9 (2011).

20. Wang, Z. *et al.* Spatial light interference microscopy (SLIM). *Opt. Express* **19,** 1016 (2011).

21. Popescu, G. *et al.* Optical imaging of cell mass and growth dynamics. *Am. J. Physiol. - Cell Physiol.* **295,** (2008).

22. Gabor, D. A New Microscopic Principle. *Nature* **161,** 777–778 (1948).

23. Zernike, F. How I Discovered Phase Contrast. *Science (80-.).* **121,** (1955).

24. Conlon, I. & Raff, M. Differences in the way a mammalian cell and yeast cells coordinate cell growth and cell-cycle progression. *J. Biol.* **2,** 7 (2003).

25. Banker, G. & Goslin, K. in *Cellular and molecular neuroscience series* **2nd Ed., M,** 666 (1998).

26. Millet, L. J., Stewart, M. E., Sweedler, J. V, Nuzzo, R. G. & Gillette, M. U. Microfluidic devices for culturing primary mammalian neurons at low densities. *Lab Chip* **7,** 987–994 (2007).

27. Dickson, B. J. Molecular mechanisms of axon guidance. *Science (80-.).* **298,** 1959–1964 (2002).

28. Dent, E. W. & Gertler, F. B. Cytoskeletal dynamics and transport in growth cone motility and guidance. *Neuron* **40,** 209–227 (2003).

29. Tessier-Lavigne, M. Wiring the brain: the logic and molecular mechanisms of axon guidance and regeneration. *Harvey Lect.* **98,** 103–43

30. Ziv, N. E. & Smith, S. J. Evidence for a role of dendritic filopodia in synaptogenesis and spine formation. *Neuron* **17,** 91–102 (1996).

31. Yuste, R. & Bonhoeffer, T. Genesis of dendritic spines: insights from ultrastructural and imaging studies. *Nat. Rev. Neurosci.* **5,** 24–34 (2004).

32. Vaughn, J. E. Review: Fine structure of synaptogenesis in the vertebrate central nervous system. *Synapse* **3,** 255–285 (1989).

33. Vaughn, J. E., Henrikson, C. K. & Grieshaber, J. A. A quantitative study of synapses on motor neuron dendritic growth cones in developing mouse spinal cord. *J. Cell Biol.* **60,** 664–72 (1974).

34. Fiala, J. C., Feinberg, M., Popov, V. & Harris, K. M. Synaptogenesis via dendritic filopodia in developing hippocampal area CA1. *J. Neurosci.* **18,** 8900–11 (1998).

35. Gao, F.-B. Molecular and cellular mechanisms of dendritic morphogenesis. *Curr. Opin. Neurobiol.* **17,** 525–32 (2007).

36. Scott, E. K. & Luo, L. How do dendrites take their shape? *Nat. Neurosci.* **4,** 359–365 (2001).

37. Chen, Y., Bourne, J., Pieribone, V. A. & Fitzsimonds, R. M. The role of actin in the regulation of dendritic spine morphology and bidirectional synaptic plasticity. *Neuroreport* **15,** 829–32 (2004).

38. Portera Cailliau, C. & Yuste, R. [On the function of dendritic filopodia]. *Rev. Neurol.* **33,** 1158–66

39. Heiman, M. G. & Shaham, S. Twigs into branches: how a filopodium becomes a dendrite. *Curr. Opin. Neurobiol.* **20,** 86–91 (2010).

40. Dailey, M. E. & Smith, S. J. The dynamics of dendritic structure in developing hippocampal slices. *J. Neurosci.* **16,** 2983–94 (1996).

41. Mitchison, J. M. in 165–258 (2003). doi:10.1016/S0074-7696(03)01004-0

Figures

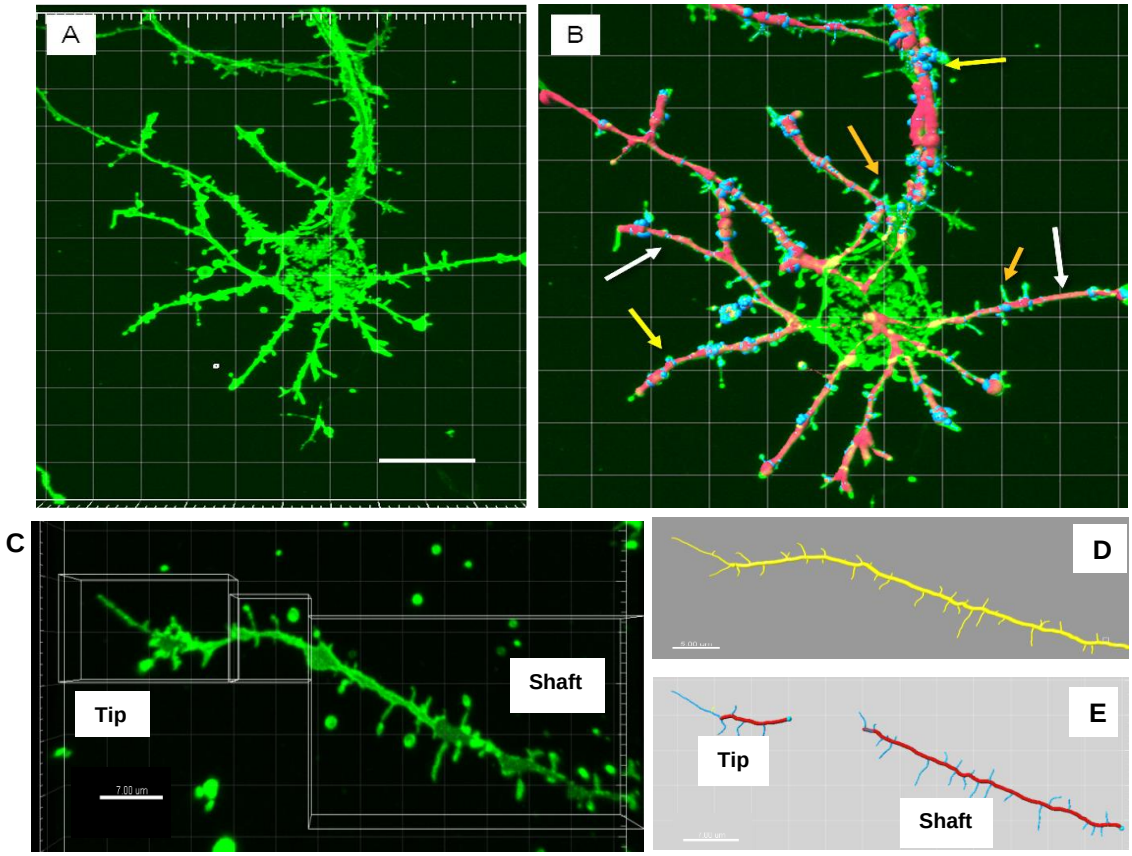

Figure 2.1. Filopodial reconstruction using Imaris (A) Original Z-stack of a 7 DIV hippocampal neuron labeled using membrane dye DiA. Scale bar = 10 µm (B) Final image with neurite reconstruction (red, with white arrows) and spine reconstruction (blue, with yellow arrows). Filopodia are process extensions in green (orange arrows). (C) High-resolution Z-stack image of a DiA labeled dendrite showing demarcation of tip and shaft, showing full filament reconstruction (D) and region-specific reconstruction (E) with dendrite in red and filopodia in blue. Scale bars in C, D, E = 7 µm.

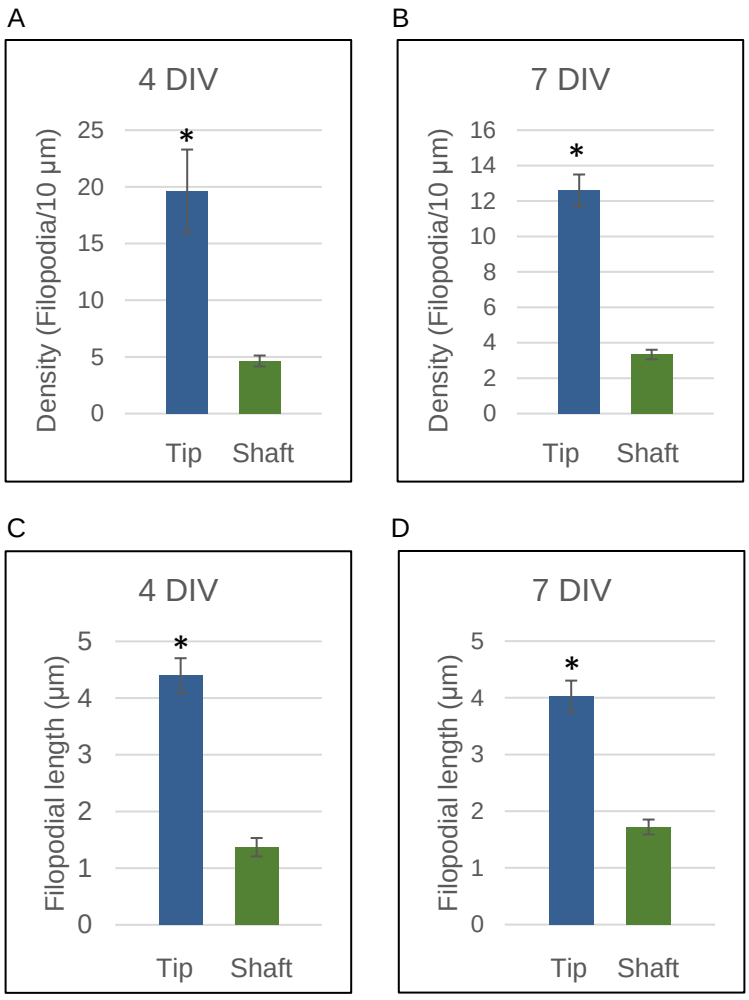

Figure 2.2. Filopodia at dendrite tips are denser and longer than those along shafts. Z-stack images of primary hippocampal neurons at 4, 7, and 10 DIV were reconstructed using Imaris. Filopodial numbers were then quantified and filopodial densities calculated as number of filopodia/10 µm dendrite. (A) At 4 DIV dendrite tips bear a significantly higher density of filopodia: 19.6 filopodia/10 µm at the tips as compared to 4.6 filopodia/10 µm along the shafts (A). (B) The trend persists at 7 DIV with 12.6 filopodia / 10 µm at the tips, and 3.3 filopodia/10 µm at the shafts. Filopodia at the tips were also found to be longer than those along the shafts, both at 4 DIV (C) and 7 DIV (D). Unpaired *t* test, n= 3 dishes per time point, 10 cells per dish, * $p < 0.01$.

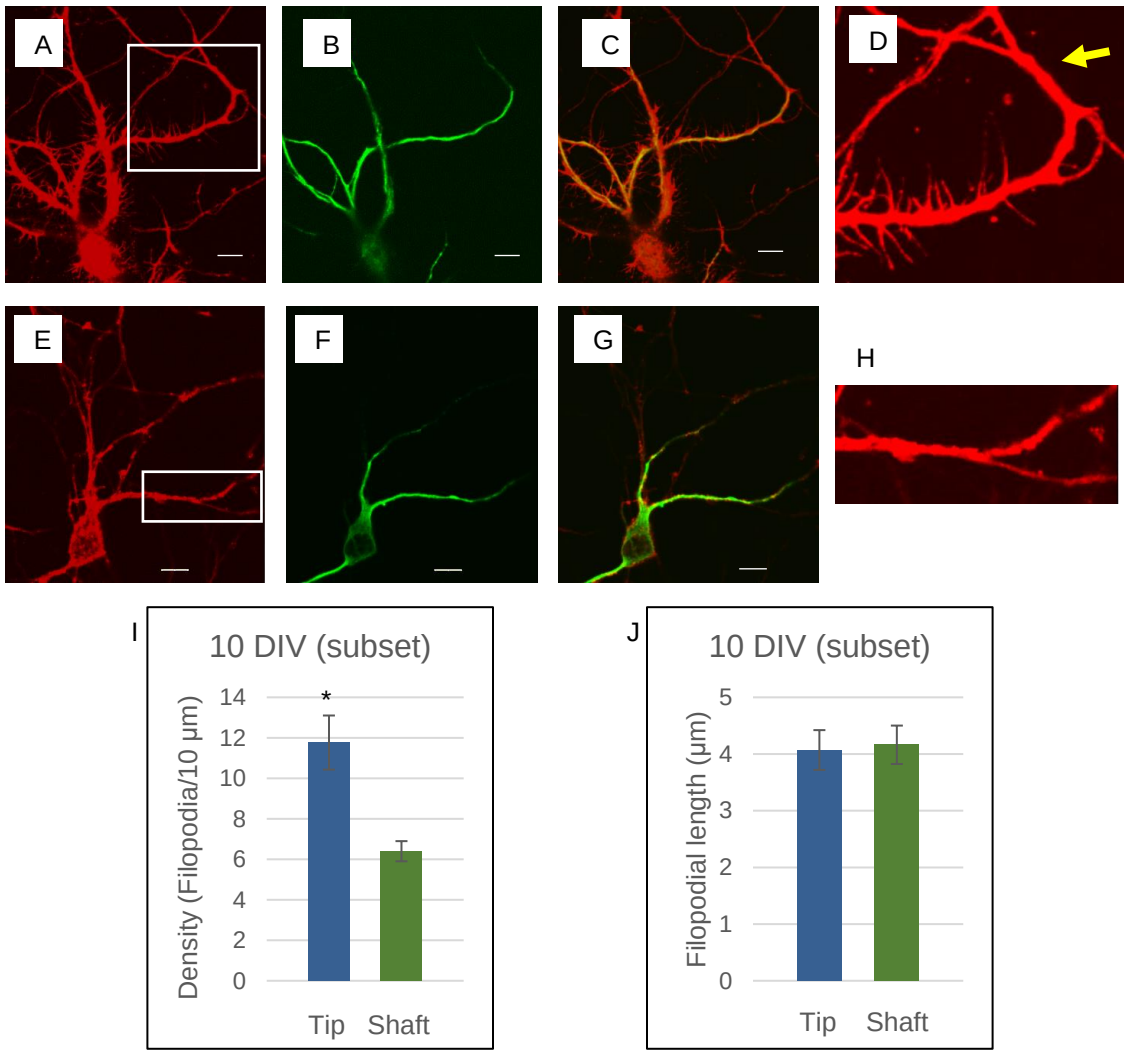

Figure 2.3. Cellular heterogeneity at 10 DIV with differential filopodial expression. Rat primary hippocampal neurons at 10 DIV were fixed and stained for actin (rhodamine-phalloidin, red), and dendrite marker, MAP-2 (Microtubule Associated Protein – 2, green). At this stage, a part of the cellular population continues to bear filopodia at the tips and the shafts (A-D), while the rest have almost none along the shafts (E-H). Dendritic segments in D and H, from boxed regions in A and E, respectively, highlight the difference in filopodial expressions. Even within cells bearing filopodia, distal segments of dendrites were found to be bare (D, yellow arrow). Filopodia-bearing segments were selectively analyzed for filopodial densities (I) and lengths (J). Tip filopodia showed similar numbers as at 4 and 7 DIV, but shaft filopodia, for this subset, were found to be significantly denser and longer. Combining data for the two populations yields values similar to the ones observed at 4 and 7 DIV. Unpaired *t* test, n = 3 dishes/time point, 10 cells/dish, * $p < 0.01$. Scale bar = 10 µm.

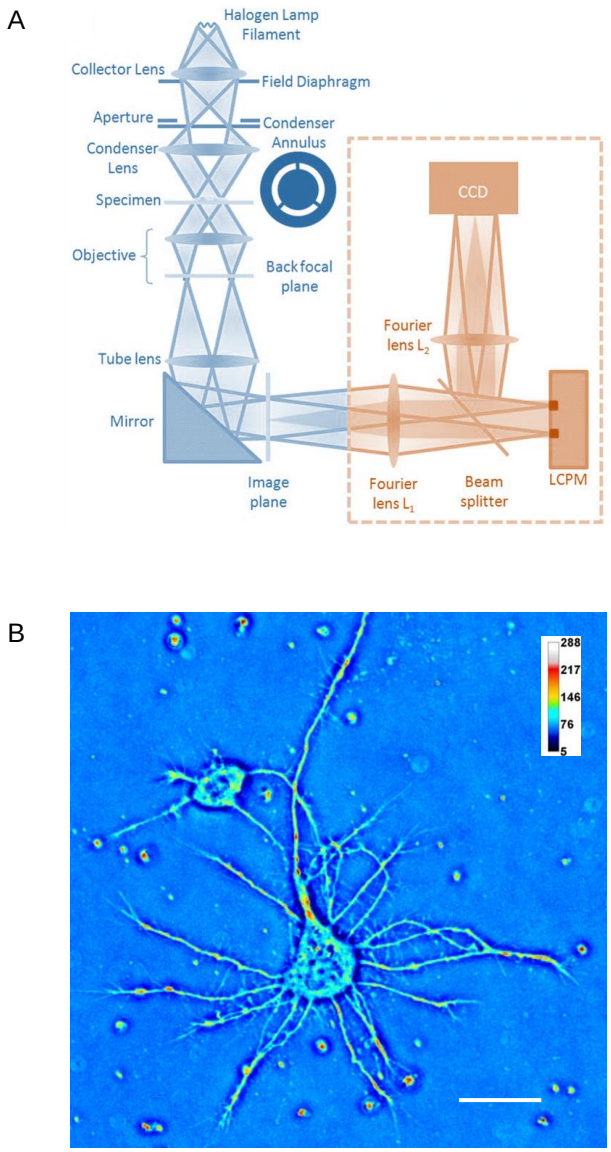

Figure 2.4. Spatial Light Interference Microscopy enables label-free, live-cell analyses. (A) Schematic representation of Spatial Light Interference Microscopy (SLIM) adapted from Wang et al. 2011.[20] The setup includes a SLIM module (orange) installed on a conventional phase contrast microscope (blue). Introduction of additional phase modulation in increments of $\pi/2$ (0, $\pi/2$, π, and $3\pi/2$) through this module, enables the generation of optical path length maps. These correspond to dry mass in the region. (B) Quantitative phase image of a primary rat hippocampal neuron at 4 DIV. Color bar indicates path length in nm, with lower path length corresponding to lower dry mass. Scale bar = 20 μm.

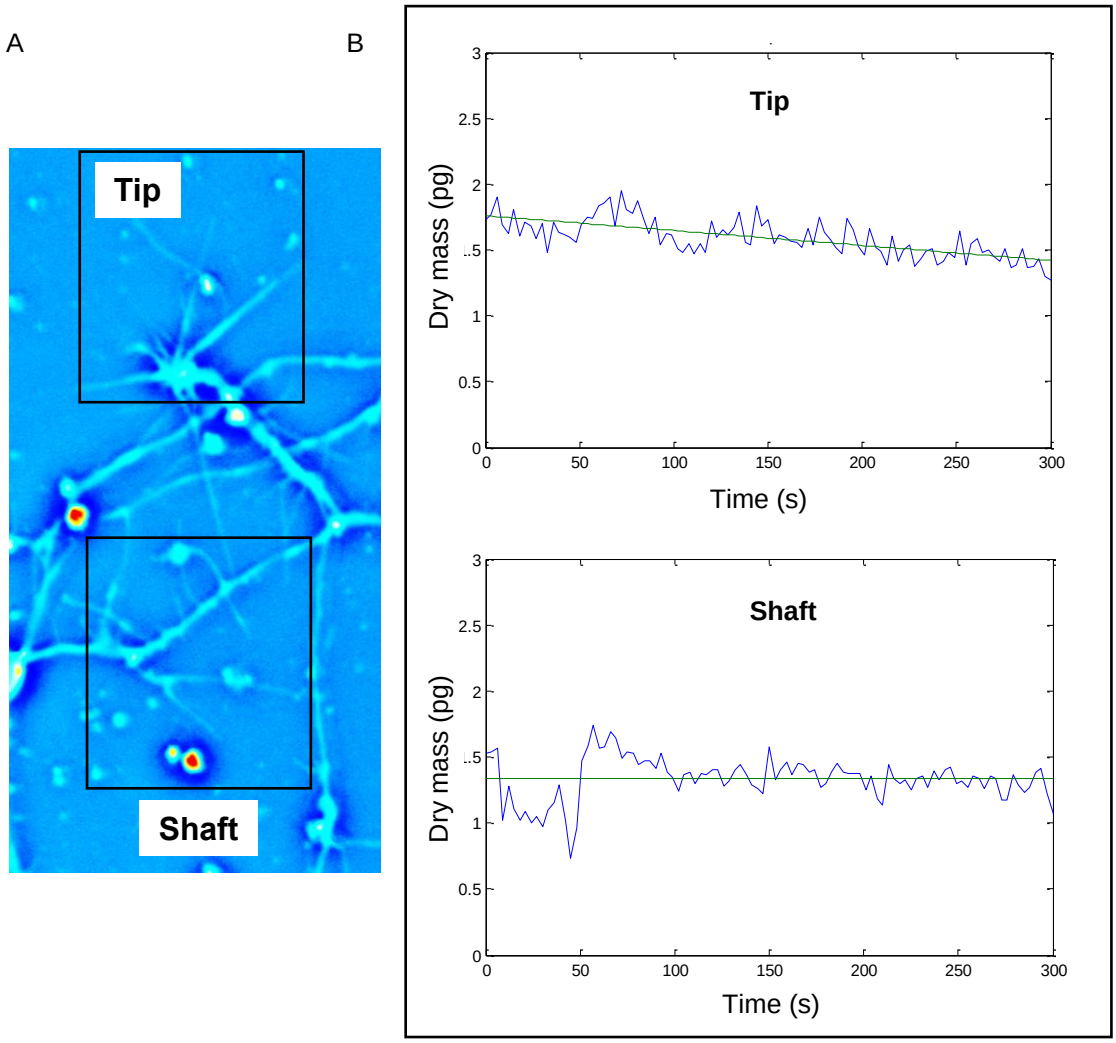

Figure 2.5. Dry mass analysis reveals filopodial retraction at dendrite tips. Phase data from SLIM (A) was used to determine the dry mass in the field of view. Analyzed over time, it was used to decipher extension and retraction trends for neurons at 4 DIV (B). Filopodia at dendrite tips showed a considerable drop in dry mass over time indicative of growth which is accompanied by stabilization of a few filopodia and retraction of the rest. For shaft filopodia, extensions mostly balanced retractions during this phase.

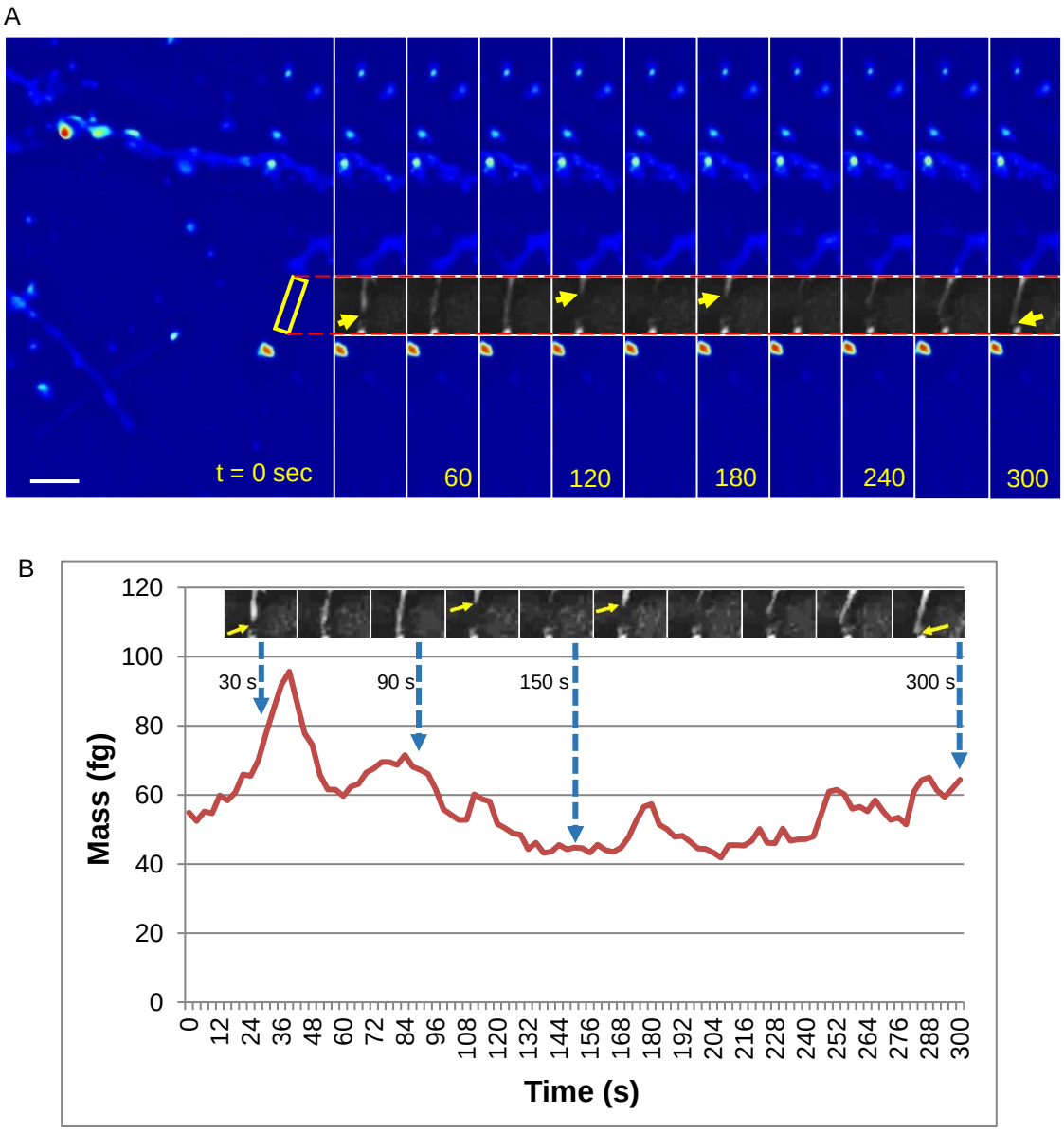

Figure 2.6. Femtogram-level resolution of SLIM enables analysis of individual filopodia. Primary rat hippocampal neurons were imaged at 7 DIV. (A) To analyze the dynamics of an individual tip filopodium, an ROI was drawn around it (yellow box), taking care that it circumscribed the entire field swept by the filopodium in the duration of the time-lapse series, while also minimizing the area enclosed to reduce noise. Scale bar = 0.5 μm. (B) The optical path length data in the ROI was processed to convert grey scale intensity values to phase, and then phase to dry mass, followed by background subtraction. When applied to the time series, this yielded the dry mass changes in the ROI which follow (blue arrows) the extension and retraction of the filopodium (yellow arrows).

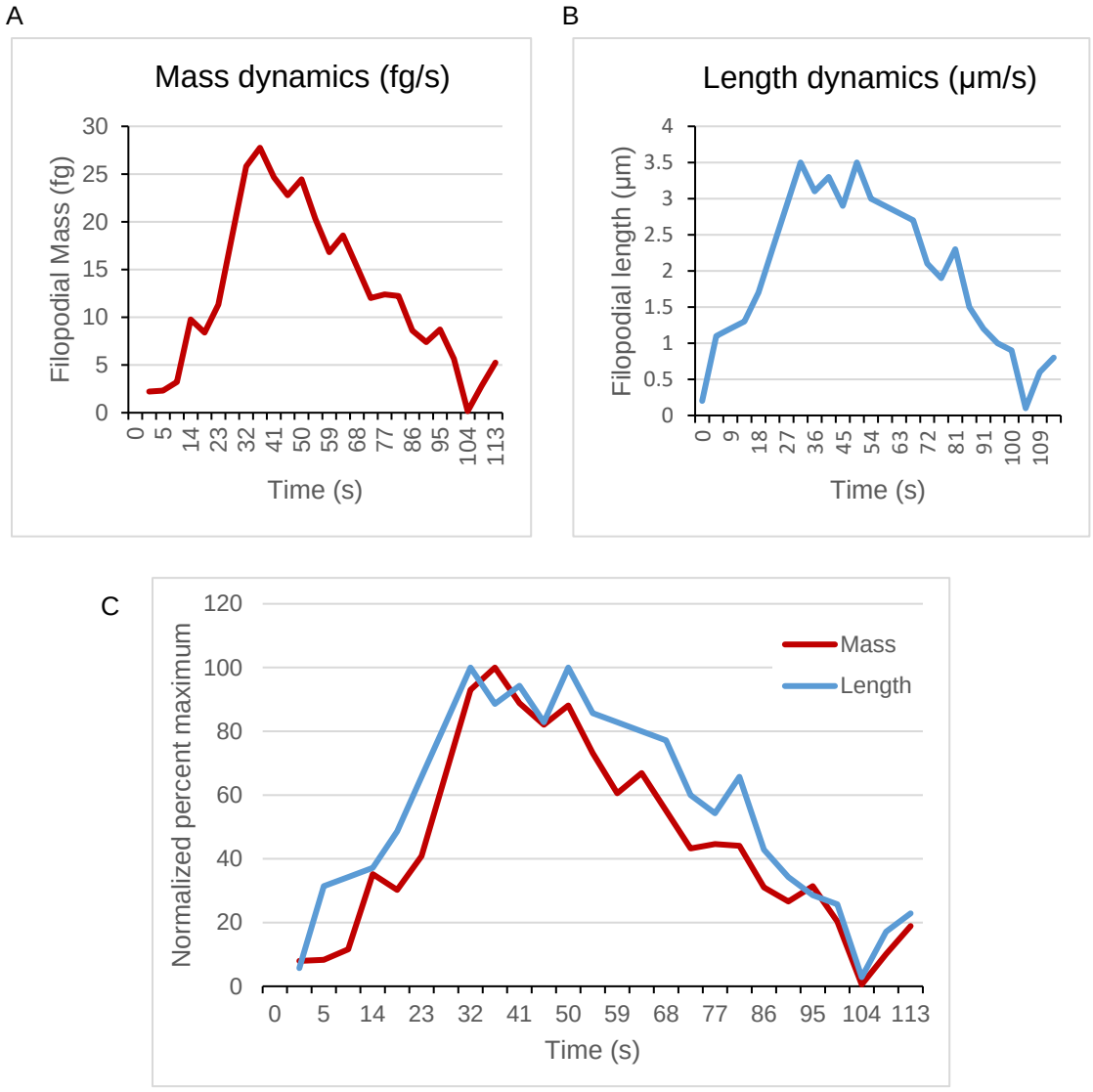

Figure 2.7. Mass-length correlation in SLIM analysis. (A) Phase data from SLIM was used to determine the dry mass in the field of view for a 4 DIV shaft filopodium. (B) The same SLIM-generated image set was analyzed using ImageJ to calculate filopodial length variation over time. (C) Correlation comparison following normalization of the two curves in (A) and (B) emphasizes the fidelity of the analysis system. Correlation coefficient, r = 0.949.

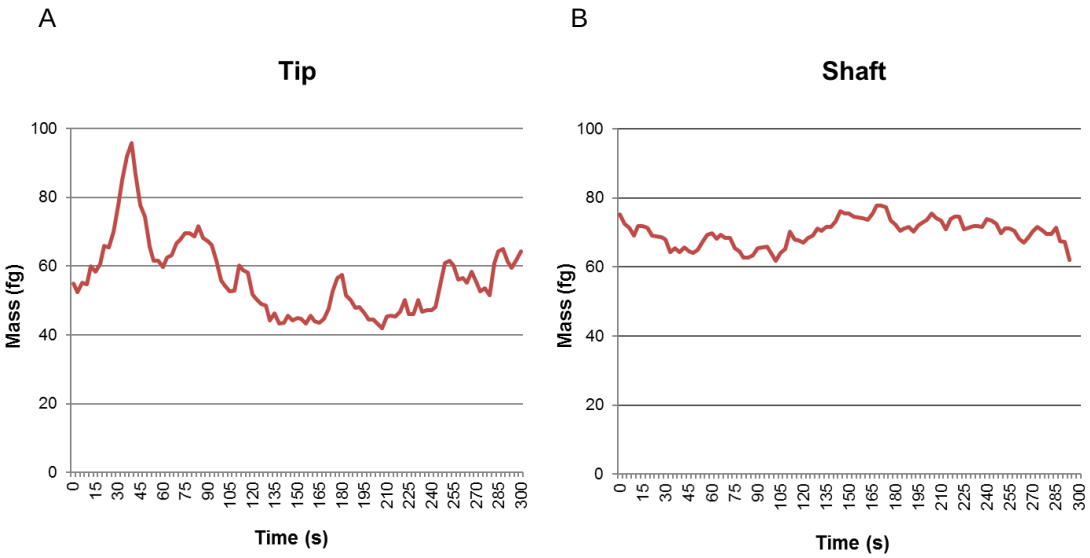

Figure 2.8. Representative traces of mass dynamics. Primary rat hippocampal neurons at 7 DIV were imaged using time-lapse SLIM imaging with images acquired every 3 sec. Phase data so obtained was used to determine the dry mass change in regions of interest containing single filopodia. Tip filopodia typically showed faster dynamics, with greater changes in mass occurring faster, than shaft filopodia as shown in representative traces for tip filopodia (A) and shaft filopodia (B).

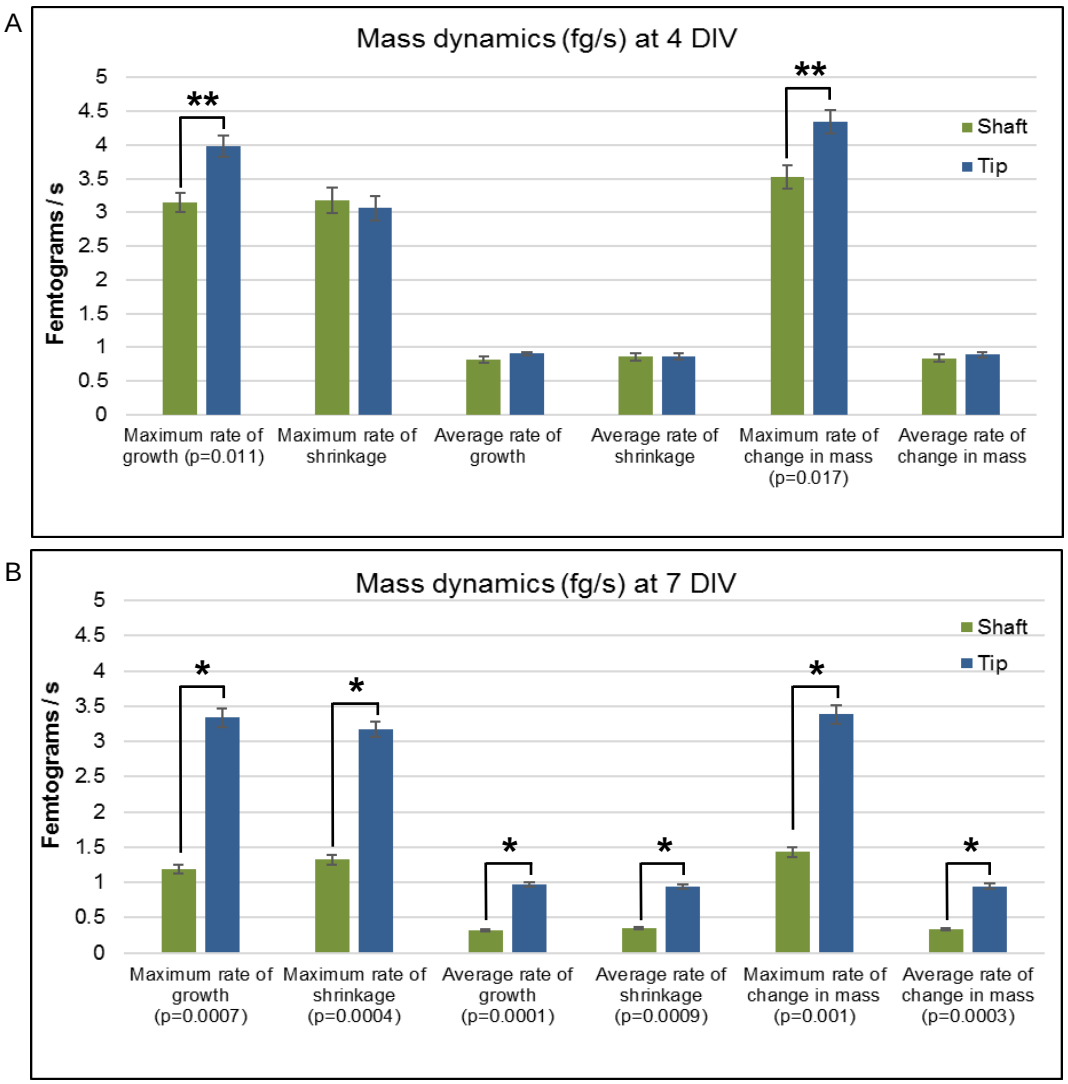

Figure 2.9. Tip and shaft filopodia differ in mass change dynamics and development. Phase data from SLIM at 4 DIV and 7 DIV was used to determine the dry mass change in regions of interest containing single filopodia. With time-lapse imaging every 3 s, mass-change rates for individual filopodia were determined in femtogram/s. (A) At 4 DIV, tip filopodia showed higher values for fastest rate of growth, and fastest change in mass, than did the shaft filopodia. (Unpaired *t* test, n = 3 dishes, with 7 fields of view/dish, with >4 filopodia/field, ** = $p < 0.05$). For other indicators of dynamics, the two populations showed similar values. (B) By 7 DIV, a marked, significant slowing down of dynamics was seen in the shaft filopodia (Unpaired *t* test, n = 3 dishes, with 7 fields of view/dish, >4 filopodia/field, $p < 0.05$ for all parameters examined). Tip filopodia retained their original fast dynamics, except for a dip in their fastest growth rate and fastest mass change (Unpaired *t* test, n = 3 dishes, with 7 fields of view/dish, >4 filopodia/field, $p < 0.05$). Tip filopodia showed faster dynamics than shaft filopodia for all parameters examined. (Unpaired *t* test, n = 3 dishes, with 7 fields of view/dish, >4 filopodia/field, * = $p < 0.01$)

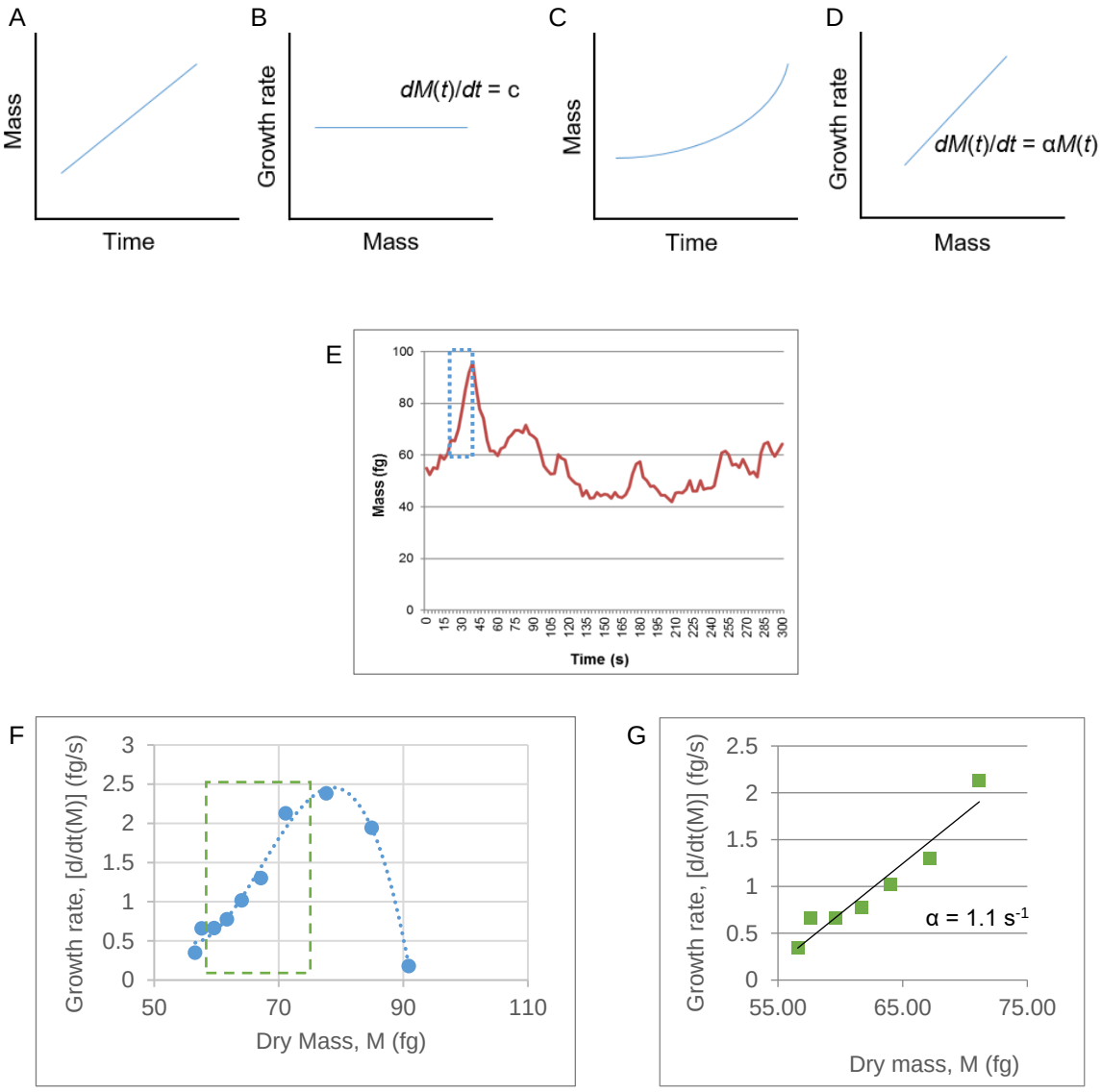

Figure 2.10. Mass dependence of growth rate in filopodia. (A-D) Characteristic traces for linear growth (A, B) and exponential growth (C, D). The former implies a constant rate of change of mass (M) over time, depicted as [d/dt(M) = c] (B), while the latter is characterized by a growth rate that increases with increasing mass, as [dM(t)/dt = αM(t)], where α is the growth rate constant. (E) Representative mass change data from SLIM imaging of a filpodium at 7 DIV. Further analysis of a growth phase (blue box, E) showed that growth rate increased as mass increased, until the filopodium reached close to its peak mass when growth rate dropped (F). (G) Increasing growth rate (green box, F) analyzed selectively, yields a growth constant of 1.1 s^{-1}.

CHAPTER 3: SEMAPHORIN 3A ACCELERATES DENDRITE DEVELOPMENT THROUGH SHAFT FILOPODIA

Abstract

The intricate wiring of the nervous system relies on filopodial navigation to form complex interconnections between neurons through their axons, dendrites, and the cell soma itself. Until recently, cellular investigations into filopodial dynamics had focused primarily on axonal growth cone filopodia. Spurred by technological advances, scientists have now begun to explore the structural and functional landscape of dendritic filopodia. Here we investigate the role of Sema3A in guiding dendritic morphogenesis, spinogenesis, and synaptogenesis. We show that it acts not only at the level of the dendrites, promoting neurite survival and growth, but also at the level of the filopodia. Since there has been some evidence indicating a difference in filopodia borne along dendrite tips vs. those borne along dendrite shafts, we treat the two populations as distinct and tease apart their different responses. Structural analyses of numbers, lengths, and locations are complemented by studies of dynamic functional aspects of growth and shrinkage rates. This is made possible through Spatial Light Interference Microscopy (SLIM), an innovative quantitative phase imaging method that makes possible high-

This study was possible due to a collaboration with Prof. Gabriel Popescu, Department of Electrical and Computer Engineering and Beckman Institute, University of Illinois at Urbana-Champaign, Prof. Popescu provided open access to his innovative imaging equipment and insights determining mass-transport using Scattered Light Interference Microscopy (SLIM). Taewoo Kim, graduate student at the Popescu Lab, helped with image acquisition and dry-mass analysis for one of the repeats of the filopodial dynamics experiments. Support was provided by the National Science Foundation IGERT 0965918 (AJ) and STC CBET 0939511 (MUG, GP), and the National Institutes of Health NIH R21MH085220 and R21MH101655 (MUG).

resolution label-free imaging of live cells through interferometry and allows measurements of the dry mass of live neurons at femtogram levels.[1,2] This convergence of filopodial investigations and the technology for engineering micro-environments, when coupled with high resolution imaging and analysis, enabled new insights on local signals, including Sema3A, that initiate and establish neuron-neuron interactions at the filopodial level. A greater comprehension of such processes that shape the development of neuronal networks is helping unravel the mechanistic bases of developmental disorders and diseases.

Introduction

The establishment of the complex patterns of neuronal connectivity during development relies heavily on guidance molecules that steer migrating neurons and extending neuronal processes to their appropriate targets.[3,4] Semaphorins form a key group among these regulators of neuronal development. They comprise a large, and diverse but phylogenetically conserved family of proteins that include transmembrane and secreted, long-range and short-range guidance molecules, all defined by the presence of a conserved extracellular ~500-amino-acid domain called the semaphorin domain.[5–7] They were initially characterized as exclusively inhibitory in their guidance mechanism, but have since been reported to exhibit attractant behavior as well, with several members of the family being bifunctional.[8,9] The first member of this group to be identified was Fasciclin IV, which was detected in 1992 in the grasshopper embryo through antibody screening and blocking experiments in studies of fasiculating axons.[10] It has since then been renamed as Semaphorin 1a.[10] The first of the semaphorins to be identified in

vertebrates was collapsin-1.[11] It was discovered in 1993 in chickens using an in vitro assay developed to detect axonal growth cone collapse,[12] and was named collapsin for its rapid induction of growth cone collapse in sensory neurons. After a brief period of being known as SemaphorinD, it is today recognized as Semaphorin 3A, or Sema3A, and has several guidance functions attributed to it.

Semaphorins function not only in neuronal development, but also in several other tissues. Sema3A, in particular, has been shown to have several other region-specific guidance effects throughout the body. For instance, it has been implicated in bone remodeling,[13] guidance and remodeling of the vasculature,[14] development of the heart,[15] lung morphogenesis,[16] and potentially even immune cell migration.[17] It has also been reported to regulate tumor progression, inhibiting the spread of breast and prostate cancer cells,[18,19] and contributing to the spread of pancreatic and colon cancers.[20,21]

Within the nervous system, Sema3A's role in neuronal patterning has been found to extend beyond influencing neurites, with studies showing its involvement in guiding neural crest cell migration,[22–24] and the radial migration and regeneration of cortical neurons.[25] However, the most well studied role of Sema3A remains that of neuron guidance, in particular through axonal growth cone repulsion, with a wealth of studies elucidating the roles of collapsin response mediator proteins (CRMPs) and rac1 in the Sema3A signaling pathway,[26–28] its stimulation of endocytosis at the growth cone,[29] underlying cytoskeletal changes[30] and several others.[31] Its guidance effect has been shown to be vital in the development of several brain regions,[32] including steering connections from the entorhinal fibers in the hippocampus[33] and establishing the glomerular sensory map in the olfactory bulb,[34] to name just a few. In addition to acting

as a growth cone repellant, Sema3A instructs axon development through inhibition of axon branching,[8,35] and pruning of axon branches.[36]

Among the most notable features of Sema3A is its contrasting guidance of dendrites. Instructing axons through repulsion, it exerts the exact opposite effect and acts as an attractant for dendrites. Polleux et al. discovered this in 2000, in mouse cortical pyramidal neurons using slice overlay assays and Sema3A knockout mice.[37] They found that Sema3A acts an attractant for apical dendrites and directs their extension towards the pial surface, while at the same time repelling axons into the underlying white matter. This differential regulation at the sub-cellular level is accomplished through differences in cGMP levels in axons and dendrites. Elevation of cGMP levels was found to convert Sema3A mediated repulsion into attraction in *Xenopus* spinal cord neurons,[38] and dendrites of cortical pyramidal neurons have high levels of guanylate cyclase which result in a dendrite-specific cGMP elevation thereby transforming the Sema3A cue into an attractive one. Sema3A has since been shown to enhance dendrite branching as well as extension,[39,40] and to direct the establishment of neuronal polarity in undifferentiated neurites, suppressing their differentiation into axons and promoting dendrite formation.[41]

Being a signaling protein that selectively promotes dendrite survival and growth, Sema3A's effects on the dendritic filopodia are all the more relevant. It has been shown to be involved in dendrite branching, spine maturation and synapse formation, but its differential regulation of these developmental processes at the level of tip and shaft filopodia remains unknown.[40,42]

We take these findings a step further and examine the effects on Sema3A on the presentation and behavior of dendritic filopodia of primary rat hippocampal neurons.

Since there has been some evidence indicating differences in filopodia borne along dendrite tips (10 μm at apical end) and those borne along dendrite shafts,[43,44] we treat the two populations as distinct and tease apart their different responses to Sema3A. We show that Sema3A acts not only at the level of the dendrites, promoting neurite survival and growth, but also at the level of the filopodia, in particular shaft filopodia, accelerating spinogenesis and synaptogenesis, and thereby acting as a key regulator of network formation. We observe that a 24 h exposure to Sema3A at 1 DIV, selectively influences filopodial presentation along the shafts, resulting in an acceleration of maturation, as well as an acceleration of the dynamics of shaft filopodia at 7 DIV detected as mass changes through SLIM imaging. Bath application of Sema3A also elicits an axonal response, which might itself affect the cells as a whole, and could confound the filopodial read out. To avoid this, we supplement bath application studies with investigations using microfluidic devices that enable focal, sub-cellular application of Sema3A.

Here we discuss these selective effects of Sema3A on the development of shaft filopodia, and their consequences towards dendritic morphogenesis, spinogenesis and synaptogenesis.

Materials and methods

Cell culture

Source animal - Long-Evans BluGill rats were used in accordance with protocols established by the University of Illinois Institutional Animal Care and Use Committee and in accordance with all state and federal regulations. Hippocampi were harvested from P1-P2 rat pups following previously published protocols.[45] Hibernate-A (Brain Bits,

Springfield, IL) and Neurobasal-A (Invitrogen) media without phenol red, supplemented with 0.5 mM L-glutamine (Invitrogen), B-27 (Invitrogen), 100 U/ml penicillin and 0.1 mg/ml streptomycin (Sigma) were used for harvesting and culture respectively. Hippocampi were dissected out in ice-cold Hibernate, pooled together and treated with papain (25 U/ml, Worthington) in Hibernate at 37 ^{o}C for 15 min, twice, with gentle shaking every five minutes. The papain-media was aspirated, and the tissue was rinsed with 1 ml fresh Hibernate at 37 ^{o}C. Cells were then mechanically dissociated through trituration with a fire-polished Pasteur pipette in 2 ml Hibernate. The supernatant from two such dissociations was pooled and centrifuged at 1400 rpm for 5 min. The cell pellet was resuspended in 1 ml Neurobasal and the cells were counted using a Haemocytometer, and plated at a density of 125-150 cells / mm^2 on acid-washed, PDL-coated (100 mg/ml poly-D-lysine, Sigma) glass-bottom petri dishes.

Device fabrication and assembly

Devices were prepared as previously described.[46] Briefly, Si-masters were created using photolithography on silicon wafers using SU-8 photoresist with quartz/chromium mask. To ensure easy release of devices, wafers were coated with (tridecafluoro-1,1,2,2-tetrahydrooctyl)trichlorosilane. To prepare devices polydimethylsiloxane, PDMS, (Sylgard 184, Dow Corning) at a pre-polymer:catalyst ratio of 10:1 was poured onto the masters to a thickness of 5-8 mm. The devices were de-gassed in a vacuum chamber and cured at 60 ^{o}C for 2 h. Once cooled, they were peeled off the masters, and inlets and outlets were created using a 4 mm biopsy punch. They were then put through a solvent extraction using HPLC-grade pentane (Fisher Scientific); xylenes isomers plus

ethylbenzene 98.5+% (xylenes) (Sigma); 200 proof ethanol to rid them of un-polymerized oligomers, remaining catalyst and other impurities. Solvent extraction involves submerging the devices in pentane for 16 h, xylene for 1–2 h, xylene for 2–4 h, ethanol for 1–2 h twice, ethanol overnight, and, finally, sterile DI water overnight, followed by 1 day for drying. Ready devices were bonded to coverslips using oxygen plasma. Device bottom side up, and the cover glasses were placed in a plasma generator for a plasma exposure of 50 s to 1 min. Upon removal from the generator, devices were flipped onto the cover glasses with gentle pressure to ensure good conformal contact. They were then autoclaved and the channels coated with PDL for 2 h before seeding cells.

Semaphorin3A treatment

Cells were seeded onto glass-bottom dishes in 1 ml media. Stock solutions were prepared using lyophilized recombinant mouse Semaphorin 3A Fc chimera (5926-S3-025, R&D Systems) reconstituted in PBS with 0.1% BSA, for a stock concentration of 1 μM. After allowing a 30 min period for cells to attach to the substrate, an additional 1 ml of Sema3A containing media was added for final concentrations of 1 nM, 5 nM or 10 nM. For device cultures, after the attachment period, media in the channels was replaced by introducing Sema3A containing media at the final concentration of 1 nM, at the inlet and reactivating flow by removing media from the outlet. After 24 h of Sema3A exposure, the media was gently aspirated and the cells rinsed with fresh Neurobasal. Fresh Neurobasal was added (2 ml for the dishes, and 40 μl for devices) and the cells

were returned to the incubator. For controls, the treatment solution was PBS with 0.1% BSA without any semaphorin.

Cell labeling and immunochemistry

DiA was used to stain cell membranes, by incubating the cells in a staining solution containing 2 µl DiA and 2 µl Dimethyl Sulfoxide (DMSO) in 2 ml Neurobasal for 10 min, followed by a 5 min PBS rinse. For antibody labeling, cells were fixed with paraformaldehyde (4%) with 4% sucrose for 15 min, permeabilized using TritonX-100 (0.25% in PBS) for 10 min and blocked with 5% Normal Goat Serum (NGS) for 30 min. Cells were incubated with primary and secondary antibodies in 2% NGS for 1 h each. Primary antibody used was anti-MAP-2 (1:1000, Molecular Probes), and secondary antibodies were Alexa Fluor 488 and/or Alexa Fluor 568 secondary antibodies (1:1000, Molecular Probes). Alternatively, for filopodial visualization using phalloidin, fixed and permeabilized cells were incubated with 5 U/ml rhodamine conjugated phalloidin (Thermo Fisher Scientific) for 20 min. Each step was followed by 5 quick rinses and one 5-min rinse with PBS.

Microscopy and data analysis

For structural studies using DiA, neurons at 4, 7, and 10 DIV were imaged on a laser-equipped Zeiss LSM-510 Meta NLO confocal microscope. Z-stacks were acquired with a slice thickness of 0.5-1 µm, at 100x magnification for filopodial studies (Chapter 2, Figure 2.1A). Imaris (Bitplane) was used for reconstruction and 3D-visualiztion of the stacks, and also for the subsequent quantification of cellular and filopodial parameters.

The tip and shaft regions of dendrites, confirmed through a second staining with dendrite marker Microtubule Associated Protein 2, MAP2, were then analyzed individually through 3D-reconstructions of the Z-stacks using Imaris software from Bitplane (Chapter 2, Figure 2.1B and 2.1D). The distal 10 μm of dendrites, inwards from dendritic end points, were designated as 'tip' (Chapter 2, Figure 2.1C and 2.1E). The next 5 μm inwards from the tip region were excluded from analysis since this is likely to be a zone of transition from tip-like characteristics to shaft-like characteristics. The remaining length of the dendrite, leaving out the 10 μm tip region and the 5 μm transition zone, was designated as the 'shaft' (Chapter 2, Figure 2.1C and 2.1E). All results obtained with DiA labeling and Imaris analysis were validated with rhodamine-phalloidin labelling. Rhodamine-phalloidin stained cells were imaged on a Zeiss LSM 880 NLO confocal microscope at 63x, and analyzed using ImageJ.

For dynamic analyses, live cells were imaged on an Axiovert fluorescence microscope equipped with a Spatial Light Interference Microscopy (SLIM) module to collect phase data. Images were acquired at 63x magnification every 1.5-3.0 s for a total of 5 min for each field of view. Background elimination, thresholding, and Region of Interest (ROI) selections were performed using ImageJ. Raw phase data was processed using MATLAB, or Dry Mass plugin (Phi Optics) on ImageJ and analyzed using Microsoft Excel.

Variable polygon ROI selections in ImageJ were employed to analyze the behavior of individual filopodia. ROI's were drawn around each filopodium analyzed, such that they circumscribed the entire field swept by the filopodia in the duration of the time-lapse image series, while also minimizing the area enclosed in order to reduce noise.

Each ROI was then individually processed to convert grey scale images to phase, and phase to dry mass, followed by background subtraction. When applied to entire time series this yields dry mass changes over time for single filopodia.

Results

Semaphorin3A is present in the hippocampus in early stages of development, guiding neuronal development to generate the layered architecture of the hippocampus. Experiments were designed with this early stage exposure in mind. Primary rat hippocampal neurons seeded onto dishes or into microfluidic devices were allowed one hour to attach to the substrate, after which Sema3A containing media was introduced for a final concentration of 1 nM, and 5 or 10 nM, for a 24 h treatment phase (Figure 3.1A).

STRUCTURAL ANALYSES

Sema3A treatment selectively increases filopodial density along dendritic shafts

Neurons from treated and control cultures were fixed and stained using membrane stain DiA. In order to determine filopodial densities within sub-regions of dendrites, tips *vs.* shafts were analyzed by counting the number of filopodial end-points / unit dendrite length. Filopodia at the distal 10 μm of dendrite shafts were designated as tip filopodia, with the next 5 μm inwards being excluded from analysis as a transition zone, and filopodia borne along the remaining length of the dendrite designated as shaft filopodia.

At 4 DIV Sema3A treated cells showed an increase in filopodial densities from 2.6 filopodia / 10 μm for controls to 4.67 filopodia / 10 μm along dendritic shafts (Unpaired *t* test, n = 10, p = 0.0310, Figure 3.1B). This increased filopodial density along

the shaft could form the basis of the increased branching in the dendritic arbor seen in response to Sema3A exposure. There was no significant increase in filopodial densities along the tips (Figure 3.1C). This might be because the tips are already densely packed with filopodia. No significant variation was seen in the width, lengths or volumes of filopodia at 4 DIV.

Sema3A promotes filopodial maturation to spines along the shafts

By the 7 DIV stage, dendritic filopodia start maturing. Some of those that are not retracted form the foundation for laying down of new dendritic branches – as seen in the increased branching induced by Sema3A exposure. Other stabilized filopodia go on to form the complex structures of spines and/or synapses. Spines are typically characterized by a mushroom or stub shape with a bulbous 'head' connected to the dendrite through a narrow 'neck' region. Maturation to spine morphology can therefore be inferred from a ratio of maximum width of the head region to the minimum width of the neck region. We term this ratio the maturation coefficient (Figure 3.2A). These coefficients were calculated for tip and shaft filopodia for neurons at 4 and 7 DIV, with and without Sema3A treatments. As expected, at the 4 DIV stage filopodia were mostly immature and rod-like in morphology. However, by the 7 DIV stage filopodial maturation to spines starts becoming evident. Shaft filopodia of neurons treated with 1 nM Sema3A at 1 DIV showed higher values of maturation coefficients than untreated controls, indicative of an acceleration of filopodial maturation towards a spine morphology (Two-way ANOVA, $n = 5$, $p = 0.0015$, Figure 3.2B). No such increase was observed for tip filopodia, implying that this is a shaft-filopodia-specific response.

Sema3A promotes synaptogenesis

Synapses were visualized using synapse marker PSD-95 at days 10 and 14. Area and volume of PSD-95 clusters were estimated using 3D reconstruction of Z-stacks with Imaris. PSD-95 distribution is not uniform along neurite lengths, with lower order thicker branches closer to the soma bearing more clusters. Hence instead of number of PSD-95 clusters per unit dendrite length, more accurate measures are total PSD-95 cluster area per unit dendrite area, and PSD-95 cluster volume per unit dendrite volume. Sema3A treatment at 1 nM and 5 nM led to a significant increase in both these measures (One-way ANOVA, $n = 16$, $p = 0.005$ for area and $p = 0.03$ for volume, Figure 3.3). There was no significant difference in the volume distribution among these clusters (Figure 3.4) suggesting that Sema3A increases clustering while also initiating formation of new clusters.

Compartmentalized cultures enable selective stimulation

Since Sema3A is a repulsive cue for axons, Sema3A-induced axonal repulsion could lead to an adverse response at the level of the whole cell. Such suppressive effects might affect filopodial read outs. To prevent such overflow of the adverse effects of axonal repulsion, microfluidic devices were incorporated into the experimental design to enable selective stimulation of dendrites only through device-assisted compartmentalization of neurons (Figure 3.5). As shown in the schematic, the device consisted of 3 parallel channels connected by narrow inter-connecting channels (or interconnects) 3 μm x 3 μm, and 45 μm long (Figure 3.5A). Flow rates of 0.1-1 nl/sec achieved through gravity-induced flow were found to be optimum for microdevice

cultures, and also enabled introduction of Sema3A into the central channel, while restricting the cell bodies to the side channel(s) (Figure 3.5B). Fluidic isolation tests were performed to confirm the absence of any fluid exchange among the channels (Figure 3.6) to endure that the Sema3A treatment was restricted to the neurite compartment, and did not leak into the cell body channel. This allowed selective stimulation of dendritic filopodia in environments that enabled high spatio-temporal control over the application of Sema3A guidance cues at varying concentrations (Figure 3.5C). Even with this selective stimulation, tip filopodia did not show increases in densities, or spine and synapse formation. Increases for shaft filopodia, for all three measures, were similar to those obtained using dish analyses and bath application of Sema3A.

FUNCTIONAL ANALYSES

Dendrites of live neurons were analyzed for their filopodial dynamics. Due to the high-resolution and fast acquisition rate requirements, high-levels of accompanying photo-toxicity rules out most fluorescence-based techniques for such analyses. On the other hand, label-free Spatial Light Interference Microscopy (SLIM),[1] a quantitative phase imaging based technique, proved ideal for capturing filopodial dynamics.

Sema3A treated tip filopodia show a more deterministic motion

Primary rat hippocampal neurons at 4 DIV were imaged using time-lapse SLIM with images acquired every 3 seconds for 5 minutes. The dynamics captured were analyzed through dispersion-relation phase spectroscopy (DPS)[1] using ROI selections for selective tip *vs.* shaft analysis. This yielded a comparison of the movements of the tip

filopodia and the shaft filopodia with and without Sema3A (Figure 3.7). Tip filopodia were seen to be faster, and addition of Sema3A made the filopodial explorations more deterministic.

Sema3A accelerates average growth and shrinkage rates for shaft filopodia only

Neurons at 4, 7 and 10 DIV were imaged using SLIM and neurites confirmed as dendrites through post-imaging MAP2 staining were selected for filopodial dry mass analysis. For these neurites, regions of interest containing individual filopodia at the tips and shafts were selectively analyzed for changes in dry mass. These changes were used to compute growth and shrinkage rates as indicators of filopodial dynamics. Sema3A administered for 24 h at 0-1 DIV led to increases in average growth and shrinkage rates for shaft filopodia (Figure 3.8) at 7 DIV, with average growth rate increasing from 0.32 fg/s to 0.9 fg/s (One-way ANOVA, $n = 12$, $p < 0.05$), and average shrinkage rate going from 0.35 fg/s to 0.95 fg/s (One-way ANOVA, $n = 12$, $p < 0.05$) with the administration of 1nM Sema3A. This upswing was not observed for tip filopodia at any developmental stage, or for shaft filopodia at 4 and 10 DIV. The maximum rates of growth and shrinkage, i.e., the fastest that a filopodium was seen to grow and shrink, increased for tip and shaft filopodia, at 4 and 7 DIV. For instance, for shaft filopodia at 7 DIV the maximum growth rate increased from 1.2 fg/s to 3 fg/s, and the maximum rate of shrinkage increased from 1.3 fg/s to 3.5 fg/s (One-way ANOVA, $n = 12$, $p < 0.05$).

Discussion

A majority of studies into neuronal development treat the dendrite as a homogenous region, clubbing together filopodia borne along the shafts with those borne at or near the tips of the dendrites. Portera-Cailliau et al. showed in 2003, that growth cone filopodia differ from shaft filopodia, in terms of densities and lengths, and in their response to blocking of synaptic transmission, and of ionotropic glutamate receptors.[44] With their system of choice of acute slices of the mouse neocortex, they observed these differences only up to the P5 stage of development. In 2010, Korobova and Svitkina reported the existence of a different actin organization in shaft filopodia at 10 DIV.[43] This work fills the gap between those two studies, investigating differences between tip and shaft filopodia at 4, 7, 10 and 14 DIV, and examining structure and dynamics, (Chapter 2), as well as responses to developmental cues, specifically, Sema3A.

Sema3A is a unique cue, in that it acts as a repulsive cue to axons, and an attractive cue to dendrites. Furthermore, it not only induces an increase in dendritic length and branching, but also accelerates spine and synapse formation. We found that semaphorin affects tip and shaft filopodia differentially – affecting an increase in the densities of shaft filopodia, but not tip filopodia. It also induced an increased branching of the dendritic arbor – a potential outcome of the increase density of the shaft filopodia. In the advanced stages of neuronal development of 7, 10 and 14 DIV, we found that it selectively influences the maturation of shaft filopodia. Shaft filopodia on neurons that had been exposed to Sema3A at 1 DIV, showed an acceleration of spinogenesis at 7 DIV measured as a thickening of the filopodial head region, and an increase in synaptogenesis indicated by an increased clustering of PSD-95. Neither of these effects was seen in tip

filopodia. This suggests that these two populations are not only different in terms of structure and dynamics, but are also functionally distinct, all through development.

To further understand the mechanism of this differential action of Sema3A we examined the dynamics of filopodia of neurons that had been treated with Sema3A. Dispersion-relation phase spectroscopy analysis showed that Sema3A treatment made the exploratory movements of the tip filopodia more deterministic, rather than diffusive. This indicates the progress towards a more directed growth, rather than random explorations, which could contribute to the greater dendritic lengths observed in Sema3A treated dendrites, since the energy of random explorations can now be invested in more directed growth. Further examination of dynamics showed that Sema3A selectively increases average growth and shrinkage rates in shaft filopodia at 7 DIV. This selective influence might be the basis of increase spinogenesis and synaptogenesis seen in Sema3A treated dendrites, with more and faster explorations resulting in more successful maturations into spines and synapses. Maximum growth and shrinkage rates, which are a measure of the fastest growth and shrinkage seen in filopodia, were seen to increase for both tip and shaft filopodia at 4 and 7 DIV. These faster movements are relatively rare, but could contribute to some of the increase in successful stabilizations into branches, spines and synapses observed upon Sema3A stimulation.

Differential responses to cues have been attributed to variations in cyclic nucleotide levels. Semaphorin3A acts as a repulsive cue for axons and an attractive cue for dendrites due to different cGMP levels. Variations in calcium levels can similarly elicit different responses from different sub-cellular regions. An investigation into the intracellular environments of tip and shaft filopodia, such as levels of cyclic nucleotides

and calcium, would help in further elucidating the mechanism of the differential influence of Sema3A on the two populations. Another avenue that promises answers to some of the questions raised here, is a closer examination of the cytoskeletal organization in shaft filopodia in the earlier developmental stages of 4 and 7 DIV – do these filopodia start out with a crisscross branched actin network organization? Or do early shaft filopodia resemble tip filopodia in possessing a parallel actin bundle organization, and only late stage shaft filopodia mature into a crisscross organization as a transition to the cytoskeletal organization of spines and post-synaptic structures.

In conclusion, Sema3A is a unique cue that acts on both tip filopodia and shaft filopodia, the former to increase dendrite lengths, and the latter to increase branching, spinogenesis and synaptogenesis. This compounds evidence for the two filopodial populations being distinct, not only in terms of structure and dynamics, but also functionally, in their responses to developmental cues, specifically Sema3A. This advancement in our understanding of neuronal filopodia and their diversity will help decode the signaling processes that contribute to a dendritic filopodium's maturation into a spine, a synapse, or a dendritic branch.

Literature cited

1. Wang, Z. *et al.* Spatial light interference microscopy (SLIM). *Opt. Express* **19,** 1016 (2011).

2. Mir, M. *et al.* Optical measurement of cycle-dependent cell growth. *Proc. Natl. Acad. Sci. U. S. A.* **108,** 13124–9 (2011).

3. Dickson, B. J. Molecular mechanisms of axon guidance. *Science (80-.).* **298,** 1959–1964 (2002).

4. Tessier-Lavigne, M. & Goodman, C. S. The molecular biology of axon guidance. *Science* **274,** 1123–33 (1996).

5. Tran, T. S., Kolodkin, A. L. & Bharadwaj, R. Semaphorin Regulation of Cellular Morphology. *Annu. Rev. Cell Dev. Biol.* **23,** 263–292 (2007).

6. Kolodkin, A. L. & Tessier-Lavigne, M. Mechanisms and molecules of neuronal wiring: a primer. *Cold Spring Harb. Perspect. Biol.* **3,** (2011).

7. Goodman, C. ., Kolodkin, A. ., Luo, Y., Püschel, A. . & Raper, J. . Unified Nomenclature for the Semaphorins/Collapsins. *Cell* **97,** 551–552 (1999).

8. Bagnard, D., Lohrum, M., Uziel, D., Puschel, A. W. & Bolz, J. Semaphorins act as attractive and repulsive guidance signals during the development of cortical projections. *Development* **125,** (1998).

9. de Castro, F., Hu, L., Drabkin, H., Sotelo, C. & Chédotal, A. Chemoattraction and chemorepulsion of olfactory bulb axons by different secreted semaphorins. *J. Neurosci.* **19,** 4428–36 (1999).

10. Kolodkin, A. L. *et al.* Fasciclin IV: sequence, expression, and function during growth cone guidance in the grasshopper embryo. *Neuron* **9,** 831–45 (1992).

11. Luo, Y., Raible, D. & Raper, J. A. Collapsin: a protein in brain that induces the collapse and paralysis of neuronal growth cones. *Cell* **75,** 217–27 (1993).

12. Raper, J. A. & Kapfhammer, J. R. The enrichment of a neuronal growth cone collapsing activity from embryonic chick brain. *Neuron* **4,** 21–29 (1990).

13. Fukuda, T. *et al.* Sema3A regulates bone-mass accrual through sensory innervations. *Nature* **497,** 490–493 (2013).

14. Serini, G. *et al.* Class 3 semaphorins control vascular morphogenesis by inhibiting integrin function. *Nature* **424,** 391–7 (2003).

15. Behar, O., Golden, J. A., Mashimo, H., Schoen, F. J. & Fishman, M. C. Semaphorin III is needed for normal patterning and growth of nerves, bones and heart. *Nature* **383,** 525–8 (1996).

16. Ito, T. *et al.* Repulsive axon guidance molecule Sema3A inhibits branching morphogenesis of fetal mouse lung. *Mech. Dev.* **97,** 35–45 (2000).

17. Delaire, S. *et al.* Biological activity of soluble CD100. II. Soluble CD100, similarly to H-SemaIII, inhibits immune cell migration. *J. Immunol.* **166,** 4348–54 (2001).

18. Bachelder, R. E. *et al.* Competing autocrine pathways involving alternative neuropilin-1 ligands regulate chemotaxis of carcinoma cells. *Cancer Res.* **63,** 5230–3 (2003).

19. Herman, J. G. & Meadows, G. G. Increased class 3 semaphorin expression modulates the invasive and adhesive properties of prostate cancer cells. *Int. J. Oncol.* **30,** 1231–8 (2007).

20. Nguyen, Q.-D. *et al.* Inhibition of vascular endothelial growth factor (VEGF)-165 and semaphorin 3A–mediated cellular invasion and tumor growth by the VEGF signaling inhibitor ZD4190 in human colon cancer cells and xenografts. *Mol. Cancer Ther.* **5,** (2006).

21. Müller, M. W. *et al.* Association of axon guidance factor Semaphorin 3A with poor outcome in pancreatic cancer. *Int. J. Cancer* **121,** 2421–2433 (2007).

22. Eickholt, B. J., Mackenzie, S. L., Graham, A., Walsh, F. S. & Doherty, P. Evidence for collapsin-1 functioning in the control of neural crest migration in both trunk and hindbrain regions. *Development* **126,** 2181–9 (1999).

23. Roffers-Agarwal, J. & Gammill, L. S. Neuropilin receptors guide distinct phases of sensory and motor neuronal segmentation. *Development* **136,** 1879–88 (2009).

24. Schwarz, Q., Maden, C. H., Vieira, J. M. & Ruhrberg, C. Neuropilin 1 signaling guides neural crest cells to coordinate pathway choice with cell specification. *Proc. Natl. Acad. Sci. U. S. A.* **106,** 6164–9 (2009).

25. Chen, G. *et al.* Semaphorin-3A guides radial migration of cortical neurons during development. *Nat. Neurosci.* **11,** 36–44 (2008).

26. Goshima, Y., Nakamura, F., Strittmatter, P. & Strittmatter, S. M. Collapsin-induced growth cone collapse mediated by an intracellular protein related to UNC-33. *Nature* **376,** 509–14 (1995).

27. Kuhn, T. B., Brown, M. D., Wilcox, C. L., Raper, J. A. & Bamburg, J. R. Myelin and Collapsin-1 Induce Motor Neuron Growth Cone Collapse through Different Pathways: Inhibition of Collapse by Opposing Mutants of Rac1. *J. Neurosci.* **19,** (1999).

28. Jin, Z. & Strittmatter, S. M. Rac1 Mediates Collapsin-1-Induced Growth Cone Collapse. *J. Neurosci.* **17,** (1997).

29. Fournier, A. E. *et al.* Semaphorin3A enhances endocytosis at sites of receptor-F-actin colocalization during growth cone collapse. *J. Cell Biol.* **149,** 411–421 (2000).

30. Fan, J., Mansfield, S. G., Redmond, T., Gordon-Weeks, P. R. & Raper, J. A. The organization of F-actin and microtubules in growth cones exposed to a brain-derived collapsing factor. *J. Cell Biol.* **121,** 867–78 (1993).

31. Kitsukawa, T. *et al.* Neuropilin-semaphorin III/D-mediated chemorepulsive signals play a crucial role in peripheral nerve projection in mice. *Neuron* **19,** 995–1005 (1997).

32. Giger, R. J., Pasterkamp, R. J., Heijnen, S., Holtmaat, A. J. G. D. & Verhaagen, J. Anatomical distribution of the chemorepellent semaphorin III/collapsin-1 in the adult rat and human brain: Predominant expression in structures of the olfactory-hippocampal pathway and the motor system. *J. Neurosci. Res.* **52,** 27–42 (1998).

33. Steup, A., Ninnemann, O., Savaskan, N. E., Püschel, R. N. andreas W. & Skutella, T. Semaphorin D acts as a repulsive factor for entorhinal and hippocampal neurons. *Eur. J. Neurosci.* **11,** 729–734 (1999).

34. Taniguchi, M. *et al.* Distorted odor maps in the olfactory bulb of semaphorin 3A-deficient mice. *J. Neurosci.* **23,** 1390–7 (2003).

35. Dent, E. W., Barnes, A. M., Tang, F. & Kalil, K. Netrin-1 and Semaphorin 3A Promote or Inhibit Cortical Axon Branching, Respectively, by Reorganization of the Cytoskeleton. *J. Neurosci.* **24,** (2004).

36. Bagri, A., Cheng, H.-J., Yaron, A., Pleasure, S. J. & Tessier-Lavigne, M. Stereotyped Pruning of Long Hippocampal Axon Branches Triggered by Retraction Inducers of the Semaphorin Family. *Cell* **113,** 285–299 (2003).

37. Polleux, F., Morrow, T. & Ghosh, A. Semaphorin 3A is a chemoattractant for cortical apical dendrites. *Nature* **404,** 567–73 (2000).

38. Song, H. *et al.* Conversion of Neuronal Growth Cone Responses from Repulsion to Attraction by Cyclic Nucleotides. *Science (80-.).* **281,** (1998).

39. Fenstermaker, V., Chen, Y., Ghosh, A. & Yuste, R. Regulation of dendritic length and branching by semaphorin 3A. *J. Neurobiol.* **58,** 403–12 (2004).

40. Morita, A. *et al.* Regulation of dendritic branching and spine maturation by semaphorin3A-Fyn signaling. *J. Neurosci.* **26,** 2971–80 (2006).

41. Shelly, M. *et al.* Semaphorin3A Regulates Neuronal Polarization by Suppressing Axon Formation and Promoting Dendrite Growth. *Neuron* **71,** 433–446 (2011).

42. Yamashita, N. *et al.* Regulation of Spine Development by Semaphorin3A through Cyclin-Dependent Kinase 5 Phosphorylation of Collapsin Response Mediator Protein 1. *J. Neurosci.* **27,** (2007).

43. Korobova, F. & Svitkina, T. Molecular architecture of synaptic actin cytoskeleton in hippocampal neurons reveals a mechanism of dendritic spine morphogenesis. *Mol. Biol. Cell* **21,** 165–76 (2010).

44. Portera-Cailliau, C., Pan, D. T. & Yuste, R. Activity-regulated dynamic behavior of early dendritic protrusions: evidence for different types of dendritic filopodia. *J. Neurosci.* **23,** 7129–42 (2003).

45. Millet, L. J., Stewart, M. E., Sweedler, J. V, Nuzzo, R. G. & Gillette, M. U. Microfluidic devices for culturing primary mammalian neurons at low densities. *Lab Chip* **7,** 987–994 (2007).

46. Millet, L. J., Stewart, M. E., Nuzzo, R. G. & Gillette, M. U. Guiding neuron development with planar surface gradients of substrate cues deposited using microfluidic devices. *Lab Chip* **10,** 1525–1535 (2010).

Figures

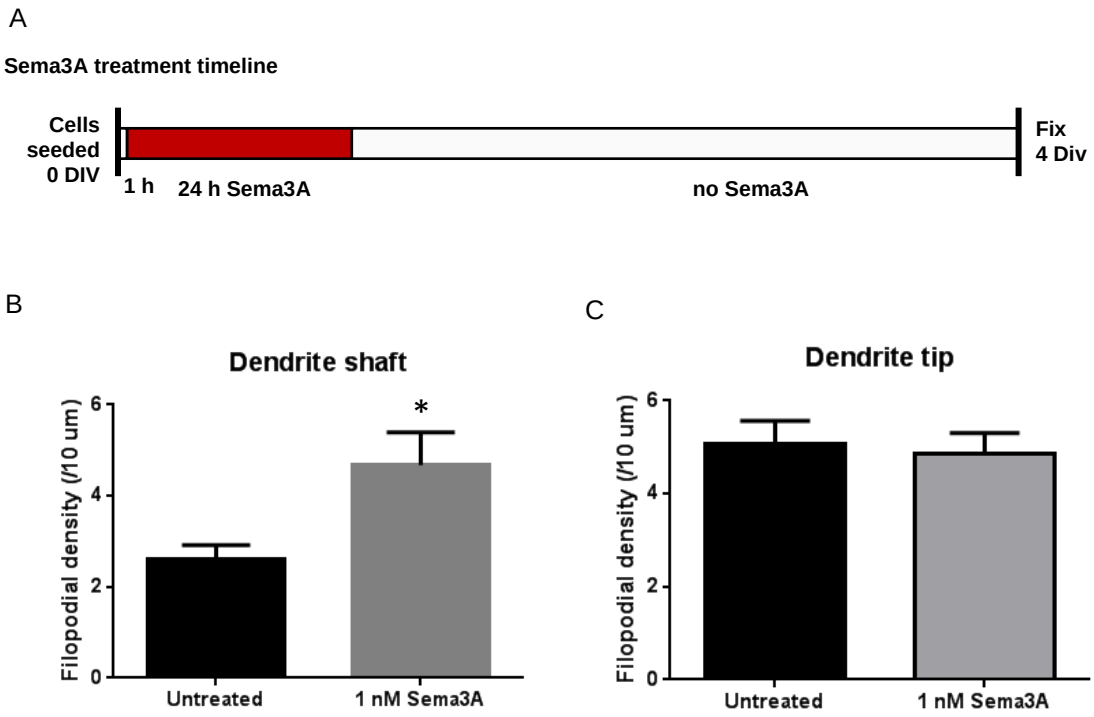

Figure 3.1. Sema3A treatment selectively increases filopodial density along dendritic shafts. (A) Treatment timeline for Sema3A. Sema3A was added to primary rat hippocampal neurons at 1 nM, 1 h after cell seeding, and it was rinsed out 24 h later. Neurons were fixed at 4 DIV, stained using DiA, imaged using a confocal microscope, and reconstructed using Imaris. (B) Neurites identified as dendrites through subsequent labeling with MAP2 (Microtubule Associated Protein – 2) were analyzed for filopodial numbers, and filopodial densities calculated as number of filopodia / 10 µm dendrite. A 24 h exposure to Sema3A at 1 DIV led to an increase in densities along shafts from 2.6 filopodia / 10 µm to 4.67 filopodia / 10 µm (Unpaired *t* test, n = 10, p = 0.0310), but did not significantly affect tip filopodial densities (C).

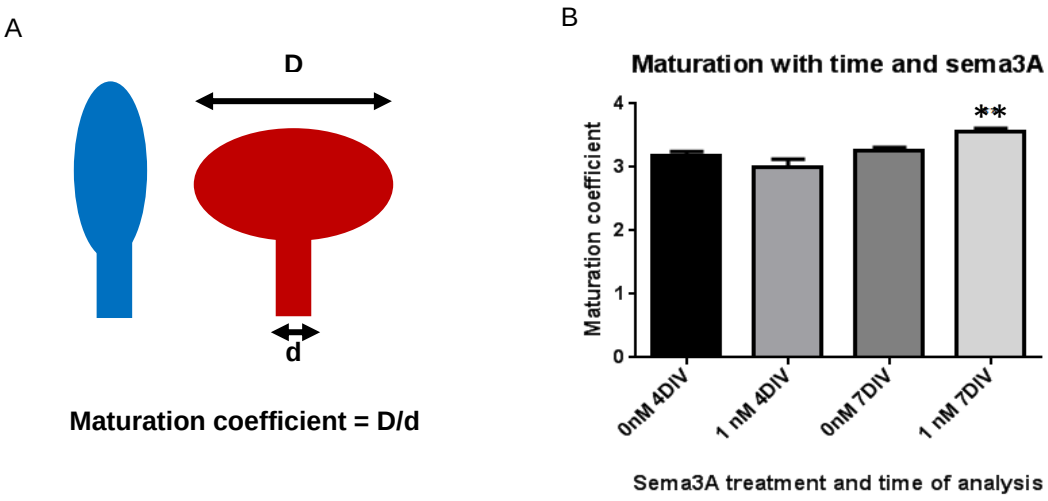

Figure 3.2. Sema3A promotes filopodial maturation to spines (A) Schematic showing filopodial maturation from rod-like immature filopodium (blue) to mature stub- or mushroom-shaped spine (red) with a bulbous head on a narrow neck. As spine morphology is characterized by a high spine head diameter, D, and a low neck diameter, d, a ratio of the two, D/d, is representative of level of maturation. (B) A 24 h long exposure to1 nM Sema3A at 1 DIV accelerated filopodial maturation to spines by the 7 DIV stage. Two-way ANOVA, n = 5, p = 0.0015

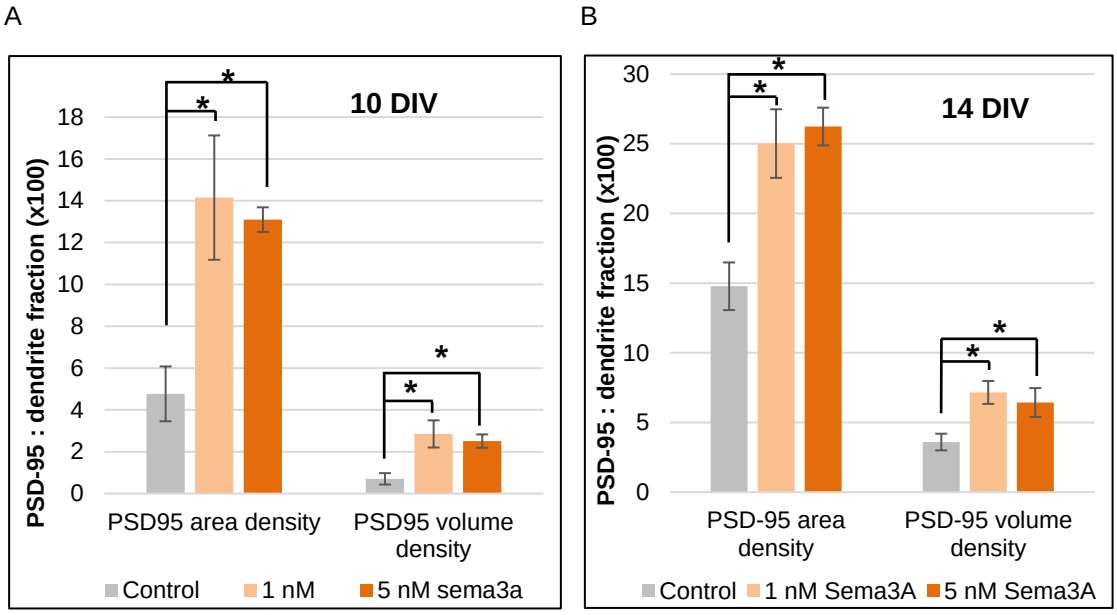

Figure 3.3. Sema3A promotes synaptogenesis. Z-stack images of primary hippocampal neurons at 10 and 14 DIV were reconstructed using Imaris. Areas and volumes of PSD-95 clusters and dendrites were quantified using PSD-95 and MAP2 antibody staining respectively. A 24 h treatment of Sema3A administered at 1 DIV led to a significant increase in both area and volume densities of synaptic clusters at (A) 10 DIV (One-way ANOVA, n = 16, p = 0.04 for area and volume) and at (B) 14 DIV (One-way ANOVA, n = 16, p = 0.005 for area and p = 0.03 for volume).

A

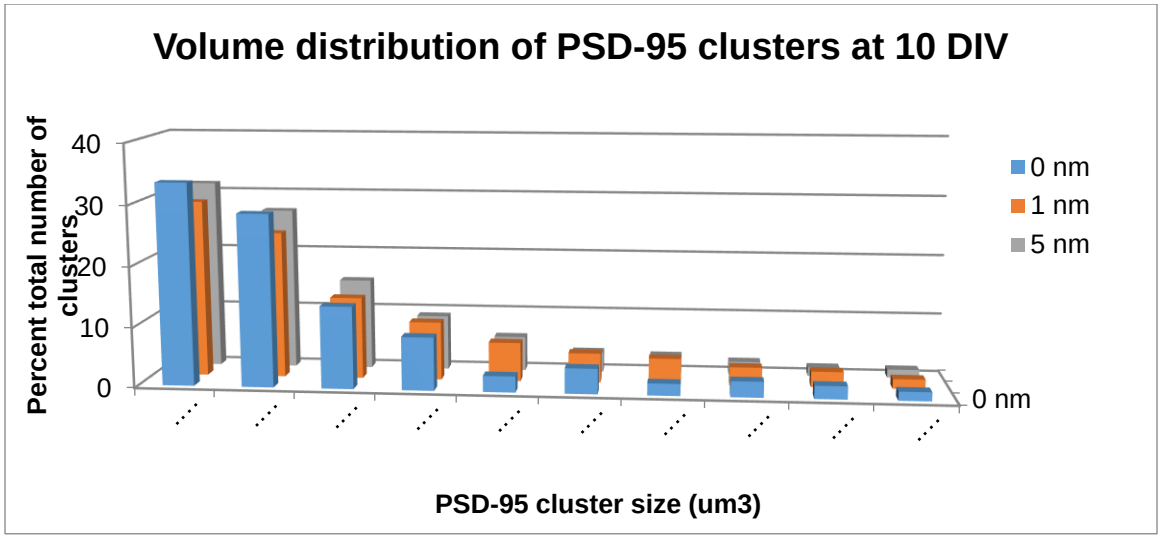

B

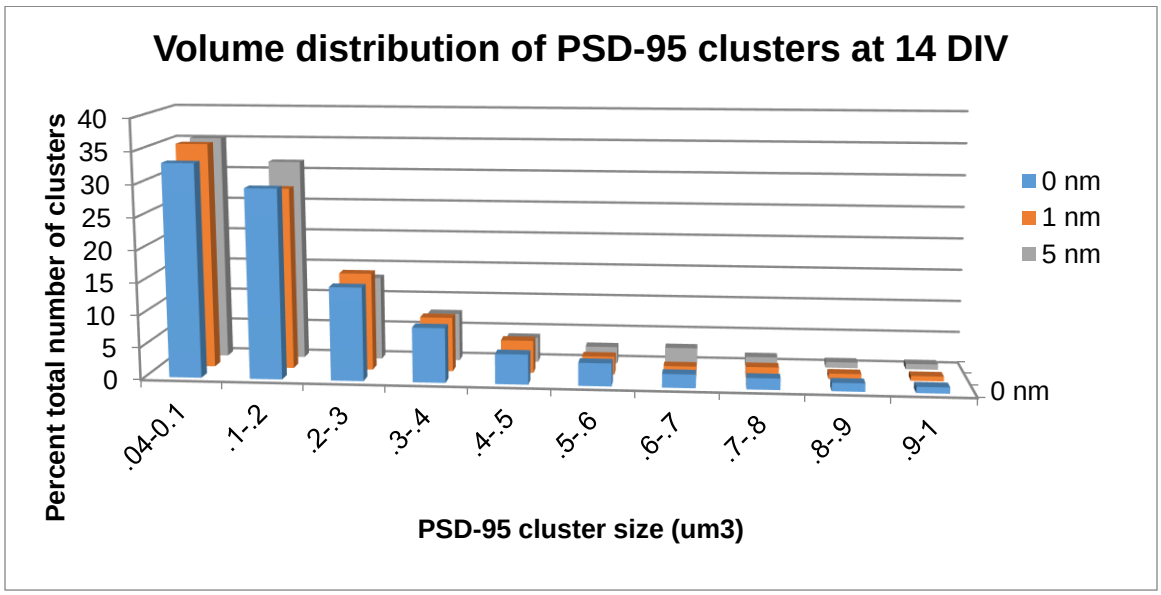

Figure 3.4. Sema3A administration does not vary volume distribution of PSD-95 clusters. Z-stack images of primary hippocampal neurons at 10 and 14 DIV reconstructed using Imaris were analyzed for PSD-95 cluster volumes. A 24 h treatment of Sema3A administered at 1 DIV, which led to increases in cluster area per unit dendrite area and cluster volume per unit dendrite volume, left the relative volume distribution unaffected. Similar percentages of clusters were seen in each volume division.

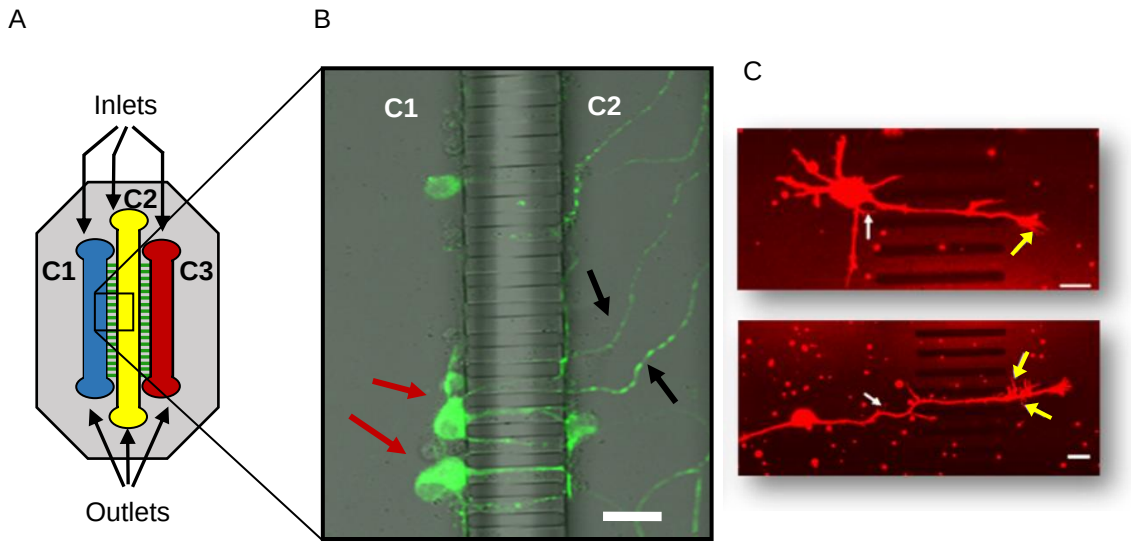

Figure 3.5. Filopodia form on both sides of an interconnect in compartmentalized channels of the microfluidic device. (A) Schematic of microfluidic device design. Channels C1, C2 and C3 are linked via 3 μm^2 x 45 µm interconnects. (B) Compartmentalized culture of rat hippocampal neurons, 4 DIV. Neurons in left channel (red arrows) send processes through inter-connects, into the right channel (black arrows). Scale bar = 20 µm. (C) Neurons at 2 DIV that have compartmentalized in microfluidic chambers labelled with membrane dye DiI. Neuronal process traverses interconnect and extends filopodia (white arrows) into 2 distinctly controllable, fluidically isolated channels. Scale bar = 10µm. Sema3A is introduced into C2 1 h after cell seeding, and rinsed out after 24 h. Only filopodia in C2 (yellow arrows) are exposed to Sema3A, while the rest of the neuron including the axon remain untreated.

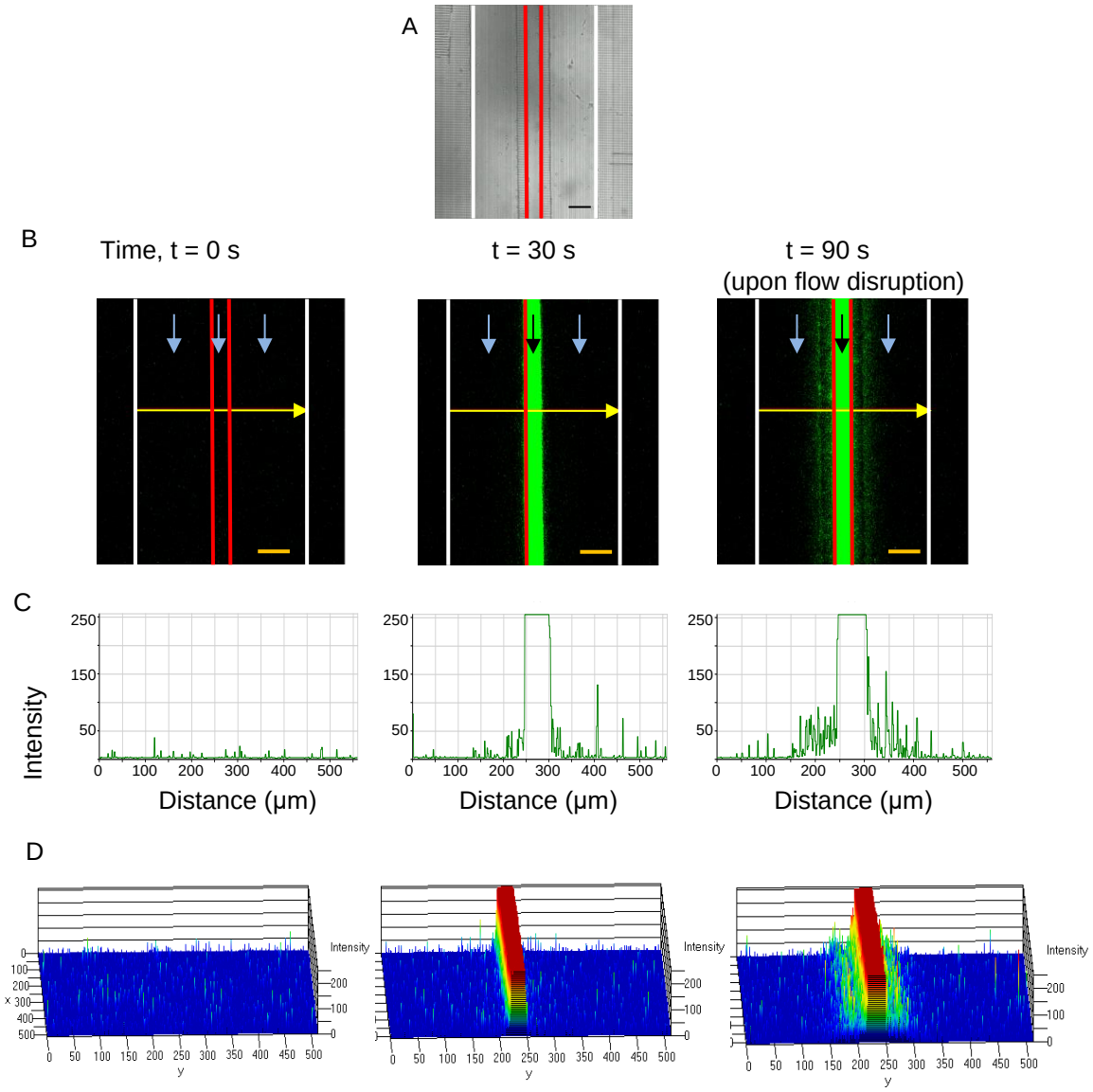

Figure 3.6. Fluidic isolation test using fluorescein isothiocyanate (FITC). (A) Bright-field image of the microfluidic device at time, t = 0 s. Red and white lines mark the outer edges of the central and side channels, respectively. Fluidic isolation was tested by flowing FITC through the central (B-D) or side channels (not shown). (B) Fluorescence time-lapse microscopy was used to visualize fluid flow. Blue arrows = PBS, black arrows = FITC. (C) Intensity profiles were generated along the yellow lines in (B). X-axis: distance, Y-axis: Intensity. (D) Intensity profiles in 2.5D. Intensity variation is depicted in rainbow spectrum with dark blue being the minimum intensity and red the maximum. Scale bars = 100 μm. At 90 s flow was disrupted by reversing the fluid head differential at the inlets and outlets with media levels higher for the central channel and lower for the side channels. This resulted in leakage of FITC from the central channel and this consequent leakage was observed as shown. This demonstrated the capability of the detection system to detect any disruption of fluidic isolation. In the absence of flow disruption, fluidic isolation was maintained (tested up to 12 h)

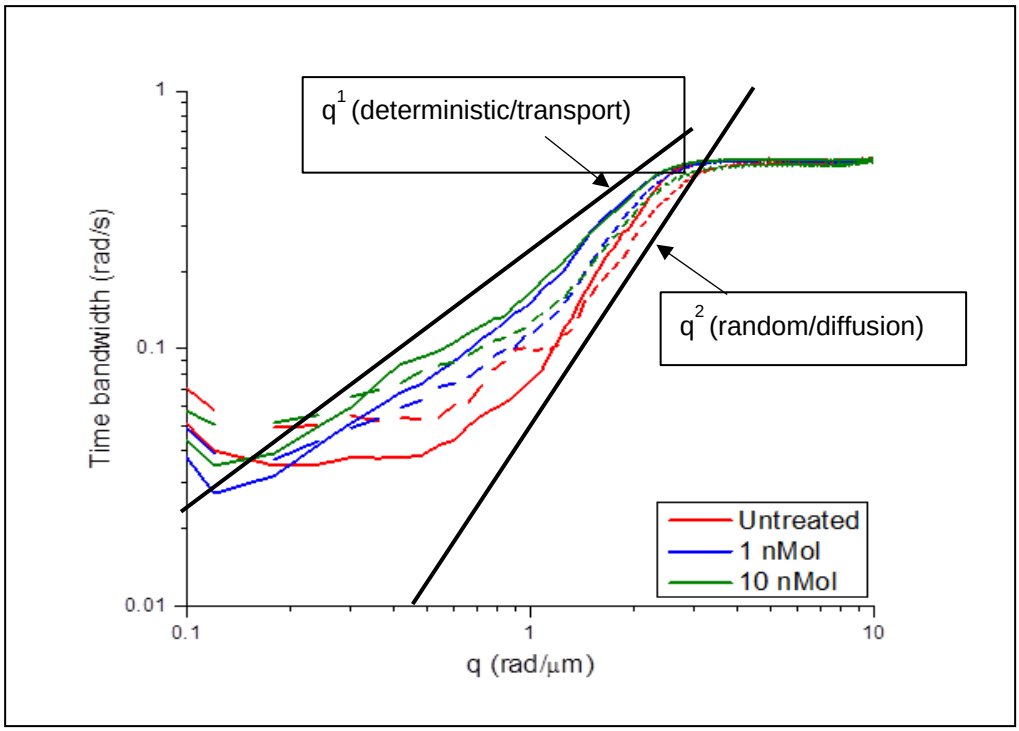

Figure 3.7. Dynamic analysis of filopodial movement Time lapse imaging of live neurons at 4 DIV using Spatial Light Interference Microscopy (SLIM) yielded quantifiable data that was analyzed using dispersion-relation phase spectroscopy (DPS) where q represents momentum transfer. Tip filopodia (solid lines) were compared to shaft filopodia (dashed lines) across three treatment regimens – control, 1 nM Sema3A and 10 nM Sema3A. The stronger the treatment, the faster the filopodial movement, both along the tips as well as the shafts. The highest increase was seen for tip filopodia, which also showed a more deterministic motion indicative of a 'search and grow' behavior.

A

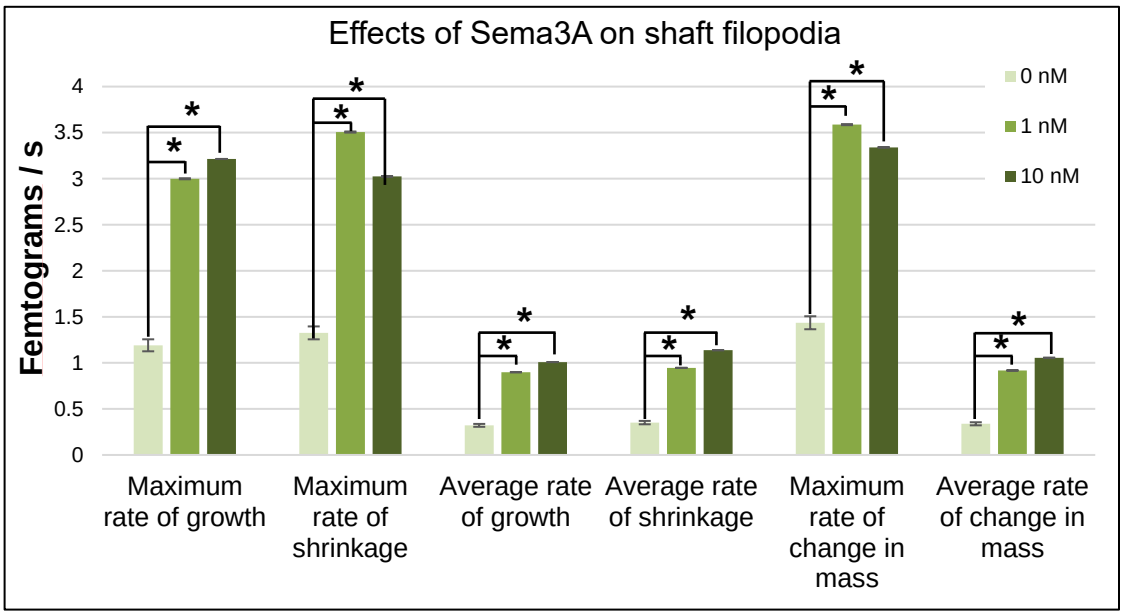

B

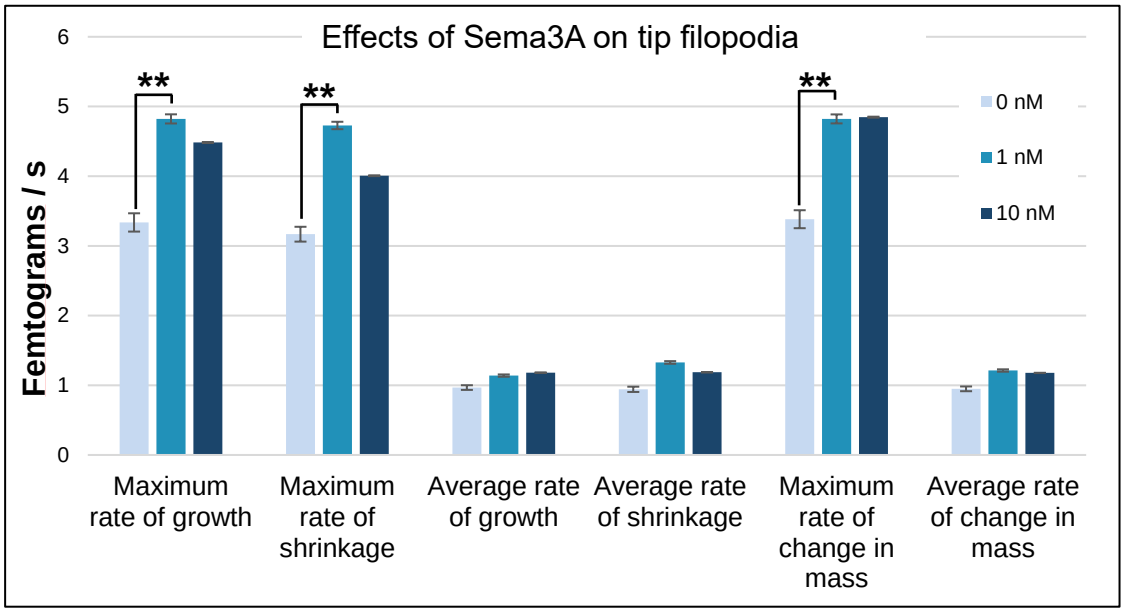

Figure 3.8. Sema3A increase motility in shaft filopodia selectively. Neurons treated with a 24 h dose of Sema3A at 1DIV and control cells were imaged using SLIM at 7 DIV. Phase analyses of regions of interest containing single filopodia were used to quantify the motility of tip and shaft filopodia for treated and untreated cells. (A) Cells treated with 1 nM or 10 nM Sema3A showed higher values of maximum and average extension and retraction rates and motility (change in mass/unit time) for shaft filopodia. (One-way ANOVA, $n = 12$, $p < 0.05$). (B) Sema3A had no significant effects on the dynamics of tip filopodia except for an increase in the maximum rates of growth, shrinkage and overall mass change. (One-way ANOVA, $n = 12$, $p < 0.05$).

CHAPTER 4: MICRODEVICES ENABLE FOCAL STIMULATION OF CELLULAR NETWORKS

Abstract

Key determinants in the emergence of complex cellular morphologies and functions are cues in the micro-environment. Primary among these is the presence of neighboring cells as networks form. Therefore, for high-resolution analysis, it is crucial to develop micro-environments that permit exquisite control of network formation. This is especially true in neuroscience, tissue engineering, and clinical biology. We introduce a new approach for assembling polydimethylsiloxane (PDMS)-based microfluidic environments that enhance formation and analysis of functional cell networks. We report that in solvent-extracted PDMS (E-PDMS) unique properties emerge with the removal of free oligomers, and demonstrate that high-strength bonding occurs upon autoclaving this oligomer-free E-PDMS onto clean glass – properties not associated with conventional PDMS. Sequential chemical extraction followed by autoclave annealing promotes polymer cross-linking, facilitates covalent bond formation with glass, and retains the highest biocompatibility. This extraction protocol also shortens the oligomer removal

---

This work is currently under review for publication -

Millet, L. J., Jain, A. & Gillette M. U. Less is More: Oligomer extraction and thermal hydration increase PDMS bonding forces for a new method of microfluidics assembly. *Lab Chip* (under review)

Support was provided by the National Science Foundation IGERT 0965918 (AJ), STC CBET 0939511 (MUG), CBET 1040462 (MUG) and EAGER DBI 1450962 (MUG) and National Institute of Health R21MH101655 (MUG). ORNL is managed by UT Battelle, LLC, for the Department of Energy under contract DE-AC05-00OR22725. L. Millet and A. Jain contributed equally to this work.

process from 5 to 2 days. Resulting microfluidic platforms are uniquely suited for cell-network studies owing to high bond strengths, effective corralling of cellular extensions, and elimination of harmful oligomers associated with conventional PDMS. We demonstrate simple, effective, simultaneous actuation of multiple microfluidic domains for invoking ATP- and glutamate-induced Ca^{2+} signaling in glial-cell networks. These low-cost, simple E-PDMS modifications and flow manipulations further enable microfluidic technologies for cell-signaling and network studies as well as novel applications.

Introduction

We present a new method for adhering highly biocompatible E-PDMS microfluidic channels to glass substrates that achieves high bond strength without compromising E-PDMS biocompatibility. Microfluidic devices are a mainstay for on-chip miniaturization of chemical and biological systems owing to the highly controlled spatiotemporal manipulations of minute sample volumes. Microfluidics are particularly beneficial for resolving mechanisms of growth, differentiation, and signaling of biological systems that are complex and dynamic. Such microtechnology confers the ability to perform complex environmental manipulations that mimic natural systems on a fundamental level.[1,2] From manipulations of subcellular domains to miniaturized organs-on-chip, microfluidics facilitate systematic interrogations of cells and networks through the establishment of functional microenvironments.[1,3–8]

The selection and utilization of materials and chemicals are also key factors for defining the cellular microenvironment. Over the past century, the means of culturing

cells of the nervous system have improved in parallel with the development of a range of platforms and media formulations for chemically-defined investigations into mechanisms of nervous system development and function.[2] Recent improvements in microfabrication, materials, engineering, and chemical processes have provided organs-on-chip that refine the ability to achieve biological discoveries and advance medical diagnostics.[3,9–12]

Because of the many advantages inherent in PDMS (transparency, affordability, gas permeability, replication, etc.)[13,14], it is widely accepted as an ideal material for rapidly fabricating microfluidic devices and environmental culture systems. Thus, it is the most widely used polymer for microfluidic prototyping in research labs and is generally considered to be biocompatible. However, the biological implications of PDMS are process-dependent with conditional biocompatibility that scales with device dimensions and possesses fluidic constraints.[15–18]

Our previous work demonstrates that PDMS can be rendered highly biocompatible by extracting the unpolymerized oligomers and metal catalysts from the cured elastomer to produce E-PDMS.[11] Not only does the solvent extraction process improve the material biocompatibility, but it also alters material properties of PDMS. E-PDMS exhibits reduced adhesion of conformal contact to planar surfaces (e.g., glass coverslips, microscope slides, and Petri dishes)[19] and increased absorption of small molecules.[20] While reduced conformal adhesion of E-PDMS confers benefits for substrate patterning and minimizes the transfer of hydrophobic oligomers to the substrate,[19] E-PDMS provides unique fabrication challenges for implementing microfluidic platforms for cell signaling studies of adherent cells.

Typical approaches used to covalently bond PDMS to glass substrates include high-energy processes (plasma exposure, corona discharge, UV-ozone exposure)[21–24] that have the potential to break bonds and promote the generation of more oligomers. The biological implications of oligomer regeneration in E-PDMS are not well understood. The presence of oligomers in conventional PDMS microfluidic devices has been shown to influence gene expression; in ethanol-washed PDMS, oligomers accumulate within cells cultured in the microfluidic channel.[15,16] Improving highly biocompatible E-PDMS adhesion through non-destructive, bio-compliant processes provides favorable conditions for cell signaling studies in microfluidics and minimizes material-mediated confounds to biological investigations.

By performing solvent-extraction prior to autoclaving, E-PDMS becomes covalently bound to glass substrates. This process also retains the high biocompatibility of PDMS while sterilizing the materials. Autoclaving is a high temperature, high pressure, humidified process that is known to drive the polymerization process towards completion; autoclave sterilizers are available in most biological facilities.

The high-strength covalent bonds of E-PDMS permit a tight interface for microfluidic manipulations without detaching the channels from the surface; without tight E-PDMS-to-glass bonds, the devices are prone to delamination during cellular growth and migration. Combining the high biocompatibility of E-PDMS with the versatility of covalently-bound channels improves conditions for cell signaling studies in microfluidic environments. After rigorous solvent extraction, unpolymerized oligomers are no longer available to translocate into cells where they can confound cell signaling processes.

Glial cells are the most abundant type of cell in the brain and play important roles in modulating neuronal communications. Astrocytic glia sense and respond to local signals, in part through extended branches that contact neighboring glia, neurons, and endothelial cells. Conventional cultures in plates, dishes, or wells do not offer the ability to perform spatio-temporal interrogation without exposing the population of interest to the stimulant through diffusion. Through microfluidic platforms, signaling between distinct cellular populations can be studied without exposing the entire population to the stimulant. Furthermore, multiple spatial stimulations can be deployed for more complex signaling studies, an experimental advantage not achievable without microfluidics. Here we compartmentalize branches of primary glial cells in E-PDMS microfluidic platforms and interrogate glial activity by monitoring Ca^{2+} oscillations in response to focal pulses of neurotransmitters applied through laminar flow. Ca^{2+} oscillations are observed in individual cells and waves of Ca^{2+} transients are observed in glial networks. Our work demonstrates the advantage of implementing E-PDMS microfluidic platforms for cell signaling applications.

Materials and methods

Preparation of PDMS Plugs

PDMS plugs were prepared by mixing pre-polymer and curing compound (Sylgard 184, Dow Corning) at a 10:1 ratio, respectively. After thorough mixing, all wells of a clean 96-well plate were filled with the PDMS mixture and cured at 70 ^{o}C for at least 2 h. Care was taken to prevent filling voids between wells with PDMS. A small amount of 70% ethanol in deionized water (DI, from a Millipore (MilliQ) filtration

system) was used to facilitate releasing cured PDMS plugs from individual wells. PDMS plugs were dried of ethanol, then a 1.0 mm dermal biopsy punch was used to bore a diametric hole through the vertical midpoint of the plug. PDMS plugs were separated into two groups for treatment (solvent extraction) and control group (no treatment) prior to assembling plugs onto microscope slides or PDMS slabs.

Preparation of Microfluidic Channels

Microfluidic channels were replicated using the same master sets from our previous work for substrate patterning; for master fabrication and PDMS microchannel replication from a library of devices, we refer the reader to our previous publication.[19] The PDMS microfluidic channel replicates were solvent extracted through a simplified protocol (protocol defined below) followed by a thermal bonding process using an autoclave.

PDMS Extraction

Prior to assembling PDMS plugs or channels onto slides or coverslips, E-PDMS structures were extracted through a series of organic solvents according to the optimized extraction protocol[19] modified from our original process[18], while the control group was left untreated. For microfluidic channels, four to five PDMS microchannel replicates measuring ~464 mm^2 and 2–4 mm thick were gently stirred and submerged in 150–200 mL of each solvent for the indicated times: HPLC grade pentane (Fisher Scientific) for ~16 h; xylenes, isomers with ethylbenzene, 98.5+% (Sigma) for 1–2 h; xylenes, isomers with ethylbenzene, 98.5+% for 2–4 h; 200 proof ethanol USP for 1–2 h (AAPER);

ethanol for 2 h minimum. In the final step, the PDMS channels were transferred from ethanol to 1 L of sterile DI water and soaked overnight, then dried prior to use. For E-PDMS plugs, the same solvent extraction sequence was employed using 500-600 mL of each solvent. To ensure the PDMS plugs were devoid of any residual solvents, plugs were dried for at least 1 week (ambient temperature and pressure) after the extraction process, prior to use.

Glass Cleaning

Two common methods of glass cleaning were employed for comparison, ethanol cleaning and acid-bath cleaning. Ethanol-cleaned microscope slides for PDMS adhesion studies were submerged and spaced apart (not stacked) in a beaker of 200 proof ethanol for at least one day. After soaking, the glass slides were removed and placed on end on absorbent paper to remove excess ethanol and allowed to dry. Acid-cleaned microscope slides were prepared by immersing the glass slides in concentrated sulfuric acid (> 90% w/w) overnight, minimum. For convenience, the slides were kept in a histology rack during acid bath cleaning. Note of caution: Concentrated sulfuric acid is caustic and hygroscopic; leave ample empty vessel volume for fluid expansion. After a minimum of 24 h in sulfuric acid, the histology rack with slides was removed and rinsed with a direct stream of MilliQ DI for 5 min. Clean glass slides were turned on end and dried. For cell culture, acid-cleaned coverslips (Corning, thickness no. 1.5) were prepared following this same cleaning protocol.

Elastomer Bonding

Immediately after clean glass slides and coverslips were dry, unextracted and E-PDMS plugs, or microchannels, were placed in conformal contact with the glass substrate for thermal bonding using an autoclave. In a comparative study, ultra-violet light (UV) or a dry oven were used for bonding PDMS to glass substrates; high-powered UV with continuous air flow was used to oxidize/activate the PDMS for bonding followed by a 70 ^{o}C annealing process. The PDMS glass assemblies were placed in an aluminum foil-lined metal pan, covered and sealed with aluminum foil, and autoclaved with the following settings: 121 ^{o}C and 110 kPa for 20 min (sterilization step) with a 20-min drying time (81 ^{o}C to 91 ^{o}C).[18] After thermal bonding, E-PDMS microfluidic channels for cell culture were cooled, removed from foil in a sterile biosafety hood, transferred to a culture dish and prepared for cell culture.

Performing Force Measurements

Force measurements of adherent unextracted and E-PDMS structures on glass or PDMS substrates were taken at room temperature after autoclaved samples cool to room temperature (≥ 30 min). Spring force meters (SI Manufacturing) were used for measuring the force required to separate PDMS plugs from substrates. Meter ranges were in Newtons (N) 0-2.5 N, 0-5 N and 0-30 N. Force meters were connected to the PDMS plugs using a strong wire triangle. The triangle base passed through the PDMS plug with the apex attached to the hook of the force meter (Figure 4.1B). Force meter performance was verified with calibrated weight standards.

Flow Control and Manipulation

Dynamic fluid manipulations were achieved by modulating positive and negative pressures at the fluidic ports and reservoirs. Culture perfusion was created with differential hydrostatic pressures and gravity flow. For hydrostatic pressures, fluid droplets were placed at the inlet ports or reservoirs to create positive pressures with surface tension. After surface tensions equilibrated, the dish was tilted a few degrees to elevate one end of the coverslip and reinitiate flow. Negative pressures were obtained with unequal concave menisci at the inlets or reservoir. For pulses of stimuli, rapid fluidic infusion was achieved by combining positive pressures (droplets at inlets) with negative pressures (concave menisci at the outlet reservoir), and the infusate was rapidly reversed by wicking the inlet(s) empty with a Kimtech wipe. Reinitiation of flow was achieved by pipetting defined volumes back into the empty inlet. Imaging controls (with flow of fluorescein and fluorescently labeled antibodies) were performed to refine the pulse process. During glial stimulation, the glial culture channel was always maintained at a greater positive pressure than stimulation channels to prevent stimuli from entering the glial culture compartments. Fluidic manipulations were greatly assisted by monitoring experimental duration during image acquisition and utilizing time-mark features in the Zeiss image acquisition software.

Glial Cell Culture

Animal procedures were conducted in accordance with PHS Policy on Humane Care and Use of Laboratory Animals under approved protocols established through the University of Illinois at Urbana-Champaign Institutional Animal Care and Use

Committee. Astrocytes were isolated from P2-P4 Long-Evans BluGill rats through the following procedure: Subjects were rapidly decapitated, the brain removed, meninges cleared from tissues, and the hippocampi and cortex dissected. For each culture, the tissue was minced and incubated with papain (25.5 U/mL, Worthington) or trypsin EDTA (0.05%) for 30 min at 37 ºC. After enzymatic digestion, tissue fragments were rinsed with media (without enzyme), and the tissue triturated through a fire-polished glass Pasteur pipette. The cell suspension was centrifuged at 1400 rpm for 5 min and suspended in astrocyte culture media (DMEM with 10% FBS, 3mM L-glutamine, and 100 U/mL penicillin and 0.1mg mL^{-1} streptomycin) and plated at 300-500 cells/mm^2. Cultures were maintained in astrocyte culture media in a humidified incubator with 5% CO_2 and 95% air until reaching confluence (~7-9 days). Cultures were shaken at ~300 rpm for four consecutive periods of 18 h to remove loosely adherent cells (i.e., neurons and microglia); each 18-h interval was interrupted by ~30-h periods of overnight recovery.[25,26] Astrocytes were released from the dish and loaded into microfluidic channels where they were allowed to grow and extend branches to compartmentalize into adjacent channels.

Calcium Imaging

Imaging spatial dynamics of transient Ca^{2+} signals of individual glial cells and networks was achieved using Fluo-4 AM, a cell-permeable Ca^{2+} indicator dye. Cultures were mounted on a Zeiss LSM-510 Meta NLO laser-scanning microscope without an environmental chamber and imaged at room temperature (22-25 ºC). Glial cell Ca^{2+} transients were evoked with ATP (20 µM) or glutamate (10 µM). Fluorescence signals

were obtained using argon laser illumination (488 nm, 0.1%) through a plan-apochromatic 20x (0.8) objective, and a LP505 filter. Images were acquired with a photomultiplier tube; detector and scanner parameters (gain, sensitivity, scan rate, zoom and field size) were optimized to minimize laser exposure to live cells, and maximize scan rates for field size and resolution.

Immunocytochemistry

Immunochemistry was performed following our previously published process.[18] Glial cultures were fixed for 30 min with 4% paraformaldehyde and then permeabilized for 10 min with 0.25% Triton in PBS and blocked for 30 min with 10% BSA in PBS at room temperature. To label glial cells, mouse monoclonal primary antibodies against glial fibrillary acidic protein (GFAP, 1:1000 dilution) were used; antibody-labeling occurred for 1-2 h at room temperature or overnight at 4 ^{o}C. Secondary antibodies were goat-anti-mouse Alexa 488 (1:1000 dilution, Molecular Probes) incubated at room temperature for 1–2 h. Rhodamine-conjugated phalloidin (5 U/ml, Molecular Probes) was used to label actin filaments (f-actin) with 20 min incubation at room temperature. The same protocol was followed for immunochemistry in microfluidic channels with flow maintained throughout the labeling process and flow velocities kept to a minimum. Flow directions were reversed every 10 min during the course of the antibody and phalloidin incubations. Following ~20 min PBS rinse, the samples were briefly rinsed with DI water and dried. Channels were filled with Prolong Gold anti-fade reagent (Molecular Probes). To optimize imaging, cells in channels were imaged immediately following antifade reagent application.

Results and discussion

Material characterization

E-PDMS exhibits unique material properties distinct from untreated PDMS. Prior work has demonstrated the high biocompatibility of E-PDMS for establishing cultures of highly sensitive cells, neurons.[18] While E-PDMS is highly biocompatible for small-volume cell cultures, the removal of oligomeric components weakens the conformal contact and the ability of E-PDMS to remain attached to a glass substrate. E-PDMS microfluidic platforms detach from substrate surfaces more readily than unextracted PDMS. While weak E-PDMS contact is advantageous for microfluidic patterning processes,[19] it can be cumbersome for cell cultures utilizing dynamic flow regimes administered through pumps and valves.

During experiments with neuronal cultures using E-PDMS, we occasionally observed neurites probing under the E-PDMS to navigate out of the channel between the PDMS and glass, indicating an imperfect seal. When maintaining long-term cultures (> 10 days) of primary neurons in E-PDMS microfluidics, we also observed that distinct changes occur in the conformal contact adhesion forces of E-PDMS. Some E-PDMS channels in long-term cultures exhibited high affinity for the glass and could not easily be removed. Thus, E-PDMS channels in culture either delaminated from the coverslip or they became increasingly adherent the longer they were maintained in the cell culture environment (a humidified atmosphere at 37 ^{o}C).

We hypothesized that longer exposure to elevated temperatures and/or humidity facilitates the formation of adhesion bonds between E-PDMS and a clean glass substrate. To test this hypothesis, we fabricated PDMS plugs of uniform volume and geometry and

subjected them to various annealing processes on clean glass slides following solvent extraction (Figure 4.1). We then measured the force required to remove each plug from the glass surface. The processes of solvent extraction, or autoclaving, alone improves PDMS biocompatibility and renders the microfluidic environment sterile,[18] but the combined effects of these processes on adhesion have not been characterized.

Figure 4.2 shows a time-dependent increase in forces required to separate E-PDMS plugs from glass slides exposed to a range of conditions. For cell culture conditions (Figure 4.2A), there is a significant increase in the adhesion bonds (from 2.0 to 8.8 Newtons (N), ($p < 0.02$, two-way ANOVA) of E-PDMS on acid-cleaned glass when exposed for 2 weeks to a humid atmosphere at physiological temperatures (37 ^{o}C). The data are in agreement with prior observations that elevated temperatures and/or humidity facilitate E-PDMS bonding to clean glass.[18] Our glass cleaning process for primary cell culture uses a sulfuric acid bath followed by a DI water wash. A common alternative cleaning protocol is sterilization with ≥ 70% ethanol in DI water. We included both glass preparations in our E-PDMS and PDMS adhesion force comparisons. Our results show that under cell culture conditions, acid-cleaned glass enables a stronger adhesion of E-PDMS to glass than does the ethanol-cleaned glass.

To resolve the contributions of conventional fabrication and sterilization conditions to increased E-PDMS bonding forces, we compared E-PDMS annealed to glass with dry heat (PDMS curing oven, 70 ^{o}C) vs. humidified heat (autoclave sterilization, 121 ^{o}C). Figure 4.2B shows that autoclaving increases adhesion of E-PDMS and PDMS over dry heat exposure for both material types ($p < 0.05$, two-way ANOVA). E-PDMS showed superior adhesion over PDMS under either treatment. After 4 days'

exposure of E-PDMS and PDMS to dry heat, PDMS adhesion results were not statistically different from 2 h, whereas E-PDMS on acid-cleaned glass over 4 days showed a statistically significant increase (from 2.0 N to 6.7 N, $p < 0.001$, two-way ANOVA); the increase on ethanol-cleaned glass at 4 days was not significant.

We performed an extended time-course study on the temporal-dependence of E-PDMS annealing under dry heat (Figure 4.2C). The data show that after 7 days at 70 ^{o}C E-PDMS removal forces (4.7 to 10.7 N) are significantly greater on acid-cleaned glass than the alternative ($p = 0.0002$), and forces become similar to those achieved through the 2-h autoclaving process (2.0-10.7 N) (Figure 4.2B). These data suggest that increased heat promotes the annealing process of E-PDMS to glass. E-PDMS plugs kept at room temperature (25 ^{o}C) for 14 days did not show this large an increase in adhesion forces but at 14 days had significantly stronger (2.7 N verses 4.5 N, $p < 0.0001$, two-way ANOVA) bonding than PDMS (Figure 4.2D). To further understand the influence of temperature and humidity, we exposed both E-PDMS and PDMS plugs to temperature-matched (135 ^{o}C) treatments in a dry oven and in an autoclave with saturated humidity (Figure 4.2E). Autoclaving produced significantly stronger forces than dry heat for E-PDMS on acid-cleaned glass ($p = 0.014$) and ethanol-cleaned glass ($p = 0.0004$). Again, autoclaving provides superior results for E-PDMS, suggesting that both humidity and elevated temperatures facilitate the annealing process of E-PDMS to glass.

For perspective, we compared our E-PDMS annealing process to the typical oxygen plasma-bonding process. E-PDMS material can be activated through high energy processes; however, these high energy processes break PDMS bonds and introduce more oligomers into the culture system.[21,22,24] Our results show that E-PDMS adhesion

outperforms PDMS after autoclaving or plasma treatment, and plasma treatment shows superior removal forces compared to autoclaving (Figure 4.2F). It remains uncertain how much oligomers are generated in E-PDMS through high energy processes, such as plasma treatment, or how freely any newly formed E-PDMS oligomers can translocate from the material to cells cultured in microfluidic systems. Given these adhesion study results, we employed solvent extraction followed by autoclave annealing for microfluidic cell cultures with fluid manipulation for cell signaling studies.

With the ability to covalently bond E-PDMS to glass through an autoclaving process, we tested the possibility of performing polymer-to-polymer bonding through extraction and autoclave annealing. We placed E-PDMS and PDMS materials each in direct contact on both substrates of E-PDMS and PDMS, then subjected them to the same autoclaving process. Following the annealing process, we observed a consistent trend of noticeable location-dependent deformation of the plug "footprint" when plugs were placed on the opposite substrates and autoclaved. Profilometric measures of PDMS substrates show that PDMS indents (~7 μm) where E-PDMS plugs are placed in direct contact during autoclaving (Figure 4.3). Conversely, the footprint of E-PDMS swells (~6 μm vertical change) only where the PDMS plugs are in contact with the E-PDMS substrates (Figure 4.3B). The footprint deformation induced by autoclaving E-PDMS in contact with PDMS is significant ($p < 0.0001$) and consistent regardless of whether E-PDMS serves as the plug or substrate (Figure 4.3C). No appreciable changes of footprint deformation are observed when E-PDMS and PDMS plugs are matched to the selfsame substrates.

Oligomer translocation is possible in cross-linked PDMS as evidenced by the time-dependent reversion of plasma treated PDMS from a hydrophilic to hydrophobic state.[21,22] This information, combined with our results of E-PDMS and PDMS deformation, suggest that oligomer translocation occurs within PDMS, and the effect on the material is measurable after translocation from source (PDMS) to sink (E-PDMS). The observable deformation indicates that a pronounced quantity of material remains unpolymerized when prepared under common conditions (10:1 ratio, 70 ^{o}C cure for 2 h). It also provides further evidence to support the need to remove unpolymerized oligomers through the pentane-xylene-ethanol-water solvent extraction process.

Bonding force measurements show that PDMS-PDMS pairing achieves the highest bonding forces (1.18 N) between any two polymer types (Figure 4.3D), possibly due to the presence of oligomers and the platinum catalyst that can facilitate further chemical interactions between untreated PDMS materials at elevated temperatures. Without oligomers and catalyst in one of the two paired materials, bonding forces are on average half (0.39-0.78 N) those achieved with PDMS-PDMS interfaces. Solvent extraction removes oligomers and platinum catalyst from the polymerized material,[18] thus reducing its ability to crosslink with other PDMS surfaces but improving the ability of E-PDMS to bind to glass. These results contribute to the understanding that E-PDMS possesses unique material properties, beyond increased biocompatibility, apart from its native, unextracted material form.

Cell signaling

With the ability to produce highly-biocompatible E-PDMS tightly bound to clean glass substrates, we cultured primary astrocytes in E-PDMS microfluidic platforms for cell observation and analyses. These platforms enable spatiotemporal manipulation of fluids to achieve multiple, simultaneous or sequential focal stimulations across compartmentalized cultures. Following solvent extraction, E-PDMS microfluidics were trimmed to produce fluid source wells useful for retaining and perfusing media during cell culture, for actuating fluids during cell signaling studies, and for immunolabeling cells (Figure 4.4). Fluidic pulses, achieved through a combination of gravity and hydrostatic pressure, were produced in adjacent channels of the microfluidics to demonstrate a range of fluidic controls from seconds to minutes (Figure 4.5). The method of chemo-temporal manipulation employed enables rapid chemical transients without increased pressures within the microfluidic device. This approach to fluidic actuation permits simultaneous pulses in multiple channels and is applicable for any lab seeking to employ microfluidics, and the approach does not require expensive pumping systems.

Like neurons, glial cells can be guided into adjacent microchannel compartments. Individual glial cells cultured in E-PDMS microfluidics develop glial extensions that migrate along channel corners to extend through 3 μm interconnects. Most glia show affinity for the glass-to-sidewall channels interface. Larger ramified glial cells do not prefer channel corners (Figure 4.6) but appear to avoid them. Similar observations of corner affinity, or avoidance, have been noted for neurons in microfluidics.[18,27]

Glial protrusions possess sensory capabilities for detecting changes in extracellular concentrations of small signaling molecules (e.g., ATP, glutamate). Glial

cells exhibit spontaneous or evoked fluctuations of internal Ca^{2+} stores that can induce propagating signals that pass through nervous tissues and cell cultures.[28,29] Potential roles of Ca^{2+} waves include contributions to vascular regulation, metabolic processes, synaptic modulation and mechanisms of axonal guidance.[30–32] Ca^{2+} transients in glial cells exhibit characteristic temporal signature forms and periodicities.[33–36]

Figure 4.7 shows a population of glial cells stimulated through a subcellular plug of ATP (10 μM) focally administered to a compartmentalized cell. Within the population, some glial cells show brief, robust cyclic or acyclic response, while other cells continue to oscillate beyond the 4 m observation time. Previous studies have typified Ca^{2+} responses with high throughput analyses; signals of glia in E-PDMS microfluidics conform to categorical morphologies of spikes, bursts, cyclic responses, or sustained Ca^{2+} elevations.[33] The rate of Ca^{2+} wave propagation (11-12 μm/s) for glia cultured in our E-PDMS microfluidic samples are within the range of wave propagations observed in dispersed cultures and brain slices (6-27 μm/s).[37] The process of extracting unpolymerized oligomers and binding E-PDMS to the glass through autoclaving both removes harmful oligomers that can accumulate in cells,[15,18] and provides strong adhesion forces that allow for cell signaling studies without E-PDMS delamination.

With the ability to develop and stimulate compartmentalized glial cultures without biasing the remaining culture to stimulating chemical cues, we cultured glial populations in the central channel between two parallel microfluidic stimulation channels. Glial cells develop in the central channel and expand in clusters to extend processes into adjacent channels throughout the length of the microfluidic platform. ATP (20 μM) was administered before glutamate (50 μM) in succession (73 s between applications) (Figure

4.8). Although two inputs were applied, three population responses were observed (Figure 4.8A-B). First, ATP created a local response on one side of the population. A second stimulation locally activated the opposite portion of the population, followed by a third robust response on the same side as the second response. The third stimulation induced activation of the entire population, reminiscent of a microburst (Figure 4.8B). While the source of the additional Ca^{2+} response is not known, the most plausible explanation would be that the ATP plug activated an upstream glial population, glial processes extending into the second stimulation channel may have released a chemical messenger into the channel prior to the introduction of the glutamate application. Through laminar flow, the chemical messenger could be carried down the channel to activate downstream glial populations. Figure 4.8C schematic summarizes the sequence of cellular "regions of interest" activated and displayed in Figure 4.8B.

Glial cells are known to signal both through gap junctions and vesicular release.[30,38] Gap junctions permit local signal transfer to directly connected cells whereas gliotransmitter release can influence cells not connected through gap junctions.[39] We demonstrate the ability to culture glial cells in E-PDMS microfluidic devices for cell signaling investigations. A handful of papers co-culture glial cells with neurons in microfluidics for studying neuro-glial interactions;[40–45] to our knowledge, no investigations specifically study glial population signaling interactions in microfluidics.

Microfluidics surpass cell culture dishes in the ability to exhibit spatio-temporal control of the microenvironment. Glial cells stimulated in a dish can release gliotransmitters that diffuse from sites of stimulation to neighboring cells. Culture dish perfusion chambers allow for continuous fluidic exchange that can rapidly wash stimuli

away; however, the entire culture is exposed to flow conditions that carry the stimuli across the remaining population or remove locally released neurochemicals. Microfluidics remove many of the limitations and enable a broader range of signaling studies not achievable through dish cultures, perfusion chambers, or *in vivo.*

Conclusion

This work advances the fabrication and implementation of microfluidics, particularly for biological applications and cell signaling studies. With conventional equipment (autoclave and solvent hood) available in biological departments, elevated humidity and temperature can be used to induce high-strength bonds between E-PDMS and glass to permit highly biocompatible microfluidics for maintaining fluidic fidelity during growth and stimulation studies. An advantage of this annealing process is that humidified cell culture conditions (37 ^{o}C) favor the E-PDMS bonding process, rather than counteract it.

This simple, effective fabrication method will expand the range of possibilities for process miniaturization and sample manipulation in tightly-bound, biocompatible, PDMS-based microfluidics. Solvent extraction or autoclaving alone improve material biocompatibility. Combining these easy processes in sequence retains material biocompatibility while increasing material adhesion, thus improving the versatility of applications of E-PDMS for microfluidic platforms. It is yet to be determined how E-PDMS microfluidics will be advantageous for chemical synthesis, material interactions, flexible electronics, or PDMS surface modifications, but the implications from PDMS deformation from oligomer translocation may prove valuable.

Oligomer translocation between PDMS types is evident through material deformation when oligomer-free, E-PDMS is placed in contact with oligomer-containing PDMS and subjected to elevated temperatures. This provides a possible approach for optimizing curing agent and pre-polymer ratios, and curing conditions to minimize oligomer translocation through, and out of, PDMS.

Optimal cell signaling results when environmental confounds are eliminated. E-PDMS microfluidics are devoid of free oligomers, which are known to accumulate in cells and modify gene transcription. E-PDMS microfluidic platforms are advantageous for a wide range of signaling studies for monotypic cell cultures or co-cultures.

Literature cited

1. Millet, L. J. & Gillette, M. U. New perspectives on neuronal development via microfluidic environments. *Trends Neurosci.* **35,** 752–761 (2012).

2. Millet, L. J. & Gillette, M. U. Over a century of neuron culture: from the hanging drop to microfluidic devices. *Yale J. Biol. Med.* **85,** 501–21 (2012).

3. Selimović, S., Dokmeci, M. R. & Khademhosseini, A. Organs-on-a-chip for drug discovery. *Curr. Opin. Pharmacol.* **13,** 829–33 (2013).

4. Taylor, A. M., Dieterich, D. C., Ito, H. T., Kim, S. A. & Schuman, E. M. Microfluidic local perfusion chambers for the visualization and manipulation of synapses. *Neuron* **66,** 57–68 (2010).

5. Taylor, A. M. *et al.* A microfluidic culture platform for CNS axonal injury, regeneration and transport. *Nat Methods* **2,** 599–605 (2005).

6. Baker, B. M. & Chen, C. S. Deconstructing the third dimension - how 3D culture microenvironments alter cellular cues. *J. Cell Sci.* **125,** 3015–3024 (2012).

7. Nahavandi, S. *et al.* Microfluidic platforms for the investigation of intercellular signalling mechanisms. *Small* **10,** 4810–4826 (2014).

8. Guo, F. *et al.* Probing cell-cell communication with microfluidic devices. *Lab Chip* **13,** 3152–62 (2013).

9. Ren, M., Du, C., Herrero Acero, E., Tang-Schomer, M. D. & Özkucur, N. A biofidelic 3D culture model to study the development of brain cellular systems. *Sci. Rep.* **6,** 24953 (2016).

10. Puschmann, T. B. *et al.* Bioactive 3D cell culture system minimizes cellular stress and maintains the in vivo-like morphological complexity of astroglial cells. *Glia* **61,** 432–440 (2013).

11. Kraus, D., Boyle, V., Leibig, N., Stark, G. B. & Penna, V. The Neuro-spheroid-A novel 3D in vitro model for peripheral nerve regeneration. *J. Neurosci. Methods* **246,** 97–105 (2015).

12. Jain, A. & Gillette, M. U. Development of microfluidic devices for the manipulation of neuronal synapses. *Neuromethods* **103,** 127–137 (2015).

13. Sia, S. K. & Whitesides, G. M. Microfluidic devices fabricated in poly(dimethylsiloxane) for biological studies. *Electrophoresis* **24,** 3563–3576 (2003).

14. Mata, A., Fleischman, A. J. & Roy, S. Characterization of polydimethylsiloxane (PDMS) properties for biomedical micro/nanosystems. *Biomed. Microdevices* **7,** 281–93 (2005).

15. Łopacińska, J. M., Emnéus, J. & Dufva, M. Poly(Dimethylsiloxane) (PDMS) Affects Gene Expression in PC12 Cells Differentiating into Neuronal-Like Cells. *PLoS One* **8,** (2013).

16. Regehr, K. J. *et al.* Biological implications of polydimethylsiloxane-based microfluidic cell culture. *Lab Chip* **9,** 2132–2139 (2009).

17. Walker, G. M., Zeringue, H. C. & Beebe, D. J. Microenvironment design considerations for cellular scale studies. *Lab Chip* **4,** 91–97 (2004).

18. Millet, L. J., Stewart, M. E., Sweedler, J. V, Nuzzo, R. G. & Gillette, M. U. Microfluidic devices for culturing primary mammalian neurons at low densities. *Lab Chip* **7,** 987–994 (2007).

19. Millet, L. J., Stewart, M. E., Nuzzo, R. G. & Gillette, M. U. Guiding neuron development with planar surface gradients of substrate cues deposited using microfluidic devices. *Lab Chip* **10,** 1525–1535 (2010).

20. Toepke, M. W. & Beebe, D. J. PDMS absorption of small molecules and consequences in microfluidic applications. *Lab Chip* **6,** 1484–1486 (2006).

21. Hillborg, H., Sandelin, M. & Gedde, U. W. Hydrophobic recovery of polydimethylsiloxane after exposure to partial discharges as a function of crosslink density. *Polymer (Guildf).* **42,** 7349–7362 (2001).

22. Hillborg, H., Tomczak, N., Olàh, A., Schönherr, H. & Vancso, G. J. Nanoscale hydrophobic recovery: A chemical force microscopy study of UV/ozone-treated cross-linked poly(dimethylsiloxane). *Langmuir* **20,** 785–94 (2004).

23. Duffy, D. C., McDonald, J. C., Schueller, O. J. A. & Whitesides, G. M. Rapid prototyping of microfluidic systems in poly(dimethylsiloxane). *Anal. Chem.* **70,** 4974–4984 (1998).

24. Langowski, B. a & Uhrich, K. E. Oxygen plasma-treatment effects on Si transfer. *Langmuir* **21,** 6366–72 (2005).

25. McCarthy, K. D. & de Vellis, J. Preparation of separate astroglial and oligodendroglial cell cultures from rat cerebral tissue. *J. Cell Biol.* **85,** 890–902 (1980).

26. Ramamoorthy, P. & Whim, M. D. Trafficking and fusion of neuropeptide Y-containing dense-core granules in astrocytes. *J. Neurosci.* **28,** 13815–13827 (2008).

27. Jo, K. *et al.* Mass spectrometric imaging of peptide release from neuronal cells within microfluidic devices. *Lab Chip* **7,** 1454–1460 (2007).

28. Hassinger, T. D., Guthrie, P. B., Atkinson, P. B., Bennett, M. V & Kater, S. B. An extracellular signaling component in propagation of astrocytic calcium waves. *Proc. Natl. Acad. Sci. U. S. A.* **93,** 13268–13273 (1996).

29. Bowser, D. N. & Khakh, B. S. Vesicular ATP is the predominant cause of intercellular calcium waves in astrocytes. *J. Gen. Physiol.* **129,** 485–491 (2007).

30. Verkhratsky, A., Orkand, R. K. & Kettenmann, H. Glial calcium: homeostasis and signaling function. *Physiol. Rev.* **78,** 99–141 (1998).

31. Zonta, M. *et al.* Neuron-to-astrocyte signaling is central to the dynamic control of brain microcirculation. *Nat. Neurosci.* **6,** 43–50 (2003).

32. Parri, H. R., Gould, T. M. & Crunelli, V. Spontaneous astrocytic Ca2+ oscillations in situ drive NMDAR-mediated neuronal excitation. *Nat. Neurosci.* **4,** 803–812 (2001).

33. James, L. R. *et al.* High-throughput analysis of calcium signalling kinetics in astrocytes stimulated with different neurotransmitters. *PLoS One* **6,** e26889 (2011).

34. Nett, W. J., Oloff, S. H. & Mccarthy, K. D. Hippocampal Astrocytes In Situ Exhibit Calcium Oscillations That Occur Independent of Neuronal Activity Hippocampal Astrocytes In Situ Exhibit Calcium Oscillations That Occur Independent of Neuronal Activity. *J neurophysiol* **87,** 528–537 (2002).

35. Fiacco, T. a & McCarthy, K. D. Intracellular astrocyte calcium waves in situ increase the frequency of spontaneous AMPA receptor currents in CA1 pyramidal neurons. *J. Neurosci.* **24,** 722–32 (2004).

36. Pasti, L., Volterra, A., Pozzan, T. & Carmignoto, G. Intracellular Calcium Oscillations in Astrocytes : A Highly Plastic , Astrocytes In Situ. *J. Neurosci.* **17,** 7817–7830 (1997).

37. Finkbeiner, S. M. Glial calcium. *Glia* **9,** 83–104 (1993).

38. Lee, S. H., Kim, W. T., Cornell-Bell, a H. & Sontheimer, H. Astrocytes exhibit regional specificity in gap-junction coupling. *Glia* **11,** 315–25 (1994).

39. Nedergaard, M. Direct signaling from astrocytes to neurons in cultures of mammalian brain cells. *Science* **263,** 1768–1771 (1994).

40. Hosmane, S., Yang, I. H., Ruffin, A., Thakor, N. & Venkatesan, A. Circular compartmentalized microfluidic platform: Study of axon-glia interactions. *Lab Chip* **10,** 741–747 (2010).

41. Shi, M. *et al.* Glia co-culture with neurons in microfluidic platforms promotes the formation and stabilization of synaptic contacts. *Lab Chip* **13,** 3008–21 (2013).

42. Robertson, G., Bushell, T. J. & Zagnoni, M. Chemically induced synaptic activity between mixed primary hippocampal co-cultures in a microfluidic system. *Integr. Biol. (Camb).* **6,** 636–44 (2014).

43. Park, J., Koito, H., Li, J. & Han, A. Multi-compartment neuron–glia co-culture platform for localized CNS axon–glia interaction study. *Lab on a Chip* **12,** 3296 (2012).

44. Hosmane, S. *et al.* Toll/Interleukin-1 Receptor Domain-Containing Adapter Inducing Interferon-β Mediates Microglial Phagocytosis of Degenerating Axons. *J. Neurosci.* **32,** 7745–57 (2012).

45. Majumdar, D., Gao, Y., Li, D. & Webb, D. J. Co-culture of neurons and glia in a novel microfluidic platform. *J Neurosci Methods* **196,** 38–44 (2011).

Figures

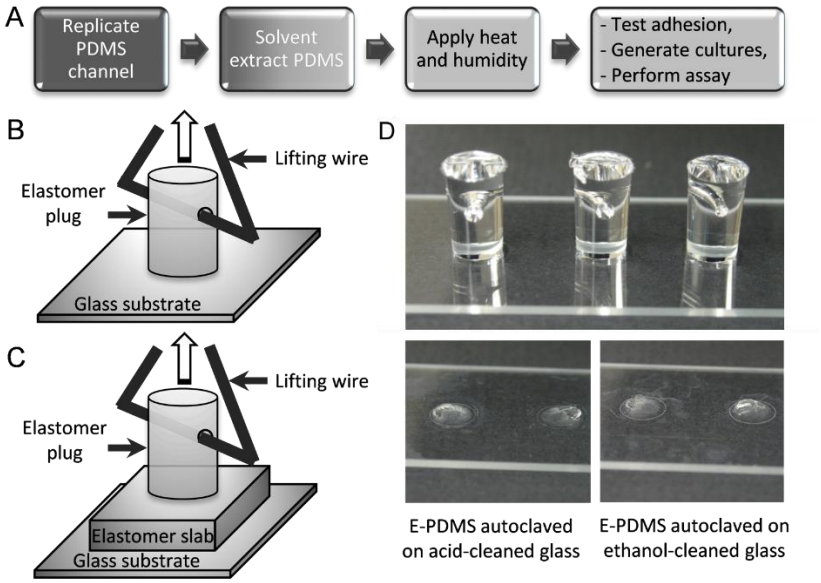

Figure 4.1. Overview of E-PDMS annealing process and adhesion measurements. (A) General overview of annealing process, from replicate molding of PDMS through cell culture. For microfluidics, masters are used to generate the PDMS microchannels. For plugs to measure adhesion forces, a 96-well plate serves as the replicate mold. Solvent extraction was performed with n-pentane, xylene, ethanol (200 proof), and water. (B, C) Schematic of PDMS elastomeric plugs and substrate configurations. Holes punched through the plugs allow for wire supports to attach to the force scales. PDMS on glass (B) was used for annealing measures. PDMS on PDMS (C) was used to measure material deformations through profilometry. (D) Images of 3 plugs on a microscope slide for force measurements (upper image). E-PDMS plugs form strong adhesion bonds after solvent extraction and autoclaving. It is typical for E-PDMS annealed after extraction and autoclaving to tear, leaving elastomer fragments when being pulled off the glass, irrespective of glass cleaning method (lower images).

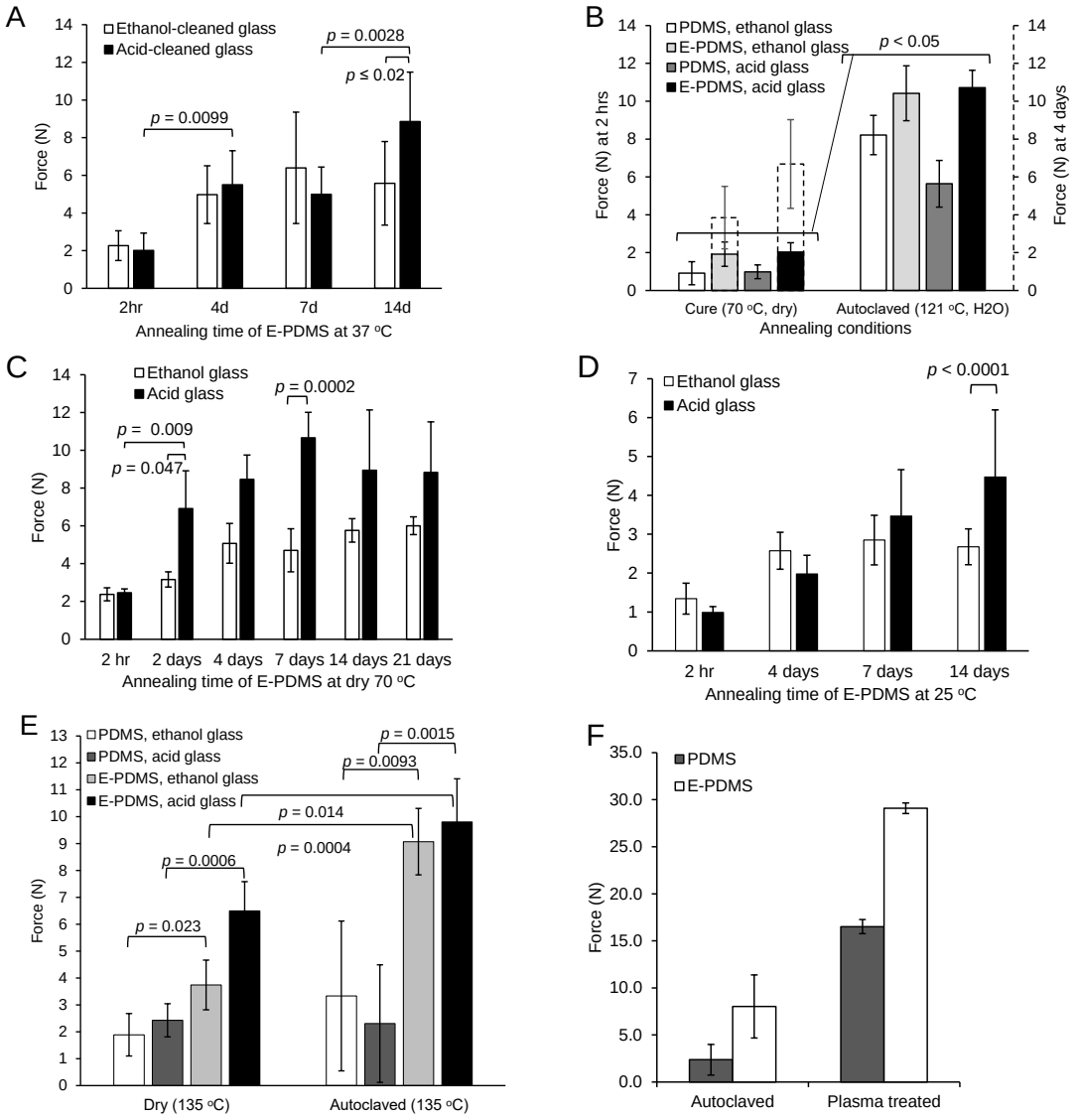

Figure 4.2. Measurements of removal forces for annealed E-PDMS and PDMS plugs. (A) Forces required to remove annealed (humidified 37 ºC) E-PDMS plugs off glass slides were measured. Similar results are achieved for both ethanol and acid-cleaned glass at 37 ºC. (B) Significant temporal effects of two annealing conditions were tested for both PDMS and E-PDMS plugs on ethanol-cleaned glass (white and light grey bars) and acid-cleaned glass (dark grey and black bars). E-PDMS annealed with dry heat (4 days) has a significant effect on changes of removal forces. Autoclave annealing produces superior bonding forces. (C) Temporal-dependence of annealing E-PDMS with 70 ºC dry heat. (D) E-PDMS plugs retained at ambient temperature and humidity show increased removal forces over a two-week period. (E) Measurements of high temperature-matched annealing (135ºC) under dry or humidified conditions show that heat, humidity, and E-PDMS produce the highest bonding forces. (F) Comparison of extraction-autoclave annealing to plasma-heat annealing. E-PDMS out performs PDMS in both cases (n=4, One-way ANOVA, $p<0.05$). (A-E) n=8, Two-way ANOVA.

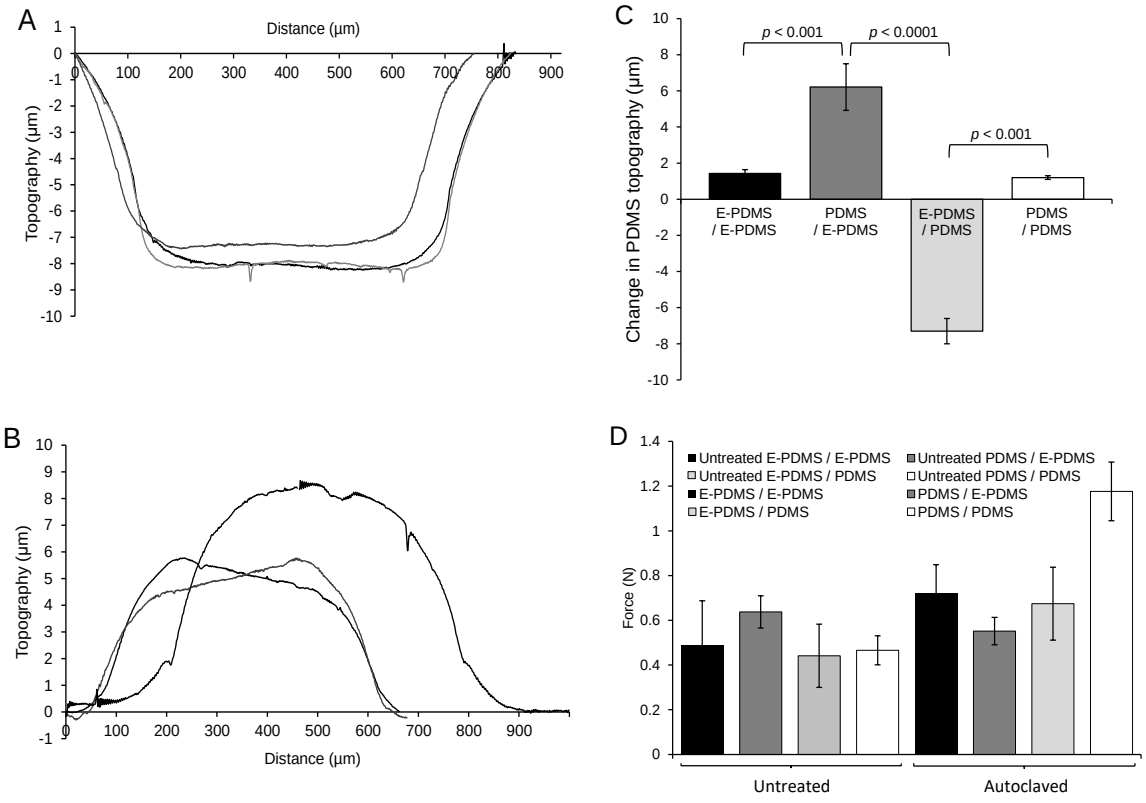

Figure 4.3. Measurement of deformation and removal forces for E-PDMS and PDMS in direct contact. (A, B) Profilometry data confirms the visual observations of E-PDMS and PDMS deformation when extracted and non-extracted samples in direct contact are autoclaved. (C) Results of changes in topography from profilometry data of E-PDMS and PDMS plugs in contact with the E-PDMS and PDMS slabs. PDMS/E-PDMS combinations show much greater changes ($p < 0.001$, 3 repeats (n=3 each), One-way ANOVA) than both E-PDMS/E-PDMS and PDMS/PDMS; matched material types show no significant changes. D) Removal force measurements of autoclave-annealed E-PDMS and PDMS plugs on E-PDMS and PDMS slabs. Weak removal forces for PDMS on PDMS are higher than any E-PDMS interactions and are attributed to the remaining oligomers and metal catalysts left in the bulk polymer (no significance).

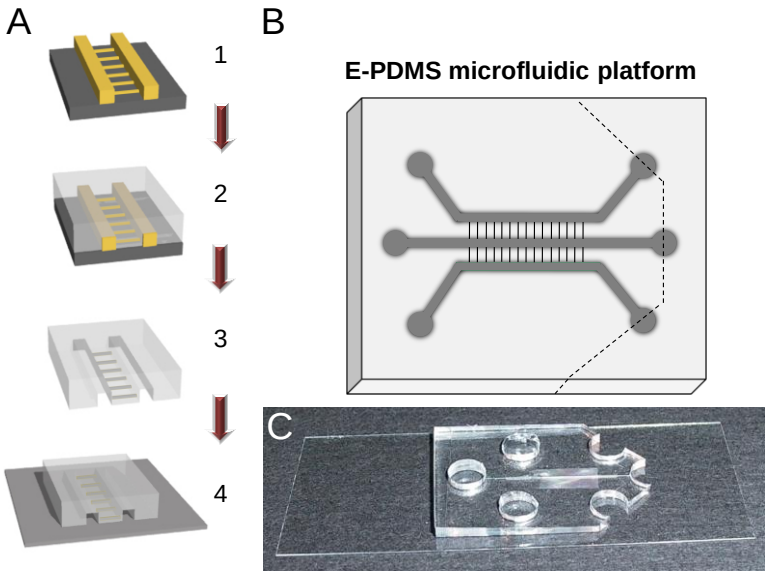

Figure 4.4. Assembly of microfluidic devices for cell signaling studies. (A) Overview of fabrication and assembly process for microfluidic chambers (200 μm W x 45 μm H) for cell signaling. [18] (1) Microfluidic masters are used for (2) replicate molding of PDMS-based microfluidic channels with interconnecting tunnels (7x7x45 μm). (3) PDMS replicates are trimmed and holes punched (upper right diagram) prior to solvent extraction to remove un-cross-linked oligomers and metal catalysts. (4) E-PDMS replicate is annealed to the glass substrate through autoclave sterilization, completing the microfluidic device. (B, C) Architecture (B) and photograph (C) of an annealed E-PDMS microfluidic device used for cell signaling studies. Ports are cut with dermal biopsy punches (5-6 mm). The reservoir is made by bisecting three ports on one end of the platform (dashed line).

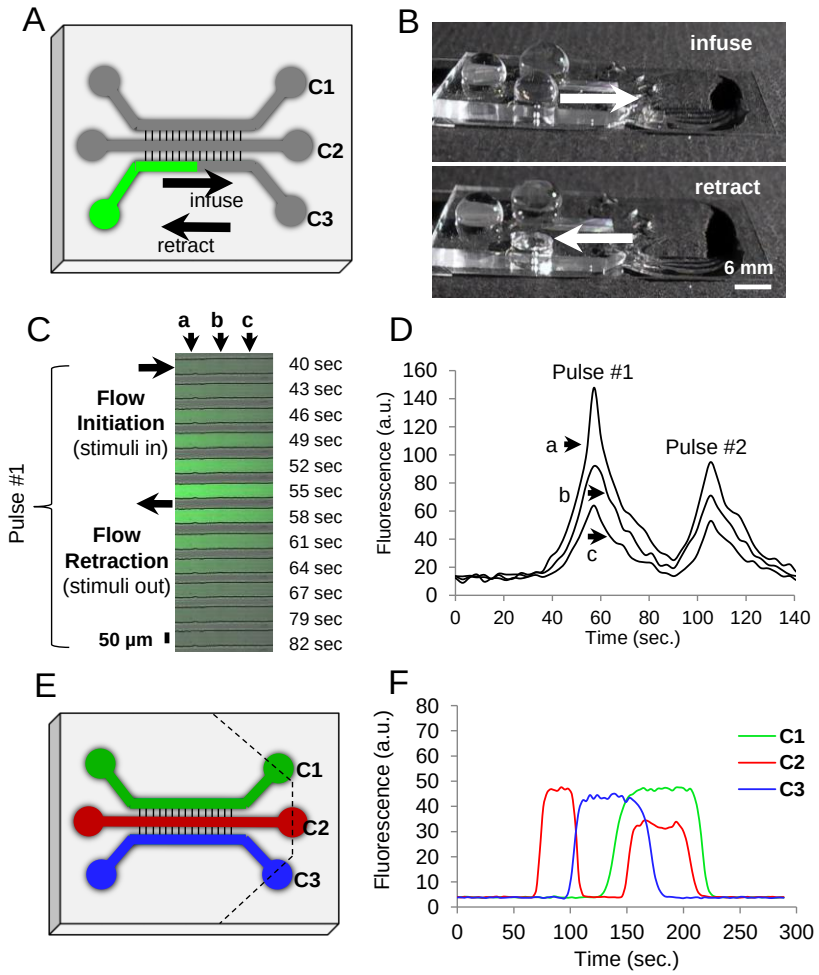

Figure 4.5. Chemo-temporal pulses in microfluidic channels. (A) Schematic and image of PDMS channels on a coverslip for a fluidically-connected microfluidic platform for cell signaling. (B) Using surface tension and gravity flow, chemicals can be pulsed in the channel for stimulating compartmentalized cells. (C) For pulse characterization, dilute FITC-conjugated secondary antibodies (green) were introduced in the channel. Spatial characteristics were assessed at three separate points 125 µm apart (a, b, c). (D) Two serial pulses demonstrate spatio-temporal characteristics for multiple cellular stimulations. In pulse #1, half-maximal stimulation concentration is achieved at peak (a) with a concentration decay of 40% at peak (b), and 57% at peak (c). Positions of points a, b, c as in (C). (E) Parallel pulsatile flow actuated by surface tension and gravity-mediated passive pumping within the same device. The device was cut along the dashed lines to allow for unrestricted outflow. Pulsatile flow was accomplished as shown in (B) with an increased fluid head at the inlet initiating channel infusion, and emptying of the inlet resulting in flow retraction. (F) Flow in the three individual channels (C1, C2, C3) can be modulated independently to produce spatio-temporal pulses as depicted in the profiles of fluorescence. Flow was initiated in C3 at the same time as the first flow retraction from C2, followed by flow initiation in C3 and re-infusion of C2 simultaneous with flow retraction from C3, ending with serial retractions from C2 and C3.

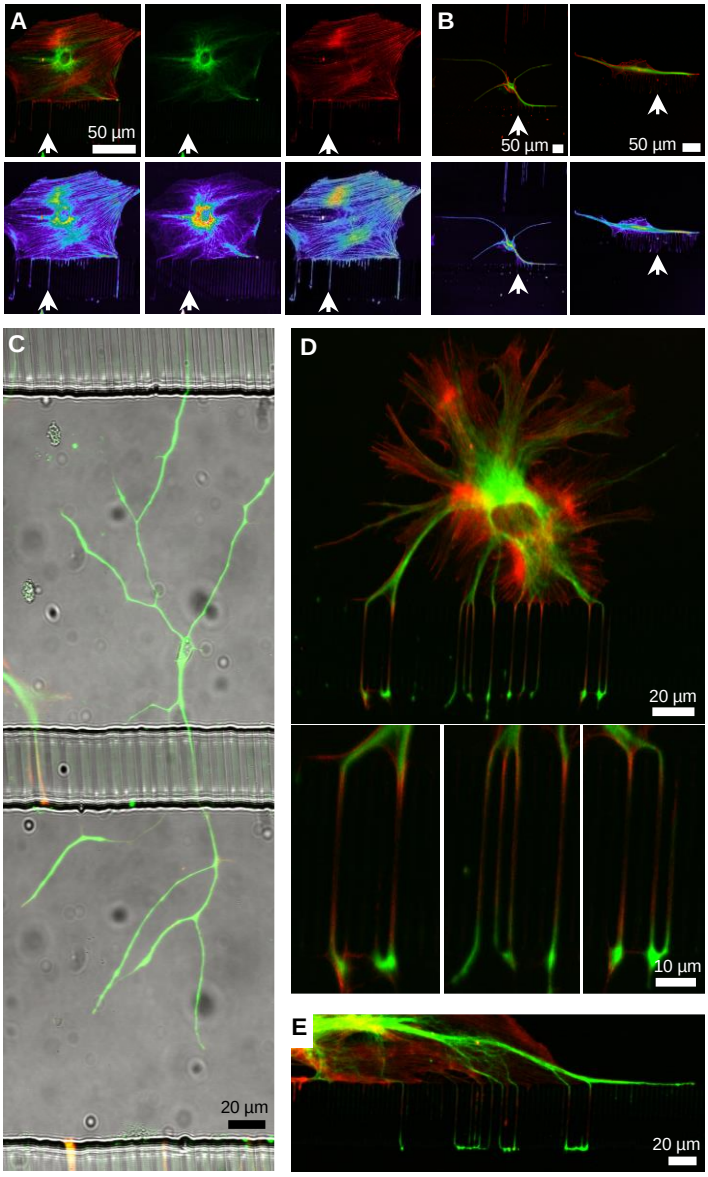

Figure 4.6. Compartmentalization of glia in microfluidic channels. (A, B) Glial cells cultured in E-PDMS microfluidics develop cellular branches that extend through interconnects. Antibodies for glial fibrillary acidic protein (green) and rhodamine phalloidin (phalloidin, red) label the cytoskeleton. Fluorescence intensities of cell branches are represented by glow-scale intensity images (below). Fine, filamentous glial branches are rich in filamentous actin and contain GFAP filaments. (B) Merged fluorescence images of two glial cells are shown, each in its own image pane. (C) Large (~400 µm long), ramified glial cells do not show affinity for channel walls and interconnects as most glial cells do. (D) A glial cell in the top channel extends branches into the bottom channel allowing subcellular stimulation with signaling molecules applied through adjacent channels. Insets show magnified views of glial branches wrapping around the interconnect pillars, merging as they emerge into the bottom channel. (E) Glial cells often spread along the channel wall sending branches over distances exceeding 100 µm, increasing the efficiency of inter-channel signaling.

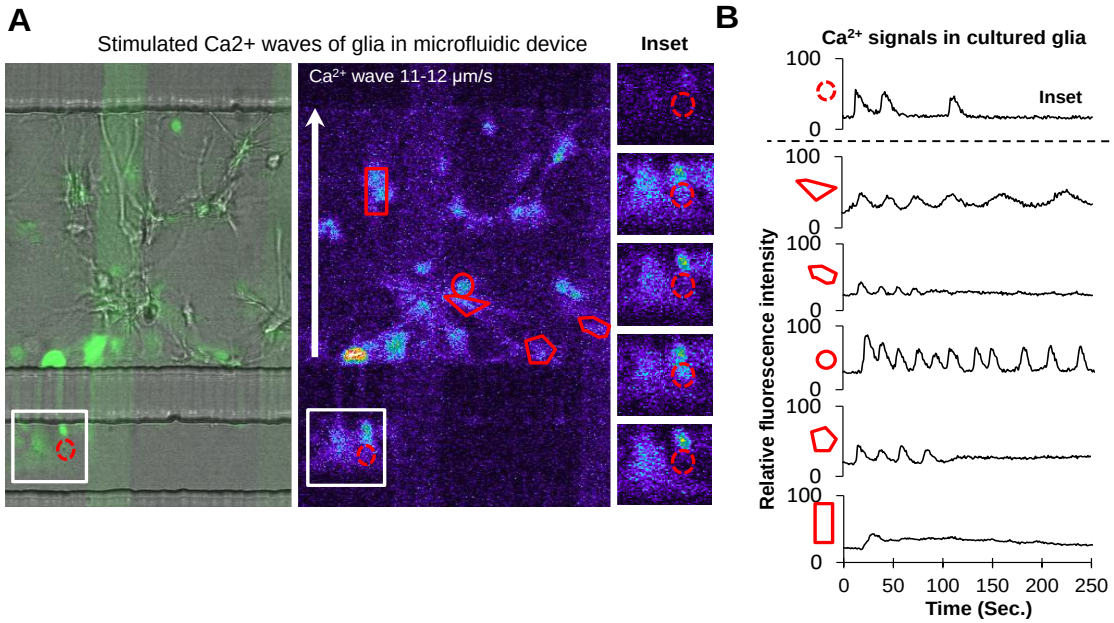

Figure 4.7. Ca^{2+} signals of glial networks in E-PDMS microfluidics. (A) Primary glial cells proliferate and extend branches into adjacent microchannels through interconnects. All channels were loaded with Ca^{2+} indicator (Fluo-4 AM in PBS). Glial cell branches were stimulated via 10 µM ATP infusion (left to right) through stimulation channel (bottom). A combined brightfield and fluorescence image is shown (left) alongside the respective fluorescence intensity glow-scale image (right); FITC-PLL lines (green) on glass are reference markers. Segmented images of inset (right) demonstrate repeated Ca^{2+} fluctuations. (B) Fluorescence profiles of Ca^{2+} responses from respective ROI demonstrate the range of characteristic Ca^{2+} responses for cultured astrocytes. Glia cultured in microdevices exhibit a typical range of Ca^{2+} fluxes that vary in frequency, amplitude, and duration.

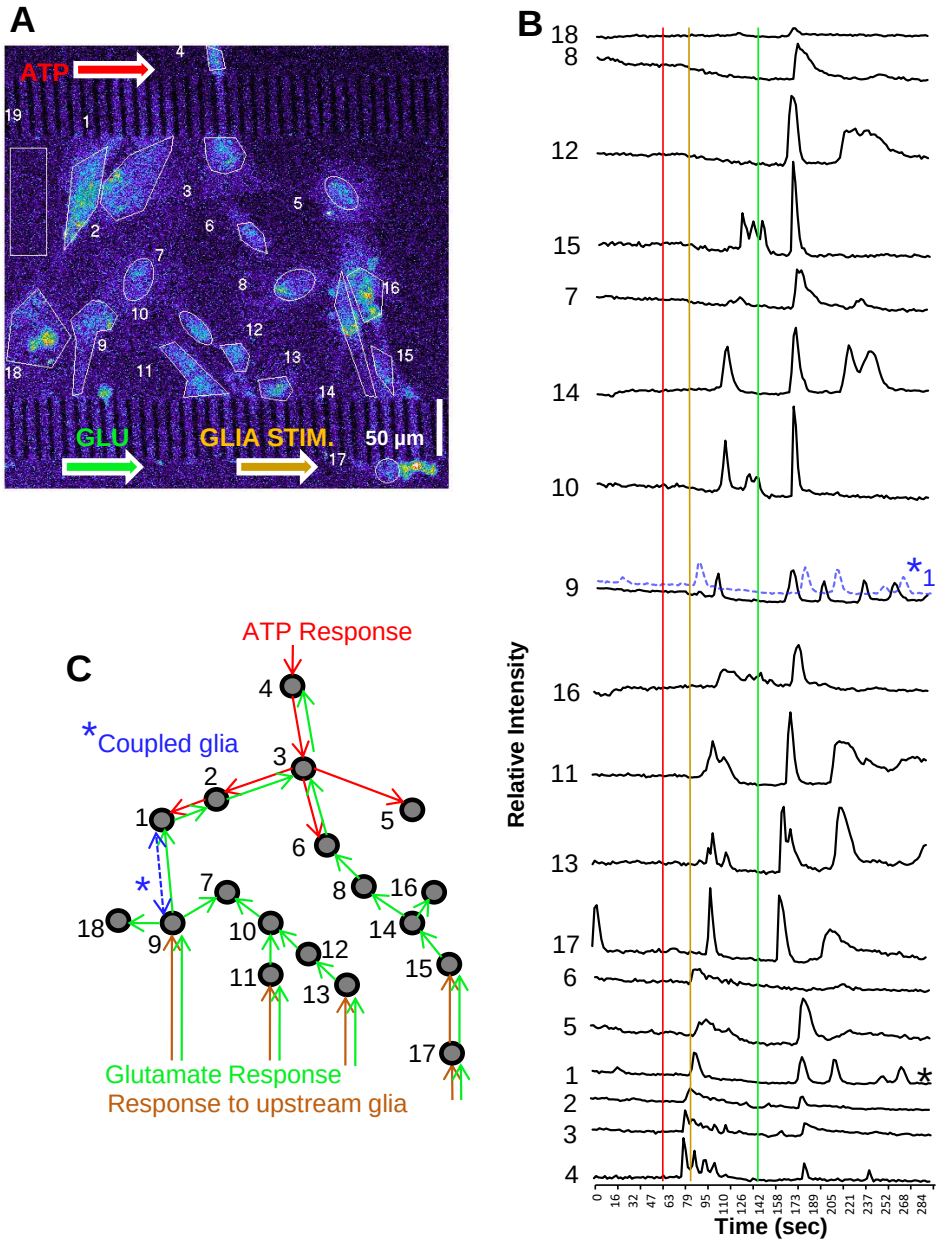

Figure 4.8. Glial network activation through multipoint stimulation. (A) Glia were cultured in the central channel of a microfluidic platform for stimulation at opposite sides of the culture for observing network activity. First, 20 µM ATP was introduced, then 50 µM glutamate was inserted into the bottom channel. From two chemical stimulations, three network activations occur. (B) Background (ROI#19)-subtracted fluorescence intensity profiles of each defined RIO ordered in chronological activation. Temporally-coupled signals from cellular ROI 1 and 9 suggest the two cells are electrically coupled. (C) Schematic summary of Ca^{2+} signal propagation through the glial population.

CHAPTER 5: SUMMARY AND CONCLUSIONS

The intricate wiring of the nervous system relies on filopodial navigation to form complex interconnections between neurons through their axons, dendrites, and the cell soma itself. Until recently, cellular investigations into filopodial dynamics had focused primarily on axonal growth cone filopodia. Spurred by technological advances, scientists have now begun to explore the structural and functional landscape of dendritic filopodia. Fully functioning dendritic filopodia have been shown to be critical to the establishment of neuronal connectivity through dendritic morphogenesis, spinogenesis and synaptogenesis. Anomalies in these processes are at the root of several developmental disorders, such as Down's syndrome,[1,2] Fragile-X mental retardation,[3] schizophrenia, Alzheimer's,[4] and mood disorders.[5] Better comprehension of the processes that shape development can help deconstruct the underlying mechanisms of these developmental disorders and diseases, thereby, aiding the advancement of cures and relief. Hence, with a view towards furthering our understanding of network formation in the brain, the aim of this work was to examine the differential presentation and behavior of filopodia along the tips and shafts of dendrites of primary hippocampal neurons.

Neuronal filopodia borne along tips and shafts of dendrites exhibit distinct behaviors

Conducting structural analyses using membrane and actin labels we found that tips bear longer filopodia, and at higher densities. We examined filopodial mass change dynamics using Spatial Light Interference Microscopy (SLIM), an innovative quantitative phase imaging method.[6] SLIM enables high-resolution label-free imaging of live cells

and allows measurements of the dry mass of live neurons, and even individual filopodia, at femtogram levels. Time-lapse SLIM analysis of the mass-change dynamics of dendritic filopodia showed that (1) tip filopodia show significantly higher rates of change of mass, for both growth and shrinkage, as compared to shaft filopodia, and (2) both tip and shaft filopodia exhibit an exponential growth, i.e., the rate of growth increases as filopodial mass increases.

Together these investigations into structure and dynamics provide further evidence for differences in the two filopodial populations – those borne on the tips, and those along the shafts, of dendrites.[7,8] They strengthen the argument that the two populations be treated as distinct in future studies into filopodial and dendrite development.

An intriguing extension of this work would be the examination of external influences on tip and shaft filopodia – if, and how, a filopodium's interaction with its neighboring filopodia, with other cells or neurites, and with debris and other topographical features, influence its presentation and behavior. The exponential growth might be demonstrative of the mechanical obstacles faced by a budding filopodium, such as membrane resistance, that might be easier to overcome with increasing mass. It could also hint to a cooperative recruitment of the machinery employed in filopodial extension. Another characteristic feature of systems that show exponential growth is the existence of checkpoints or regulatory systems that keep the growth in check. The actin cytoskeletal system that forms the core of filopodial dynamics, is a system that lends itself especially well to control and regulation. The nuances of this regulation and how it pertains to the

maintenance of an exponential growth rate in filopodia are questions that merit further investigation.

Semaphorin3A differentially instructs the development of tip and shaft filopodia

Our next set of experiments was aimed at understanding the functional ramifications of the differences in structure and dynamics in tip and shaft filopodia. Towards this aim, we investigated the responses of the two filopodial populations to Semaphorin3A (Sema3A). Sema3A is a unique cue that acts as a repulsive guidance cue for axons,[9,10] and an attractive guidance cue for dendrites.[11,12] Furthermore, it plays a multifaceted role in filopodial development, guiding dendritic morphogenesis, spinogenesis, and synaptogenesis.[13,14] In investigating these aspects of Sema3A's regulation of filopodial development, we found that a 24 h exposure to Sema3A administered 1 h after cell seeding leads to an acceleration of the maturation of shaft filopodia as evidenced by (1) an increase in the branching of the dendrites, (2) an acceleration of maturation of shaft filopodia into spines and (3) into synapses. An analysis of the underlying dynamics using time-lapse SLIM imaging showed that early exposure to Sema3A results in (1) an increase in average growth and shrinkage rates in shaft filopodia selectively, and, (2) an increase in speed of the fastest growth and shrinkage observed for tip and shaft filopodia at 4 and 7 DIV. Since Sema3A acts as a repulsive cue for axons, inducing collapse of axonal growth cones, a bath application of Sema3A to neurons would have adverse effects for the axon that might then spill over to suppress or modify the behavior of the rest of the cell, possibly even dendritic filopodia. To confirm that our findings were not affected by such a confound, and to better replicate

the *in vivo* layered structure of the hippocampus, we employed microfluidic devices that enable compartmentalization of neurons into fluidically distinct microenvironments. This allowed selective Sema3A stimulation of the dendrites only, leaving the rest of the cell unaffected. Our results held true even with this sub-cellular administration of Sema3A, with tip and shaft filopodia displaying distinct behaviors in terms of structure as well as dynamics.

Together these findings show that Sema3A is a unique cue that acts on both tip filopodia and shaft filopodia, but with different outcomes – the former to increase dendrite lengths, and the latter to increase branching, spinogenesis and synaptogenesis. (Figure 5.1) This compounds the evidence for the two filopodial populations being distinct, not only in terms of structure and dynamics, but also functionally, in their responses to developmental cues. Furthermore, these findings help deconstruct the role of Sema3A in dendritic development.

An interesting next step to these investigations would be an examination of the difference in the intracellular environments of tip and shaft filopodia, such as in their levels of cyclic nucleotides and calcium, which would help in further elucidating the mechanism of the differential influence of Sema3A on the two populations. Another avenue that promises answers to some of the questions raised here, is a closer examination of the cytoskeletal organization in shaft filopodia in the earlier developmental stages of 4 and 7 DIV – do these filopodia start out with a crisscross branched actin network organization? Or do early stage shaft filopodia resemble tip filopodia in possessing a parallel actin bundle organization, and only late stage shaft filopodia mature into a crisscross organization. The latter could be a preparation for

filopodial transition to the cytoskeletal organization of spines and post-synaptic structures.

Microdevices enable focal stimulation of cellular networks

Our work on employing microfluidic devices towards regulating the microenvironment of primary neurons helped us identify the pressing need for a new technique of device preparation that is better suited for probing such sensitive biological systems.[15–17] This led us to develop new approach towards fabricating these environments – employing a sequential combination of solvent extraction and autoclave annealing to generate unique binding properties for polydimethylsiloxane (PDMS), the polymer used to fabricate these devices. This treatment ensures the dual benefits of (1) high strength bonds between the solvent-extracted PDMS (E-PDMS) and glass, and (2) the highest material biocompatibility as achieved through the removal of free uncrosslinked oligomers. We demonstrated this by comparing adhesion strengths of E-PDMS and conventional PDMS on glass as determined by measuring the force required to remove the respective elastomer plugs from glass slides. We also quantified elastomer deformations in PDMS and E-PDMS assemblies which are indicative of oligomer translocation from PDMS to oligomer-free E-PDMS. Proceeding to applications, we exploited the unique capabilities of these E-PDMS devices to elicit Ca^{2+} oscillations in compartmentalized glial cell networks in response to focal pulses of ATP and glutamate. The tight interface allowed for maximal manipulation of fluid dynamics while the solvent extraction ensured elimination of oligomer-induced artifacts in cellular read-outs. Thus, we advanced a new approach to PDMS microfluidic assembly, the unique properties of

which present unparalleled context for unraveling cellular changes occurring at the micro- and nano-scales, thereby aiding further elucidation of the nuances of cell signaling and network formation.

Conclusion

The convergence of filopodial investigations and the technology for engineering micro-environments, when coupled with high resolution imaging and analysis, has enabled new insights on filopodial heterogeneity, into differences in the presentation and behavior of tip and shaft filopodia of neuronal dendrites, and their responses to local signals, specifically, Sema3A, that helps initiate and establish neuron-neuron interactions at the filopodial level. With dendritic filopodia being at the core of the processes of spinogenesis, synaptogenesis and dendritic morphogenesis, these findings will aid greater comprehension of the processes of neuronal patterning and network formation, and will help unravel the mechanistic bases of developmental disorders and diseases.

Literature cited

1. Becker, L. E., Armstrong, D. L. & Chan, F. Dendritic atrophy in children with Down's syndrome. *Ann. Neurol.* **20,** 520–526 (1986).

2. Takashima, S., Iida, K., Mito, T. & Arima, M. Dendritic and histochemical development and ageing in patients with Down's syndrome. *J. Intellect. Disabil. Res.* **38 (Pt 3),** 265–73 (1994).

3. Irwin, S. A., Galvez, R. & Greenough, W. T. Dendritic spine structural anomalies in fragile-X mental retardation syndrome. *Cereb. Cortex* **10,** 1038–44 (2000).

4. Good, P. F. *et al.* A role for semaphorin 3A signaling in the degeneration of hippocampal neurons during Alzheimer's disease. *J. Neurochem.* **91,** 716–36 (2004).

5. Law, A. J., Shannon Weickert, C., Hyde, T. M., Kleinman, J. E. & Harrison, P. J. Reduced Spinophilin But Not Microtubule-Associated Protein 2 Expression in the Hippocampal Formation in Schizophrenia and Mood Disorders: Molecular Evidence for a Pathology of Dendritic Spines. *Am J PsychiatryAm J Psychiatry* **161,** 1848–1855 (2004).

6. Wang, Z. *et al.* Spatial light interference microscopy (SLIM). *Opt. Express* **19,** 1016 (2011).

7. Portera-Cailliau, C., Pan, D. T. & Yuste, R. Activity-regulated dynamic behavior of early dendritic protrusions: evidence for different types of dendritic filopodia. *J. Neurosci.* **23,** 7129–42 (2003).

8. Korobova, F. & Svitkina, T. Molecular architecture of synaptic actin cytoskeleton in hippocampal neurons reveals a mechanism of dendritic spine morphogenesis. *Mol. Biol. Cell* **21,** 165–76 (2010).

9. Raper, J. A. & Kapfhammer, J. R. The enrichment of a neuronal growth cone collapsing activity from embryonic chick brain. *Neuron* **4,** 21–29 (1990).

10. Fournier, A. E. *et al.* Semaphorin3A enhances endocytosis at sites of receptor-F-actin colocalization during growth cone collapse. *J. Cell Biol.* **149,** 411–421 (2000).

11. Polleux, F., Morrow, T. & Ghosh, A. Semaphorin 3A is a chemoattractant for cortical apical dendrites. *Nature* **404,** 567–73 (2000).

12. Song, H. *et al.* Conversion of Neuronal Growth Cone Responses from Repulsion to Attraction by Cyclic Nucleotides. *Science (80-.).* **281,** (1998).

13. Morita, A. *et al.* Regulation of dendritic branching and spine maturation by semaphorin3A-Fyn signaling. *J. Neurosci.* **26,** 2971–80 (2006).

14. Yamashita, N. *et al.* Regulation of Spine Development by Semaphorin3A through Cyclin-Dependent Kinase 5 Phosphorylation of Collapsin Response Mediator Protein 1. *J. Neurosci.* **27,** (2007).

15. Millet, L. J., Stewart, M. E., Sweedler, J. V, Nuzzo, R. G. & Gillette, M. U. Microfluidic devices for culturing primary mammalian neurons at low densities. *Lab Chip* **7,** 987–994 (2007).

16. Millet, L. J., Stewart, M. E., Nuzzo, R. G. & Gillette, M. U. Guiding neuron development with planar surface gradients of substrate cues deposited using microfluidic devices. *Lab Chip* **10,** 1525–1535 (2010).

17. Jain, A. & Gillette, M. U. Development of microfluidic devices for the manipulation of neuronal synapses. *Neuromethods* **103,** 127–137 (2015).

Figures

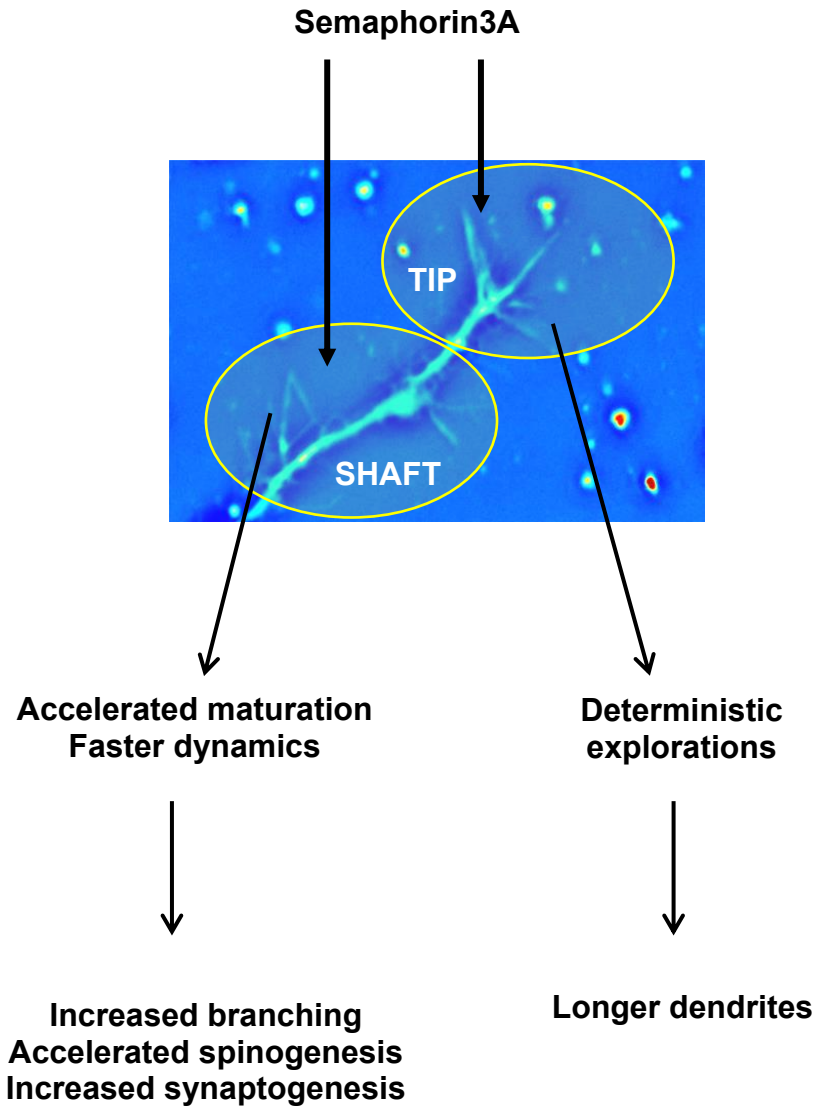

Figure 5.1. Tip and shaft filopodia differ in their response to Sema3a. Sema3A exerts different influences on the development of tip and shaft filopodia. Shaft filopodia respond to a Sema3A treatment with increased densities, and, faster average growth and shrinkage rates, resulting in increased branching, spinogenesis and synaptogenesis. Tip filopodia treated with Sema3A show exploratory movements of a more deterministic nature, eventually resulting in longer dendrites.

APPENDIX A: USING MICROFLUIDIC DEVICES TO CREATE DESIGNER NEURONAL NETWORKS

Abstract

Micro-scale devices, increasingly being employed for studying neurons in highly controlled environments, afford unique strategies for guiding cells within culture systems. Skilled manipulations of fluid flow, physical guidance cues, and other capabilities of these devices provide precise control over positioning of neurons, thereby enabling the creation of made-to-order neuronal networks.

Introduction

Studies in developmental biology revolve around the cues present in a cell's environment and its response to them. Primary among these extracellular factors is the presence and influence of neighboring cells. It is crucial, therefore, for such studies to be able to replicate *in vitro* these network-like conditions. This is especially true of neuroscience, tissue engineering and clinical biology where network formation and functioning are critical aspects of any investigation.

Over the last decade, a number of methodologies have been developed aimed at providing experimentalists with greater control over the positioning of cells.[1] One such

Support was provided by the National Science Foundation IGERT 0965918 (AJ), STC CBET 0939511 (MUG), CBET 1040462 (MUG) and EAGER DBI 1450962 (MUG) and National Institute of Health R21MH101655 (MUG).

group of techniques is based on chemical patterning to make certain regions of the substrate especially attractive or repulsive for cells. However, in several cases, such modifications are undesirable. Other techniques available include the use of laminar flow[2], electrophoretic forces[3], optical tweezers and laser traps[4], microdevices of sophisticated designs,[5,6] and combinations thereof.[7,8,9] Most of these are too expensive or time-consuming, particularly with regards to initial set-up and skill-acquisition.

Here we demonstrate three easy and inexpensive techniques based on microfluidics that provide a high degree of control in positioning cells, thereby enabling the laying down of cellular networks of virtually any desired configuration. We use a polydimethylsiloxane (PDMS) microdevice of a simple, standard design[10,11,12,13] (Figure A.1A) that can be used and re-used. Furthermore, PDMS is not only inexpensive but also flexible, impermeable to water, permeable to gases, non-toxic to cells, and optically transparent down to 230 nm, making it ideal for biological studies.

The techniques described here employ gravitational force, centrifugal force, and suction to control cell positioning.[14] The use of gravitational force is the simplest method, and also the gentlest on the cells; however, it is also the slowest of the three. Application of centrifugal force provides the maximum flexibility in the amount of force applied. The use of suction force, on the other hand, is the least flexible, but it is also the quickest of the three. With these distinct properties the techniques complement each other well and can be used in conjunction in two, or even more, cell-positioning steps to create desired networks. Once positioning has been accomplished, the PDMS device can be removed from the glass, and the culture returned to standard dish-culture conditions, or, it can be

retained, resulting in a device culture with the added properties of higher spatio-temporal control over the application of chemical cues.

Protocols

The following section details steps to create designer neuronal networks. Reagents and equipment required are listed in Table A.1.

1) Preparing the Device

1.1) Use soft lithography to fabricate the device, as described previously.[14]

1.2) Pour the PDMS pre-polymer, a 10:1 mix of base and curing agent, onto the silicon master. Place it in a vacuum desiccator to facilitate the removal of air bubbles. Allow it to cure at 70 ^{o}C for 2 h.

1.3) When cooled, create inlets and outlets using a 4 mm biopsy punch to get the desired design (Figure A.1A).

1.4) Subject the device to a solvent extraction to remove impurities and free oligomers.[11] This can be skipped for cultures where the PDMS device will be removed after cell positioning.

1.5) For device cultures, bond the device to the coverslip using oxygen plasma, or other bonding techniques.[16,17] For dish cultures that require the eventual removal of the device, place the device on the coverslip and autoclave the assembly. In addition to sterilization, autoclaving promotes a strong yet reversible bonding. Unless specified otherwise, all subsequent steps involving the device are to be carried out in a laminar flow hood to avoid contamination.

1.6) Add poly-D-lysine (PDL) to the inlets and apply suction at the outlets to ensure the PDL enters the channels. Leave it to coat for a minimum of 2 h. Rinse out with Neurobasal media prior to cell loading.

1.7) Harvest neurons according to the standard protocol.[18] Re-suspend in Neurobasal to achieve the final cell concentration of 1 x 10^6 cells/ml. To achieve the cell configuration shown in Figure A.1B, seed these cells into the inlet of central channel (C2).

1.8) Apply suction at the outlet of channel C2 to facilitate cell entry into the channel. Confirm under a microscope and stop flow by adding media to the outlet. Cells begin to adhere to the PDL within minutes of stopping of flow, and once adhered, will resist the positioning forces applied. Hence, make sure to avoid any delays once the flow has been stopped. Use one of the following techniques, (2), (3) or (4), to achieve cell positioning.

2) Gravitational Force

2.1) Tape the lid of the dish to the base to prevent its falling off.

2.2) Lean the dish against an incubator wall at an angle of 50^o-70^o such that the channel length is parallel to the ground. Channel C3 should be closest to the incubator floor and channel C1 the farthest, so the cells flow down towards the wall between channels C2 and C3.

2.3) After 15-20 min, when the cells settle, return the device to the hood. Remove the tape, empty the outlets and inlets, and refill the inlets with fresh media to actuate flow before returning the dish to the incubator.

3) Centrifugal Force

3.1) After cells are seeded into the central channel, fill all inlets and outlets with media to just above the brim. Place a fresh sterilized coverslip on top of the device. This creates a cassette that prevents media from spilling, and bubbles from entering into the channels.

3.2) Tape the lid of the dish to its base. Place the dish on an inoculation turntable close to its edge. The length of the channels should be perpendicular to a radius of the turntable circle. Secure the dish in this position with tape.

3.3) Rotate the table at approximately 100-200 rpm for a few sec. Check cell positioning under a microscope. If required, rotation can be repeated until the desired cell packing is achieved. In addition to duration, the force (f) also can be modified, by changing the distance (r) of the dish from the center of the inoculation turntable, and the speed of rotation, since $f = mw^2r$ (where, m = mass, and w = angular velocity). A centrifuge can be used to generate the rotation to allow for finer control of rotation speeds.

3.4) Following cell positioning, remove the tape and coverslip. Carefully return the device to the incubator, ensuring there is no flow that might dislodge cells. Leave the device undisturbed in the incubator for 15-20 min.

3.5) When the cells have adhered, return the device to the sterile hood. Empty the outlets and inlets, and refill the inlets with fresh media to actuate flow before returning the dish to the incubator.

4) Suction

4.1) Before harvesting cells, create a PDMS plug by pouring PDMS pre-polymer into one of the wells of a 96-well plate to a level about 4 mm above the brim, such that it forms a

dome on top. De-gas in a vacuum desiccator and cure as described in Step 1.2. Pry out the plug using forceps to obtain a ‘cupcake-shaped’ PDMS plug.

4.2) When cells have been seeded into the central channel and flow has been stopped, hold the PDMS plug at the inlet of channel C3 in an upside-down cupcake orientation. Press it down gently. The dome shape ensures good contact between the plug and the rim of the inlet; the pressure creates a seal. A sterilized coverslip can also be used instead of the plug, although it requires more careful handling to generate a good seal.

4.3) Apply suction at the outlet of channel C3. With the inlet of C3 sealed, the pressure pulls in media from channel C2, and with it the cells. The strong pressure results in a very rapid alignment of the cells against the wall of C2. To prevent application of excessive pressure that might damage the cells, stop suction after 2 sec and check cell positioning under the microscope. If required, apply more suction in 2-sec pulses.

4.4) Remove the plug, ensuring there is no flow that might dislodge the cells. Leave the device undisturbed in the incubator for 15-20 min.

4.5) After the cells have adhered, return the device to the sterile hood. Empty out the outlets and inlets, and refill the inlets with fresh media to actuate flow before returning the dish to the incubator.

5) Post-processing

5.1) For a device culture, empty out the inlets and outlets and refill the inlets with fresh media twice daily until required for further experimentation.

5.2) To revert to a dish culture, once the cells have adhered, gently remove the device pulling it off beginning at the inlet. This can be done as early as within an hour of cell

adherence, or even a day or two after the culture. The latter allows one to exploit the presence of the fine interconnecting tunnels as guides for controlled neurite outgrowth (Figure A.1B). The device can be autoclaved and re-used for positioning.

Representative Results

Using careful application of gravitational force, centrifugal force and suction to cells in microdevices (Figure A.1A), neuronal networks of varying configurations were created. Figure A.1B represents one of the simplest network architectures that can be obtained with the device, with cells lining up against a wall in response to the applied force, in this case, suction at the outlet of the adjacent channel (C3).

Modifications and combinations of these forces were used to create more complex networks (Figure A.2)

Neuronal networks were tested for signal transmission using glutamate introduced into the central channel at a concentration of 1 mM (Figure A.3). In the absence of controlled cell positioning, the neurons form a loose network within the channel in which they were loaded. As a result, signals initiated in the central channel remained confined to that channel (Figure A.3D and E). On the other hand, with controlled cell positioning used to align cells against the interconnects, the neurons were able to form inter-channel networks. Upon glutamate stimulation, signals were initiated in the central channel and travelled to the outer channels (Figure A.3B and C).

Discussion

The techniques demonstrated here can be modified to result in varying made-to-order cell arrangements. For instance, loading cells into the outer channels and applying suction at the central channel, will result in cells lining up against the inner walls of the outer channels. Cells can then be seeded into the central channel, to create a simple network of three layers that traverses all three channels.

Different techniques can also be combined in a two- or multi-step positioning, to achieve desired configurations. For instance, once suction has been used to align cells against the inner walls of the outer channels and the cells have adhered, one can load additional cells into channels C1 and C2, and use gravitational force to align them against the left walls of the channels. Another step using gravitational force to align cells introduced into C2 and C3 against their right walls, followed by random introduction of cells into C2, would create a 7-layer inter-channel network (Figure A.2). Care should be taken to avoid the use of suction as a second or subsequent technique unless the channel is empty, since the strong force can dislodge pre-adhered cells.

In addition to studies of signaling and development in neuronal networks, this technique can be used to create and study heterotypic networks containing different cell types such as neuron and glia, neurons and myocytes and even non-neuronal networks. The ‘adjacent-stripe’ architecture of these networks (e.g., Figure A.2), also makes them ideal for studies of layered structures in the brain and elsewhere. For instance, neurons from different cortical or hippocampal layers can be laid out side-by-side representing the *in vivo* structures, thereby enabling studies of inherent as well as emergent properties of these networks. Furthermore, this alignment of cells in one line can facilitate assays of

cellular motility and migration in studies of phenomena such as cancer metastasis and wound healing.

Applications of this technique will not only aid in answering new questions, but will also be invaluable in revisiting old questions in the new paradigms emerging at the interface of biology and engineering. [12,13]

Literature cited

1. Carlo, D.D. & Lee, L.P. Dynamic Single-Cell Analysis for Quantitative Biology. *Anal. Chem.* **78**, 7918-925. (2006).

2. Takayama, S. *et al.* Patterning cells and their environments using multiple laminar fluid flows in capillary networks. *P. Natl. Acad. Sci. USA.* **96,** 5545-48 (1999).

3. Li, P. C. H. & Harrison D.J. Transport, manipulation, and reaction of biological cells on-chip using electrokinetic effects. *Anal. Chem.* **69,** 1564-68. (1997).

4. Arai, F. *et al.* On chip single-cell separation and immobilization using optical tweezers and thermosensitive hydrogel. *Lab. Chip.* **5,** 1399-1403. (2005).

5. Li, P. C. H. *et al.* Transport, retention and fluorescent measurement of single biological cells studied in microfluidic chips. *Lab. Chip.* **4,** 174–180. (2004).

6. Wheeler, A. R. *et al*. Microfluidic device for single-cell analysis. *Anal. Chem.* **75,** 3581–3586. (2003).

7. Arai, F. *et al*. High-speed separation system of randomly suspended single living cells by laser trap and dielectrophoresis. *Electrophoresis.* **22,** 283-88. (2001).

8. Enger, J. *et al*. Optical tweezers applied to a microfluidic system. *Lab. Chip.* **4,** 196-200. (2004).

9. Luo, C. *et al*. The combination of optical tweezers and microwell array for cells physical manipulation and localization in microfluidic device. *Biomed. Microdevices.* **9,** 573-78. (2007).

10. Millet, L.J. *et al*. Microfluidic devices for culturing primary mammalian neurons at low densities. *Lab. Chip.* **7,** 987-994. (2007)

11. Millet, L.J. *et al*. Guiding neuron development with planar surface gradients of substrate cues deposited using microfluidic devices. *Lab. Chip.* **10,** 1525-535. (2010)

12. Millet, L.J. & Gillette, M.U. New perspectives on neuronal development via microfluidic environments. *Trends Neurosci.* **35,** 752-761. (2012)

13. Millet, L.J. & Gillette, M.U. Over a century of neuron culture: From the hanging drop to microfluidic devices. *Yale J. Biol. Med.* **85,** 501-521. (2012)

14. Rhee, S.W. *et al*. External force-assisted cell positioning inside microfluidic devices. *Biomed. Microdevices.* **9,** 15-23. (2007).

15. Jain, A. & Gillette, M.U. Development of microfluidic devices for the manipulation of neuronal synapses. *Neuromethods.* **103,** 127-137. (2015)

16. Bodas, D. & Khan-Malek C. Formation of more stable hydrophilic surfaces of PDMS by plasma and chemical treatments. *Microelectronic. Engineering.* **83,** 1277-79. (2006)

17. Banker, G. & Goslin, K. in *Cellular and molecular neuroscience.* **2nd Ed., M,** 666 (1998).

Tables and figures

Name of the reagent	Company	Catalogue number	Comments
PDMS	Dow Corning		
Plasma Cleaner			Any available oxygen-plasma generator can be used.
Inoculation Turntable	Lab Safety Supply	155287	Any available inoculation turntable can be used.
Corning 22x22 mm square No. 1 Cover Glass	Corning	2865-22	Size can be varied according to size of the device
35 mm Petri Dish	BD Falcon	351008	Size can be varied according to size of the device
Neurobasal-A medium minus phenol red	Invitrogen	12349-015	
Hibernate-A medium minus phenol red	BrainBits		
B27	Invitrogen	17504-044	
Glutamax	Invitrogen	35050-061	
Poly-D-Lysine Hydrobromide	Sigma	P-6407	
Papain, Lyophilized	Worthington	LS003118	

Table A.1. Table of specific reagents and equipment. A table of the reagents and equipment required to create neuronal networks of the desired configuration, with columns 2 and 3 listing company and catalogue information for their acquisition.

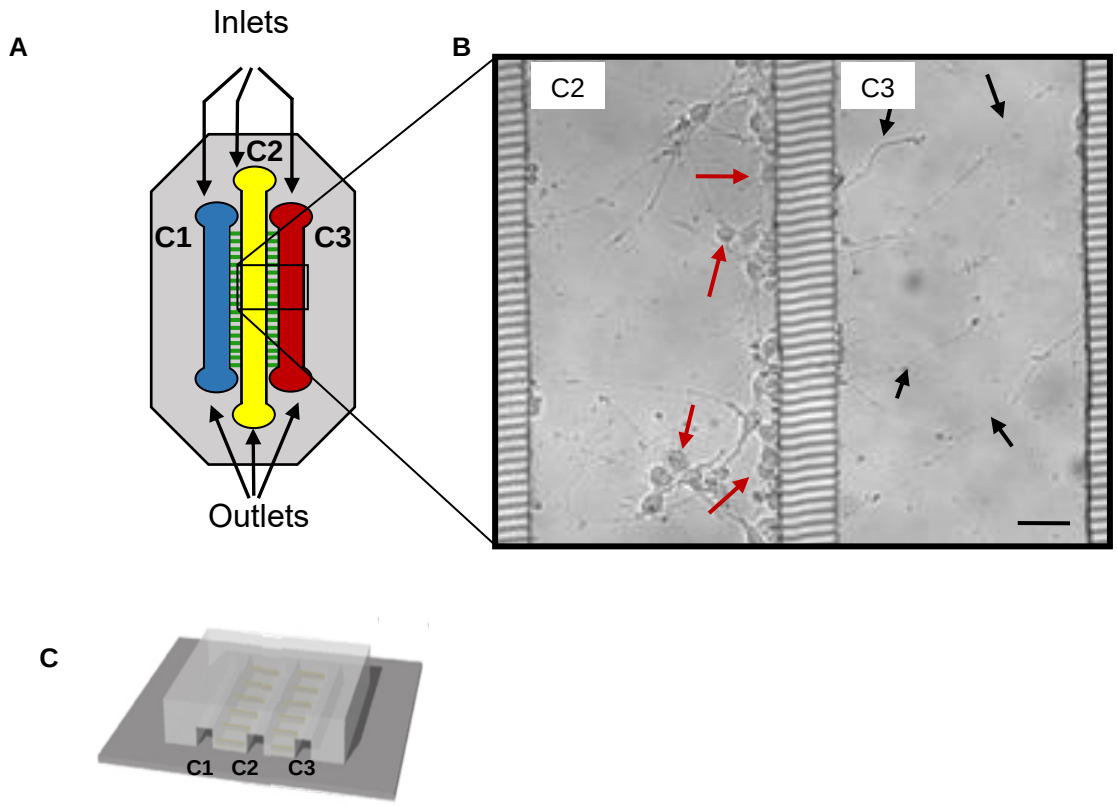

Figure A.1. Microfluidic devices enable positioning of cells. (A) Schematic, (B) Microscopic, and (C) 3D-representation of the device design. C1, C2, C3 are three channels, each 200 μm wide and 45 μm high. The channels communicate through narrow interconnects, 7 μm x 7 μm and 45 μm long. (B) A 5-day-old neuronal culture with neurons positioned against the right wall of channel C2. Neurons were loaded into C2 and suction was applied at the outlet of C3. Neurons in C2 (red arrows) lined up against the wall and sent out processes (black arrows) through the interconnecting tunnels, into C3. Scale bar = 50 μm.

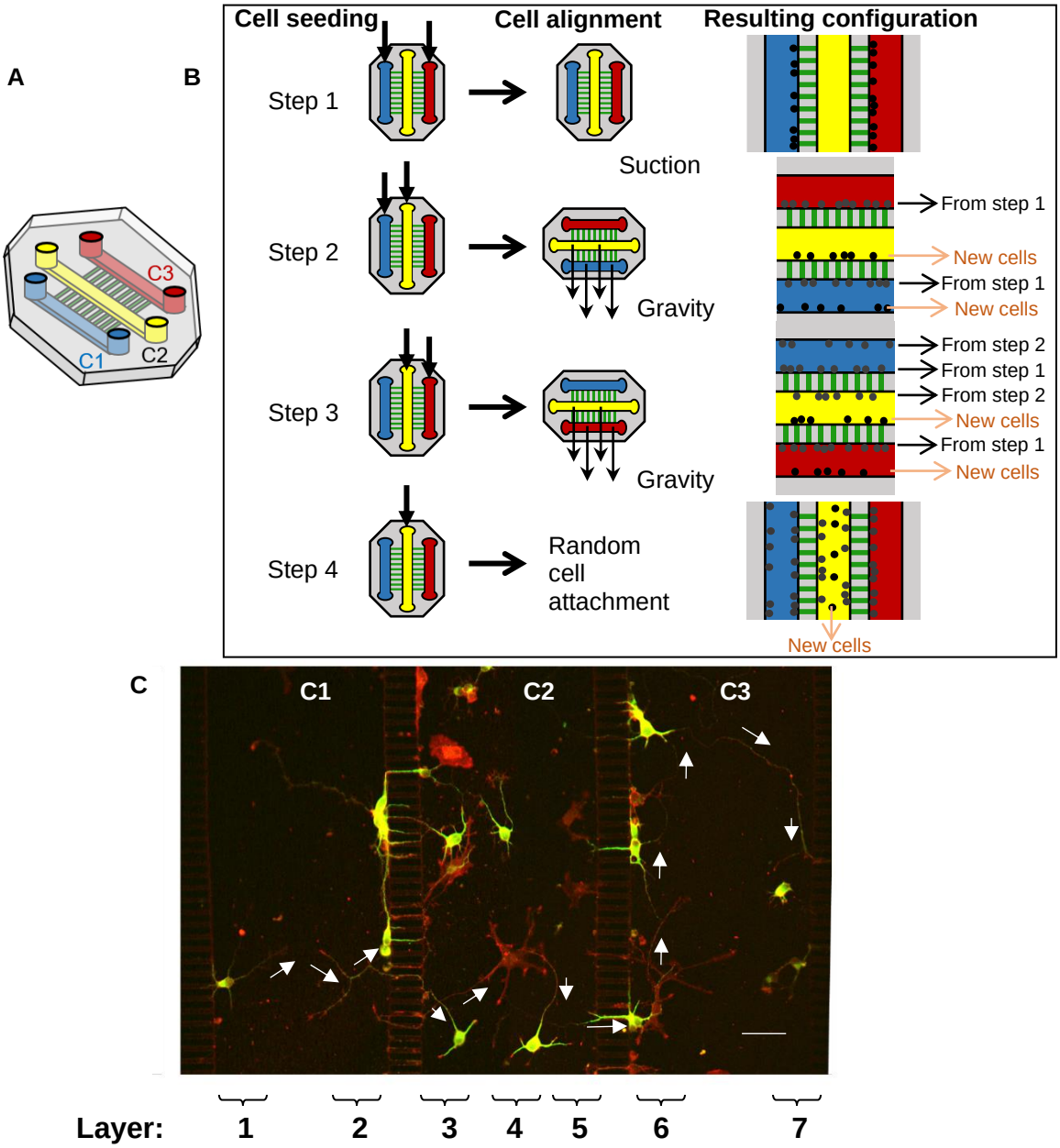

Figure A.2. Modifications and combinations of the forces result in intricate network designs. (A) A 3D-representation of device design. C1, C2, C3 are three channels (200 μm wide, 45 μm high) communicating through narrow interconnects (7 μm x 7 μm and 45 μm long, in green). (B) Process flow for cell seeding and alignment in four sequential steps. (C) A 7-layer network of primary rat hippocampal neurons at 2 DIV generated using the process flow in (B) – Step 1: Suction, used to generate layers 2 and 6; Step 2: Gravitational force, to position layers 1 and 3; Step 3: Gravitational force, again, to position layers 5 and 7; Step 4: Cells seeded without any alignment forces, resulting in randomly positioned cells, for layer 4. Cytoskeletal markers (green: MAP2, red: rhodamine-phalloidin) label neurites growing out, and establishing intra-layer and inter-layer contacts. White arrows highlight a network of cell-cell contacts beginning in layer 1 and connecting cells all the way through layer 7. Scale bar = 50 μm.

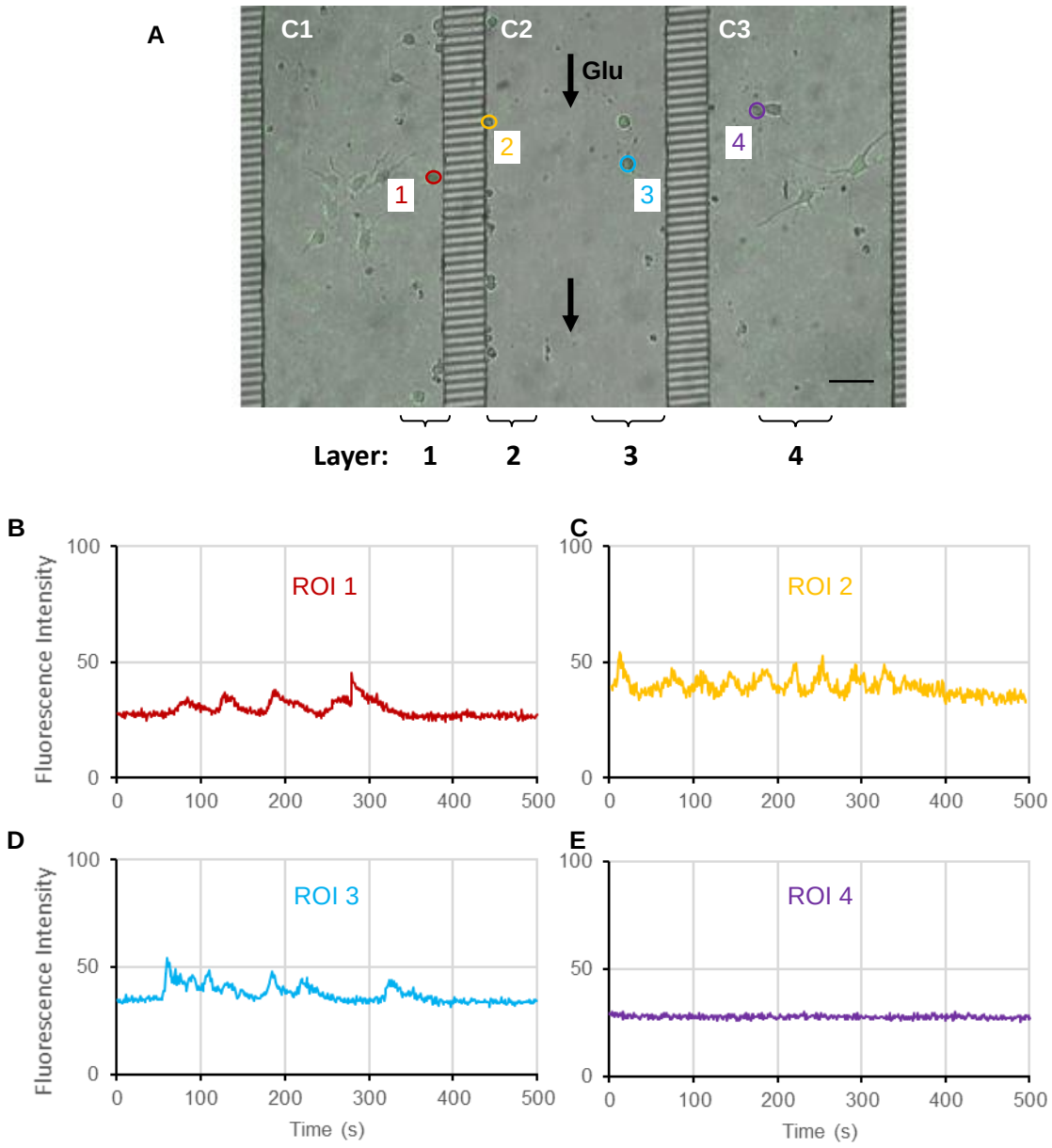

Figure A.3. Demonstration of signal transmission through a designed network extending across microfluidic channels. (A) Primary hippocampal neurons in a microfluidic device at 4 DIV. Cell layers 1 and 2 aligned using suction and gravity, respectively, form more compact layers than randomly aligned layers 3 and 4. The proximity and the guidance provided by interconnects promote formation of cell-cell contacts and, thereby, of an inter-channel inter-layer network between the former pair. Glutamate (1 mM) introduced into the central channel C2 initiates Ca^{2+} signaling in cells in C2. (C) and (D) show representative traces of Ca^{2+} waves in cells 2 and 3, visualized as peaks in fluorescence of Ca^{2+} indicator Fluo-4. Fluidic isolation prevents glutamate entry into C1 and C3, but signals are transmitted from cells of layer 2 to those of layer 1 through the neuronal network. This inter-channel cell signaling initiates Ca^{2+} transients in cell 1 (B). Randomly aligned layers 3 and 4 show no such communication (E). Scale bar = 50 μm, ROI: Region of interest.